Using rock physics to determine uncertainties in pore-fluid and lithology-estimates from seismic attributes in the Bredasdorp Basin, offshore South Africa

January, 2006

Tobias R. Tönsing

Presented in fulfillment of the requirements for an MSc degree at the Department of Geological Sciences, University of Cape Town

ABSTRACT

This study is aimed at developing a workflow for quantitative seismic interpretation. The workflow generates probability maps of various facies and pore-fluids by combining seismic attributes and wireline log data through rock physics relationships and supervised statistical classification. The workflow was developed mainly for hydrocarbon exploration, but could be used for other purposes, provided the target is seismically detectible.

Any prior regional geological knowledge is built into the workflow, by extending the training data appropriately. The workflow aims to maximize the extraction of quantitative geological parameters from data that are most commonly acquired for hydrocarbon exploration, namely seismic and wireline log data.

The workflow is presented as a case study using 3D seismic data from the Bredasdorp Basin offshore South Africa's south-coast. Wireline log data from the E-BX1 borehole are also used in the study, as well as regional geological interpretations. The study is focused on the siliciclastic Aptian "13B" sequence, which was encountered at a depth of 2500 m below sea level at borehole E-BX1. Two massive 13B sandstone units were encountered at E-BX1. The lower unit is 50 m, and the upper 20 m thick. Both are water wet.

The results of this study suggest that there are two oil accumulations at the 13B level around E-BX1. This is indicated by the high probability predicted for oil-bearing sandstone in these two areas.

Acknowledgements

I would like to extend my sincere appreciation to the following persons and institutions:

- The Petroleum Oil and Gas Corporation of South Africa for funding this work, and also for their kind permission to use the data from the Bredasdorp Basin.
- My supervisor from the University of Cape Town, George Smith, for his guidance and support.
- Dr. Patrick Young for his guidance and fruitful discussions.
- Kobus van Wyk and Andrew Dippenaar for their encouragement.

and finally, to my wife, Susanne, for her moral support.

Index

List of Figures

Tables

Equations

Abbreviations

AVO	Amplitude variation with offset
CC	Correlation coefficient
DEM	Differential effective medium
E & P	Exploration and production
GR	Gamma ray
I_e	Elastic Impedance
I_p	P-wave acoustic impedance
I_s	S-wave acoustic impedance
LMR	$\lambda\mu\rho$
STP	Standard temperature and pressure
VCL	Volume of clay
Vp	P-wave velocity
Vs	S-wave velocity
PDF	Probability Density Function

Appendixes

1. Introduction

Exploration for producible hydrocarbon accumulations has been ongoing since the mid 1970's offshore South Africa. Hydrocarbon accumulations occur in the Cretaceous sediments of the Bredasdorp Basin. Due to a paucity of structural closures in these sediments, hydrocarbons are mainly encountered in stratigraphically isolated sandstone. Detached deep marine turbidite accumulations form the primary exploration targets. Since these are usually difficult to image on conventional seismic data, seismic attributes have played a large role in the Bredasdorp Basin hydrocarbon exploration history. The drive to generate direct hydrocarbon indicators from seismic data culminated in the introduction of the Fluid Factor (Geostack technique) by George Smith and Maurice Gidlow in 1986 (Smith and Gidlow, 1987).

Offshore exploration occurs mainly by acquisition and interpretation of marine seismic, wireline log and other borehole data. Wireline log data provides high-resolution information of the rocks and their pore-fill along a borehole trajectory. Seismic data, on the other hand, are usually acquired over large areas and provides lower resolution information about the subsurface environment. In order to derive meaningful attributes from seismic data, information from wireline logs must be correlated to the seismic data. This involves converting the depth axis of the log data to that of two-way seismic traveltime, computation of the desired attributes, and representing these attributes at seismic frequencies. At this stage a direct comparison of seismic and log attributes can be made at the borehole location. Unfortunately the interpretation of seismic attributes is non-unique. Rocks with different fundamental elements (mineralogy, matrices, porosities and fluids) can yield similar values of a specific attribute. Therefore using a specific seismic attribute to predict either rock composition and/or fluid content will always have some uncertainty associated with it.

In order to assess the uncertainty that is associated with using a seismic attribute to a specific end (using the Fluid Factor as an indicator of hydrocarbon saturation for example), the variation in rock and fluid parameters need to be determined. The relationship between these parameters and the seismic attribute of interest also needs to be defined. With this information, it is possible to statistically calculate the uncertainty that is inherent in using a seismic attribute as an indicator of rock properties (lithology or pore-fluid fill for example).

2. Objective and overview

The objective of this study is to develop a workflow for quantitative interpretation of seismic data. This is achieved in two steps. Firstly, with rock physics relationships, which relate the information from wireline logging data with seismic attributes, and secondly with statistical classification, which allows quantification of these relationships, and ultimately quantification of the seismic interpretation. The workflow is developed using 3D seismic and wireline logging data from the Bredasdorp Basin, offshore South Africa.

The development of this workflow is reported in four chapters, and a brief overview is provided for each chapter below.

As a first step, the principles of rock physics and statistical classification theory are discussed in chapter 3. Many of the principles of both rock physics and statistical classification have been known for many years. Recently both fields have received renewed interest from amongst others, the oil and gas-exploration industry, and this is probably as a result of the increasing availability of cheap and fast computing power, as well as the increasing geological complexity of the remaining hydrocarbon resources. Chapter 3 concludes with the presentation of a workflow for quantitative seismic interpretation using rock physics. This workflow will be discussed and implemented in the chapters to follow. In chapter 4, the dataset from the Bredasdorp Basin offshore South Africa is introduced. A geological model is formulated using this, and other regional data. The seismic and wireline log data, together with the geological model are used to calibrate the training data for the statistical classification. This is discussed in chapter 5, which documents most of the technical work on seismic attributes and classification. The last part of the study is chapter 6, where the results of the seismic data classification are presented and discussed.

3. Rock Physics and Statistical Classification Theory

3.1 Rock Physics

"Rock Physics describes a reservoir rock by physical properties such as porosity, rigidity, compressibility; properties that will affect how seismic waves physically travel through the rocks" (Dewar, 2001). Over the last decades, rock physics has become increasingly important in oil exploration and research. Oil discoveries are becoming relatively smaller in size, and are located in geologically and operationally complex areas. This has generated a need to better determine geological parameters through more accurate and diverse geophysical measurements, and more sophisticated rock physics relationships.

In this section, rock physics relationships pertaining to wave propagation in saturated, porous media, are explored. Firstly, the concept of effective media is discussed. Then the Gassmann (1951) equations, which quantify fluid effects on wave propagation, are explored. The section concludes with the Xu-White velocity model, which employs both effective medium theory and fluid effects to describe wave propagation in saturated sand-clay mixtures (Xu and White, 1995).

These rock physics relationships will form the basis for quantifying geological parameters from seismic and log data in later chapters.

3.1.1 Effective medium theory

During exploration for hydrocarbons, three types of data are mainly recorded for geophysical analyses, they are:

- Seismic data
- Log data

- Geological data (core data)

Since the seismic reflection character of the subsurface layers depends mainly on their velocities and densities, sonic and density logs are used to correlate seismic data at boreholes. However, if one wishes to relate the seismic data to morphological parameters of rocks (such as composition, porosity, pore-fill and fabric), a further step is necessary. This step involves effective medium theory, which relates the morphology of a rock to its elastic parameters.

Most data recorded for exploration purposes are band-limited. This implies that measurements (from seismic data for example) are in essence averaged over some finite volume of subsurface material. The aim of effective medium theories is to predict the overall elastic properties of a volume of material that is equivalent in size to the band-limitation of the measurements. In other words, if we consider a heterogeneous rock comprising grains, pores and cracks, which are much smaller than seismic wavelength, then effective medium theory allows us to calculate an effective homogeneous material which is much simplified, yet indistinguishable from the original, provided that low frequency measurements are considered.

The elastic properties of an effective medium depend mainly on the elastic properties of the constituent materials and their geometries. A number of formulae that relate these exist. In this chapter, a brief outline of different effective media formulations will be discussed, and special attention will be given to the Xu-White and Gassmann equations.

3.1.2 Effective media bounds

The effective elastic moduli of a mixture of grains and pores can be approximated with rock physics relationships if the following data are known;

1. Elastic properties of grain- and pore-material
2. Ratio of grains to pores
3. Geometry of the pores
4. Cementation

Data relating to points one and two above can usually be obtained, since the elastic properties of rocks and minerals are well documented, and porosity log data can be used to determine the ratio of grains to pores. The geometry of pores in sedimentary rocks is however not so easily determined. This is because laboratory analyses of core data are needed to describe it. In the absence of knowing the pore geometry of a sedimentary rock, the effective elastic parameters of the rock cannot be determined, and only upper and lower bounds for these parameters can be established. An easy way to understand these bounds is by visualizing "stiff" and "soft" pore shapes. For example, a water-saturated sandstone where each sandstone grain is surrounded by water (soft pore shapes) will have a much lower bulk modulus than one where the sand grains are cemented together (stiff pore shapes). The simplest bounds (but not necessarily the best) were defined by the Voigt (1910) and Reuss (1929) bounds. Hashin and Shtrikman defined the upper and lower bounds as the narrowest possible range of effective elastic parameters that can be defined without specifying anything about the geometries of the constituents (Hashin and Shtrikman, 1963). Figure 1 shows a graph of the upper and lower bounds of the effective bulk modulus when mixing two materials with bulk modulus K1 and K2 (taken from Mavko et al., 1998).

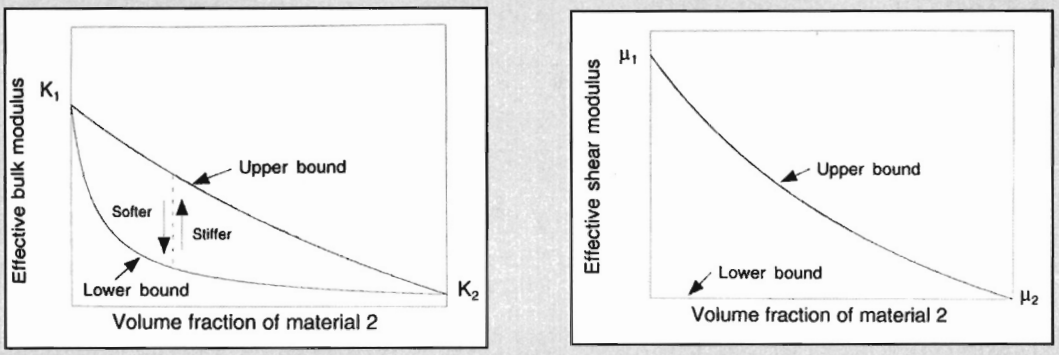

Figure 1. Graphs of the upper and lower bounds on the bulk modulus (K) and shear modulus (μ) of a mixture of two materials. (taken from Mavko et al., 1998).

The Hashin and Shtrikman formulae assume that both the constituents and the effective medium are isotropic, linear and perfectly elastic. The formulae for the Voigt and Reuss, and the Hashin and Shtrikman formulae are given below. The upper and lower Hashin and Shtrikman bounds are calculated by interchanging which material is termed 1 and 2 (Hashin and Shtrikman, 1963).

Voigt upper bound:

$$M_{voigt} = \sum_{i=1}^{n} V_i M_i$$

Reuss lower Bound:

$$\frac{1}{M_{reuss}} = \sum_{i=1}^{n} \frac{V_i}{M_i}$$

Hashin and Shtrikman bounds:

$$K_{hashin-shtrikman} = K_1 + \frac{V_2}{(K_2 - K_1)^{-1} + V_1(K_1 + 4/3\,\mu_1)^{-1}}$$

$$\mu_{hashin-shtrikman} = \mu_1 + \frac{V_2}{(\mu_2 - \mu_1)^{-1} + \frac{2V_1(K_1 + 2\mu_1)}{5\mu_1(K_1 + 4/3\,\mu_1)}} \qquad (1)$$

K - bulk modulus. μ - shear modulus.

M - bulk or shear modulus. V - volume fractions of material 1 and 2.

3.1.3 Kuster and Toksöz effective medium theory

In 1974, Kuster and Toksöz presented an effective medium theory for a two-phase medium (Kuster and Toksöz, 1974). Both phases are treated as homogeneous, with the first phase being a continuum in which inclusions of the second phase are randomly embedded. Their formulation allows for a number of inclusion shapes, ranging from spheres, to oblate and prolate ellipsoids. The Kuster and Toksöz effective medium theory is based on a first order scatter theory, which implies that the formulations are for wavelengths much longer than the inclusions. The formulation also assumes that multiple scattering effects are negligible. This assumption implies that pore concentration must be dilute, so that interactions between adjacent pores can be ignored.

An advantage of the Kuster and Toksöz effective medium theory is that it allows for inclusions with different material properties and/ or different shapes. Each material and shape requires a separate term in the formula. The elastic properties of a wide range of porous rock morphologies may thus be simulated with these equations. A generalized version of these equations is given below.

$$(K_{KT} - K_m)\frac{(K_m + 4/3\,\mu_m)}{(K_{KT} + 4/3\,\mu_m)} = \sum_{i=1}^{N} V_i (K_i - K_m) P^{mi}$$

$$(\mu_{KT} - \mu_m)\frac{(\mu_m + \xi_m)}{(\mu_{KT} + \xi_m)} = \sum_{i=1}^{N} V_i (\mu_i - \mu_m) Q^{mi} \qquad (2)$$

K bulk modulus (K_{KT}– Kuster Toksöz bulk modulus)

μ shear modulus (μ_{KT}– Kuster Toksöz shear modulus)

$\sum_{i=1}^{N}$ summation over different inclusion types with volume V_i

$$\xi = \frac{\mu(9K + 8\mu)}{9(K + 2\mu)}$$

P^{mi} and Q^{mi} describe the effect of an inclusion of material i in a background medium m (Mavko et al., 1998).

One disadvantage of the Kuster and Toksöz approach is the fact that at low frequencies, most porous sedimentary rocks allow seismically induced pore pressures to equilibrate between pores (Mavko et al., 1998). This violates the restricted pore interaction assumption, and causes discrepancies between effective and real elastic properties.

3.1.4 Differential effective medium

The formulations for a differential effective medium (DEM) were developed by Norris and Zimmerman, and are also based on a first-order scatter theory like the Kuster and Toksöz formulae (Norris, 1985; Zimmerman, 1991). These DEM theories tried to partially overcome the restricted pore interaction limitation by iteratively adding a dilute pore concentration to an "effective" matrix. In other words, the Kuster and Toksöz formulation for an effective medium is repeatedly calculated with a dilute pore concentration, until the desired porosity is obtained. It is important to note that pore interactions are never really calculated, but rather simulated through repeatedly calculating a dilute pore volume. The derivation of the DEM equations as given in Norris assumes that as a new pore is introduced, it on average replaces either the host material, or the previously introduced pore material with a user-defined probability. Norris has also shown that his DEM formulation conforms to the Hashin - Shtrikman upper and lower bounds (Norris, 1985). In Zimmerman's DEM formulation, the new pore material always replaces the host material (Zimmerman, 1991).

3.1.5 Differential elastic medium with critical porosity constraint

The differential elastic medium equations assume that the solid host material stays intact at all porosities. Sedimentary rocks do not behave like this, because the frame of connected sediments falls apart at the critical porosity. At this porosity, the matrix grains become supported by pore material, which violates the connected-matrix assumption of the differential elastic medium formulae. Mukerji et al. modified the differential elastic medium formulae to include this effect, by using the suspension model at or above a specified critical porosity (Mukerji et al., 1995). Figure 2 is taken from this paper (Mukerji et al., 1995), and shows how the critical porosity modification affects the effective bulk modulus for different values of critical porosity.

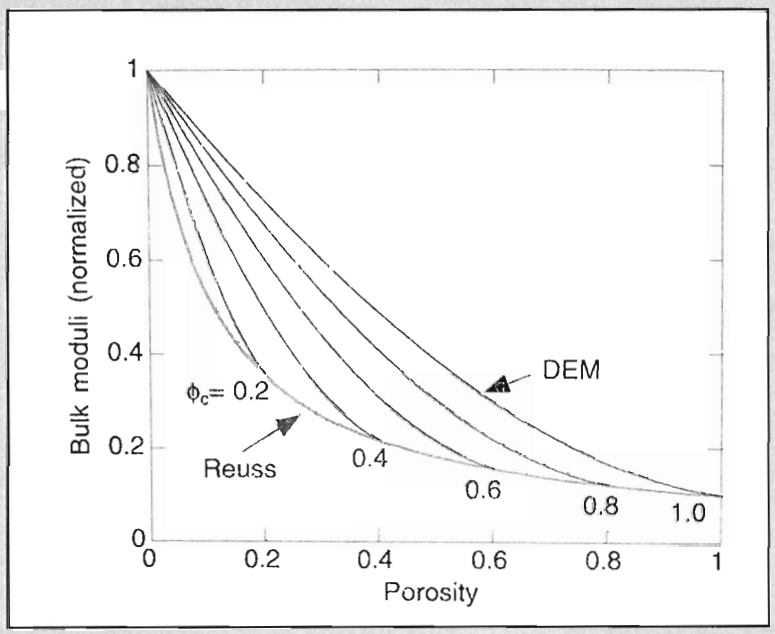

Figure 2. Differential effective medium bulk modulus with critical porosity constraint (taken from Mukerji et al., 1995).

Although DEM formulations try to simulate pore interaction, it should always be borne in mind that at each iteration, the pore volume is assumed dilute

(Mavko et al., 1998). These equations are thus still termed high frequency approximations, since fluid relaxation through pore interaction is ignored. This is discussed further in section 3.1.7.

3.1.6 The Gassmann relationships

In 1951, F. Gassmann presented a paper entitled "Elastic behavior of porous media" (Gassmann, 1951). In this paper, Gassmann uses elasticity theory to derive formulae that relate the elastic parameters of a saturated porous medium to the elastic properties of the porous frame and the saturating medium (liquid or gas). Gassmann's equations were formulated to predict elastic wave propagation in "differentially elastic" media. Differentially elastic media are those that deform irreversibly (plastic) when subject to large stress, but behave linearly elastic when subjected to small stress fields, such as those caused by acoustic waves.

In his paper, Gassmann envisages the main field of application of his formulae to be associated with building material design, acoustics and seismology. Over fifty years later, the Gassmann equations are most widely used for fluid replacement in seismic modeling. It is important to remember that the equations make the following assumptions;

1. The porous material (or frame) is differentially elastic, as described above.
2. The frame and the pore-filling material is homogeneous.
3. The pores of the frame are connected, and thus in pressure equilibrium.
4. The wavelength of the seismic wave is much larger than the pore dimensions.

It should be noted that Gassamnn's original equations were formulated for both isotropic and anisotropic frames, and also open and closed pore-

systems. Most modern software packages that use the Gassmann's equations for fluid substitution use the isotropic, closed frame formulation of the equations given by Mavko et al. (1998).

$$\frac{K_{sat}}{K_0 - K_{sat}} = \frac{K_{dry}}{K_0 - K_{dry}} + \frac{K_{fl}}{\phi(K_0 - K_{fl})} \qquad \text{and} \qquad \mu_{sat} = \mu_{dry} \qquad (3)$$

K bulk modulus ($_{dry}$=dry rock, $_{fl}$=pore fluid, $_{sat}$=rock with pore fluid, $_0$=mineral making up the rock)

ϕ porosity

μ shear modulus ($_{dry}$=dry rock, $_{sat}$=rock with pore fluid)

The assumptions that limit the use of the Gassmann equations for reservoir fluid modeling are points 3 and 4 above. In heavily cemented reservoirs, or in reservoirs with secondary porosity, where pores are isolated, Gassmann's equations are invalid. Also, where measurements of elastic parameters are made from high frequency data, errors may be introduced. The exact frequency at which Gassmann's relationships deviate depends on the pore-size. For common sandstone pore dimensions, the Gassmann equations can be used for conventional seismic data (0-100Hz). Depending on lithology, the equations still give good results at sonic logging frequencies (1-10 kHz), but fail at ultrasonic laboratory frequencies (0.1 – 1 MHz). The reason for this is that at high frequencies, wave propagation occurs at a similar speed to pore pressure equilibration. This implies that a state of pressure equilibrium is not reached during wave propagation, which increases the overall stiffness of the medium. For high frequency investigations, the Biot or SQUIRT formulae need to be applied. Pore shape and size are needed as input parameters for these equations. Since the fluid effects are modeled at relatively low frequencies in this study, the high frequency elastic formulae are not used.

Another assumption in the Gassmann equations is that of a homogeneous pore-filling fluid. This assumption may be violated when the pore fill is mobilized during drilling and production. In such instances, the porous medium may have a patchy saturation, implying that pore-fill is no longer homogeneous. A simple way to deal with this situation is to assume that the pore-fill is evenly patchy, and thus macroscopically homogeneous. Effective elastic fluid properties may then be calculated for the pore-fill, and used in Gassmann's equations.

Application of Gassmann's equations to fluid substitution

It has been mentioned before that although not originally intended by Gassmann, his relationships today are mainly used for fluid substitution in seismic modeling. The application of the Gassmann equations depends on the data available to the user. In their original state, the equations relate the elastic parameters of a saturated porous medium to those of the drained, porous frame. The aim of fluid substitution is to calculate the elastic parameters of a porous rock when the original pore fluid is replaced with another (for example brine with oil). A reformulation of the equations is thus necessary. Furthermore, the drained pore frame parameters are usually not available, since specialized laboratory analysis of core data are usually not available. For fluid substitution, Gassmann's equations are thus used in two steps. In the first step, recorded Vp and Vs data, together with measured fluid properties are used in an inverted Gassmann formula, which calculates the "drained" or "dry" rock elastic properties. These are then used together with the new fluid parameters to give substituted values of Vp and Vs. In some cases further assumptions need to be made, due to data limitations. For example, the Vs sonic log is not always available. In this case, an assumption about the "dry" rock Poisson's ratio can be made. The dry-rock Poisson's ratio is related to the Vp and Vs of the dry rock.

The elastic properties of a liquid or gas depend on its composition, temperature and pressure. Batzle and Wang give a full overview of how these are related (Batzle and Wang, 1992).

3.1.7 The Xu and White velocity model for clay-sandstone mixtures

In 1995, Xu and White presented a new velocity-porosity model for sedimentary rocks comprising shale and sandstone (Xu and White, 1995). Initially, their research revolved around predicting sonic logs from other logs over large depth intervals. In a particular dataset, where both sonic and porosity logs are available, they noticed a large error in the predicted velocities using conventional velocity-porosity relationships such as Wood's and Wyllie's equations (Wood, 1955 and Wyllie et al., 1963). In trying to understand why these failed to accurately predict the velocities, one needs to understand how they were derived.

Wood's formula allows calculation of sound velocity in a suspension or fluid mixture (Wood, 1955). The effective moduli for such a medium coincide with the lower Hashin-Shtrikman bound. Shale comprises sheet-like minerals such as kaolinite. The negative surface charge of clay particles attracts dissolved cations from surrounding pore fluids (Snyman, 1996). At shallow burial depths, and in overpressured shale formations, individual particles may thus be entirely surrounded by fluid. This occurs despite the low porosity, with the implication that pore aspect ratios are very low. The effective moduli of shallow or overpressured shale are thus well approximated by Wood's suspension model. The most important observation about shale conforming to Wood's suspension model is that at low porosity values, velocity is highly sensitive to small changes in porosity.

Wyllie et al. developed an empirical relationship between velocity and porosity from laboratory measurements of cemented sandstone (Wyllie et al.,

1963). He developed the relationship after noticing a velocity-porosity trend in certain sandstone with the following properties:

1. The matrix has a uniform mineralogy
2. The pore-space is fluid saturated
3. The rocks are under high effective pressure

If these criteria are met, then the total transit time is the sum of the transit time in the matrix mineral plus the transit time in the pore fluid. Wyllie's equation is thus referred to as the *time-average equation*, and is given below;

$$\frac{1}{Vp} = \frac{\phi}{Vp_{fl}} + \frac{1-\phi}{Vp_{dry}} \qquad (4)$$

Vp P-wave velocity of saturated rock

Vp_{fl} P-wave velocity of pore fluid

Vp_{dry} P-wave velocity of mineral rock frame

ϕ Porosity

In their research, Xu and White noticed that over large depth intervals, neither Wood's nor Wyllie's relationships adequately describe the variation of velocity. They also noted that much of the scatter in the velocity-porosity domain could be attributed to variations in lithology, specifically sand and clay. This led them to generate a new velocity model, which focuses on clay-sand sedimentary mixtures. The main point of this new model was summarised by Xu and White as follows, '*the essential of the model is the assumption that the geometry associated with sand grains is significantly different from that associated with clays. Because of this, porosity in shale affects elastic compliance differently from porosity in sandstone*' (Xu and White, 1995).

In order to calculate the effect of the different clay and sand pore geometries, Xu and White use the Kuster and Toksöz effective medium theory to calculate

dry frame moduli (section 3.1.3). The Gassmann theory is then used to obtain the elastic moduli of the saturated medium. The Kuster and Toksöz theory is only used for the dry frame parameters because it assumes pores are separated. For saturated media this would mean that low frequency fluid equilibration effects are not accounted for. This limitation becomes irrelevant when pores are empty (dry). Once the elastic parameters of the dry frame have been established, Gassmann's low frequency equation can be used to include the fluid elasticity.

The key part of the Xu-White model is the hypothesis that the aspect ratios of sand related pores are significantly different from the aspect ratios of shale related pores. Since data pertaining to aspect ratios of subsurface rocks are usually limited, Xu and White suggest that the total pore space (ϕ) is divided into shale pores (ϕ_{sh}) and sand pores (ϕ_{ss}) according to the ratio of shale to sand in the rock. This ratio can be obtained from gamma ray logs.

The next step involves calculating the velocity and density of the matrix material. The velocity is calculated with the time-average equation, whereas the density is an average of the sand- and shale density, weighted by volume. Once this has been obtained, the effect of introducing shale and sand pores is determined with the Kuster and Toksöz theory. The Xu-White model assumes oblate pore shapes with different, user-defined aspect ratios for the sand and shale pores. Finally, the effect of fluid elasticity is simulated using the Gassmann equations.

The Xu-White model requires knowledge of the aspect ratios of both sand and shale pores. These parameters can be measured from thin section analysis, although this is rarely available from offshore core data. In order to get an indication of the magnitude of pore aspect ratios, Xu-White suggest that their equations are inverted over intervals where density, porosity, shale volume, Vp and Vs data are available. In other words, over intervals where all data except aspect ratios are available (from logging or core data), the Xu-

White formulae can be rewritten to determine shale and sand pore aspect ratios. This step can also be called a calibration. The advantage of this approach is that a very complex model, which includes effective medium theory and fluid substitution, can now be applied using relatively standard offshore logging data.

Figure 3 shows measured vs. predicted velocity plots from work done by Xu and White. In the left-hand plot, the velocity was predicted using the Wyllie equation, whereas in the right-hand plot, the velocity was predicted using a calibrated Xu-White relationship. The improvement of using the Xu-White model to predict Vp is clearly illustrated by the reduction in scatter.

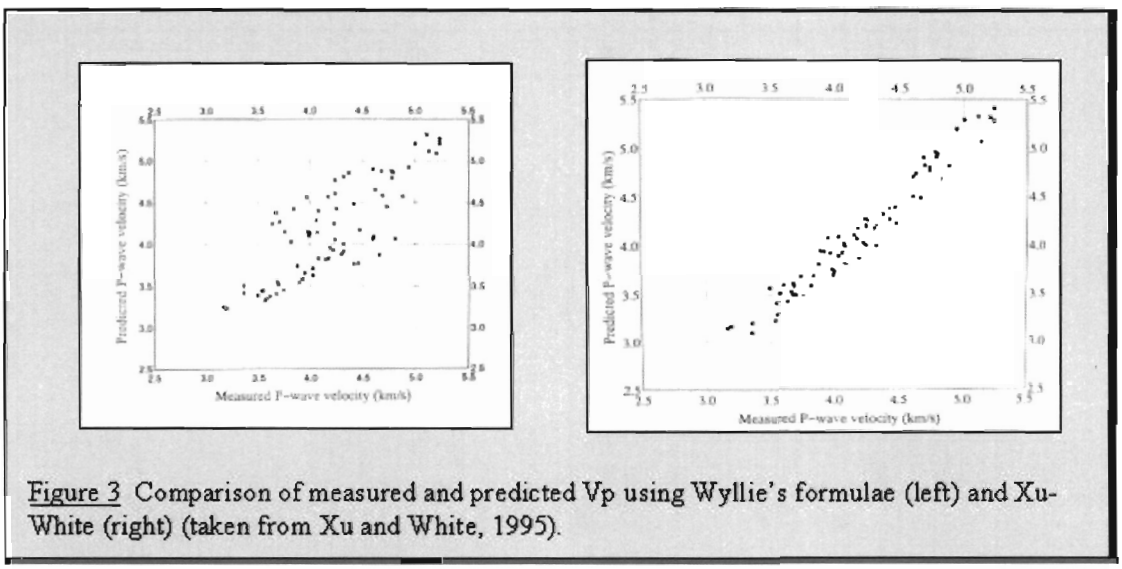

Figure 3 Comparison of measured and predicted Vp using Wyllie's formulae (left) and Xu-White (right) (taken from Xu and White, 1995).

Besides accounting for variations in lithology, Xu and White claim that other parameters affecting velocity can also be explained through pore shape variations (Xu and White, 1995). For example, effective pressure controls the closure of cracks. Overpressure in a buried formation can preserve low aspect ratio pores, and thus affect velocity. If this is the main control on aspect ratios, then the Xu-White relationship could be calibrated to map overpressure. Depending on the geology, cementation may be the main controlling factor on pore aspect ratios. In this case, the Xu-White model may be calibrated to measure cementation variations.

3.2 Statistical Classification Theory

Statistics, and specifically geostatistics can be meaningfully applied throughout the entire E&P cycle, from seismic exploration, log analysis, static and dynamic earth models to commercial analyses and high level investment decisions (Dubrule, 2003). In a nutshell, statistics and geostatistics allow us to quantify and combine all the uncertainties identified by various disciplines, in order to translate them into informed management decisions.

In this study, only a small part of statistics will be used. This relates to classifying seismic attributes. Statistical classification can be either quantitative, categorical, or a combination of the two. Quantitative classification means that the data, for example seismic attributes, are used to predict a quantity, such as the probability of oil. Categorical classification means that the seismic attributes are used to predict presence of different lithologies and pore fluids. In this study, a combination of categorical and quantitative classification will be done, in the sense that $\lambda\mu\rho$ (LMR) attributes will be used to classify the data into different categories (oil-bearing sandstone, shale, etc.), and will also be used to predict the probability of each category. This type of classification has also been called supervised classification (Hastie et al., 2001) since a training dataset is required for calibration. Another type of classification is unsupervised classification, which tries to establish statistically significant categories in the data, without knowing exactly whether these are geologically significant. Avseth et al. suggest that supervised classification gives more meaningful results than unsupervised classification, mainly because unsupervised classification may generate categories that bear no geological significance (Avseth et al., 2005).

Many algorithms can be used for both quantitative and categorical, and supervised and unsupervised statistical classifications (Hastie et al., 2001). They include discriminant analysis, principal component analysis, Bayesian

classification and neural network classification. For this study discriminant analysis will be used. Avseth et al. present a comparison of classification results from various algorithms, and conclude that classification results are largely similar, provided the prior level of training is similar (Avseth et al., 2005).

3.2.1 Discriminant analysis

Discriminant analysis requires training data to classify the data (supervised classification). In this case, the discriminant analysis will use the LMR attributes calculated from logging data to classify the seismic data into litho-categories. Discriminant analysis uses the statistical properties of the training data, such as the mean, variance, and covariance, to classify the seismic data into predefined classes. These classes, and their probability of occurrence, are the output of discriminant analysis. At well locations, both the input (attributes) and the output (litho-categories) are known. They will thus be used as the training data. For example, a cross-plot of $\lambda\rho$ and $\mu\rho$, can be plotted for various lithologies and fluid fill categories at a well. Discriminant analysis will use the scatter of values per class to determine 2D variograms in the $\lambda\rho$-$\mu\rho$ domain, and use these to determine the probability of new data belonging to a certain category. New data are classified according to the distance to the center of each cluster, which is also an indication of the probability of that data belonging to the cluster. The distance to the centre of a cluster is not necessarily the linear, or Euclidean distance. The Mahalanobis distance is a better measure for classification, since it takes into account the shape of the clusters irrespective of the scale of measurements (Reinhard et al., 1991). The Mahalanobis distance formula is given below.

$$M = \sqrt{2\left(1 - \frac{a \bullet b}{\sqrt{a \bullet a}\sqrt{b \bullet b}}\right)} \qquad (5)$$

M –Mahalanobis distance

a – coordinates of data point to be classified

b – coordinates of centre of cluster

• - dot product

Discriminant analysis can be done with any number of attributes, and any combination of the attributes. The success of the classification depends on the amount of separation between classes, and the algorithm used to classify the data. The classification success is measured through a process called validation. The output of validation is a matrix P, whose elements P_{ij} are conditional probabilities. These probabilities are calculated with the Mahalanobis distance formula (Formula 2). P_{ij} is the probability that category i is predicted as category j. The matrix P is also called the classification success ratio matrix (Avseth et al., 2005). The diagonal elements of P (i.e. P_{ii}) are the conditional probabilities of the categories being classified correctly. The rows of P add up to 1. P is not symmetric, because the probability that category i is predicted as category j, is not the same as that of j being predicted as i. High values along the diagonal imply a good classification success.

3.3 Combining Rock Physics and Statistical Classification

In sections 3.1 and 3.2, the theory of certain rock physics and statistical classification principles were discussed. In this section a workflow will be presented which integrates these theories for seismic lithology and fluid prediction. The workflow is shown in Figure 4, and can essentially be divided into three main parts. Each of these is discussed in more detail below.

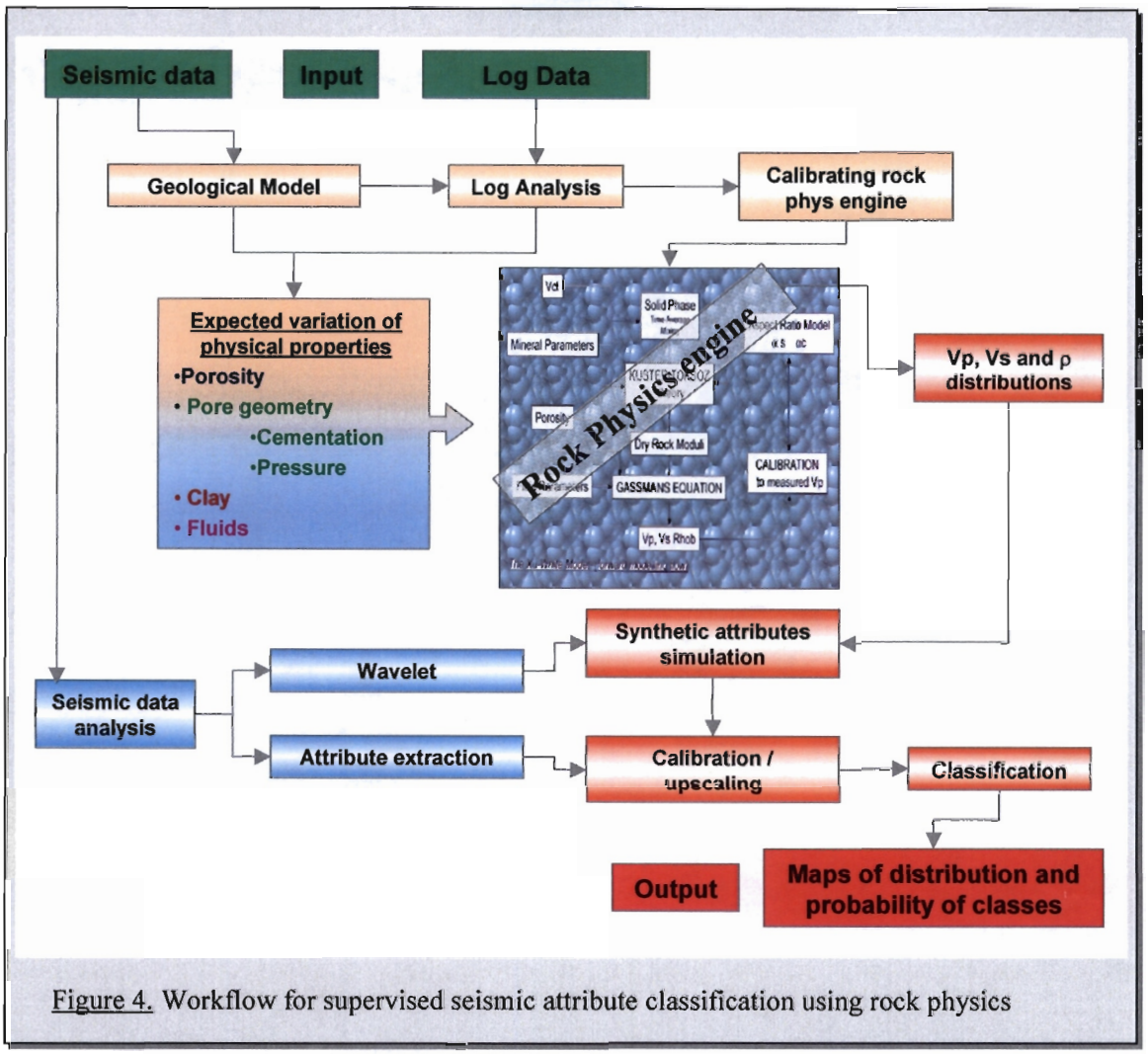

Figure 4. Workflow for supervised seismic attribute classification using rock physics

Geological model

The workflow starts with the generation of a geological framework and depositional model. The main aim of this part of the workflow is to define the subsurface geometries in 3D and understand the paleo-depositional environment of the rocks. The interpretation of both log and seismic data is essential for this step. An interpreter may start by evaluating data from a borehole. The type of rocks encountered, and log and lab measurements of these rocks, are used to determine their age, composition and paleo-depositional environment. The log interpretation is then extended beyond the confine of the borehole by interpreting the seismic data. The seismic data also provide the structural components of the geological model, which include faults, sequence boundaries and horizons.

Seismic wave propagation through rocks is affected by their acoustic properties. These in turn are affected by certain geological parameters of the rocks. This means that geological parameters can be extracted from seismic data. Unfortunately this problem is non-unique. In other words, a number of combinations of geological parameters will give the same seismic response. The only additional information that can be used to determine the correct combination lies in the geological model. The geological model must thus be used to calculate expected variations of geological parameters away from well control points. In siliciclastic basins, these include:

- Rock composition (volume clay for example)
- Porosity
- Pore geometry
- Pore fluid composition

Rock physics evaluation

Rock physics provides the link between rock parameters and acoustic propagation. In section 3.1, some fundamental rock physics relationships were discussed. In the workflow presented here, they will be used to establish the relationship between rock and fluid parameters and seismic attributes. Most rock physics relationships need to be calibrated. Wireline log data are usually used to achieve this. For example, when establishing a velocity-porosity relationship, certain scalars in the formula need to be calibrated to real measurements of velocity and porosity. Once the relationships have been calibrated, seismic attributes associated with the expected range of lithologies and pore fluids can be calculated. These data can then be used to classify the seismic data. Since seismic data are lower frequency than wireline logs, all log-derived data need to be up-scaled to better match the seismic frequencies in this step. Up-scaling is simply a filtered resampling to a larger sampling interval.

Seismic attribute generation and classification

Seismic data are usually interpreted as stacked traces in the reflection domain. This is not necessarily the best format for lithology and fluid interpretation though. To achieve optimal fluid and lithology interpretations, the seismic data need to be transformed to suitable lithology and fluid attributes. The additional information contained in the amplitude variation with offset (pre-stack seismic data) needs to be included in these attributes. For quantitative seismic interpretation, the effect of the seismic wavelet needs to be accounted for as well. This can be achieved by inverting the seismic data. For this study, $\lambda\rho$ and $\mu\rho$ attributes were generated from pre-stack seismic inversions. These attributes, and their generation will be discussed in more detail in subsequent chapters.

The last step of the workflow involves the classification of the seismic attributes into various lithology and fluid classes. The probability density functions generated from the geological model and the rock physics relationships are used to do this. The results can be used to generate maps of the most probable classes, or probability maps of a specific class. In this way quantitative interpretations can be generated from the seismic data.

Prior to implementing the workflow outlined here, a feasibility study may be conducted. Such a feasibility study may be performed using a small dataset around the borehole, but would still require all steps of the workflow to be conducted, including inversion of seismic data.

4 Dataset and Geological Model

In this chapter, the study area and its dataset from the Bredasdorp Basin offshore South Africa will be introduced. The implementation of the first part of the workflow for quantitative seismic interpretation, as outlined in the previous chapter will also be discussed in detail. A location map of the study area is shown in Figure 5. The area of interest lies in the west central Bredasdorp Basin, around borehole E-BX1, where water depths are about 120 m. The interval of interest is the Aptian 13B sequence, which is buried at a depth of roughly 2500 m below sea level in the study area. Borehole E-BX1 intersected two sandstone units in the 13B sequence, the upper being 51 m thick and the lower 22 m. Both sandstones are water wet.

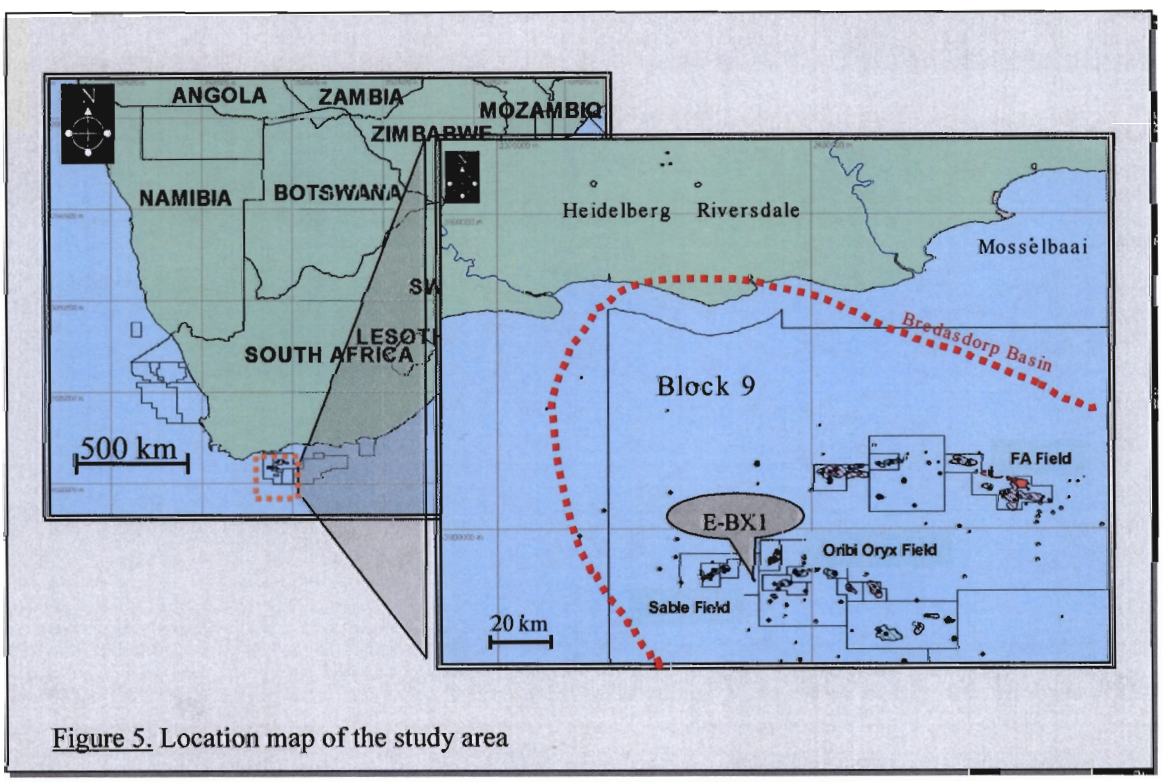

Figure 5. Location map of the study area

The sequence stratigraphic nomenclature for the Bredasdorp Basin was established by Soekor E&P during their initial oil exploration phase. The nomenclature assigns numbers to major post-rift sequences in chronological

order, starting with 1 for the oldest post-rift sequence. The major unconformities upon which a particular sequence was deposited generally carries the same name (number). In this way, sequence 13B was deposited on the type 1 unconformity 13Bt1.

4.1 Log data and log analysis

Borehole E-BX1 was drilled by Soekor E&P in 1990, in the west central Bredasdorp Basin (Figure 6). The borehole was logged, before it was plugged and abandoned as a dry hole.

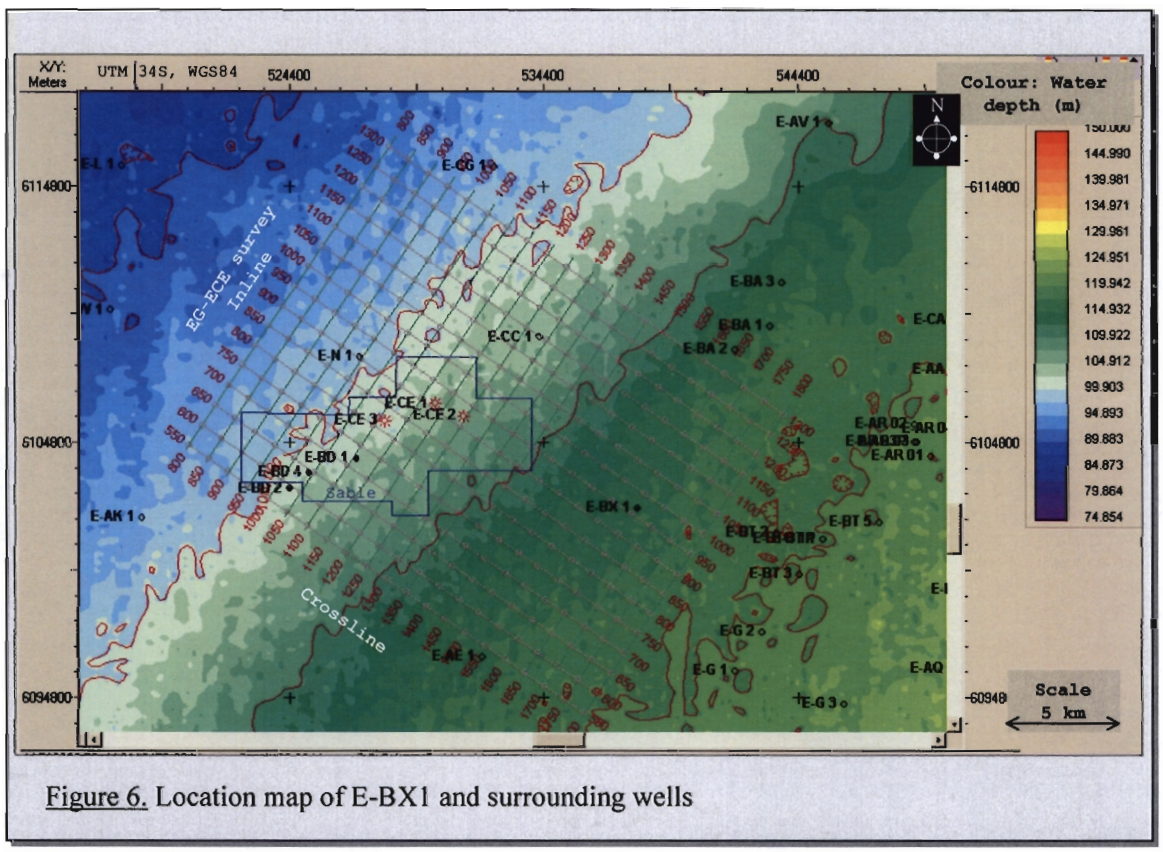

Figure 6. Location map of E-BX1 and surrounding wells

A standard suite of logs was acquired over the deeper part of the borehole. This included:

- Natural gamma ray log
- Litho density log
- Resistivity (Laterlogs)

- Sonic log

Schlumberger conducted the logging acquisition and processing, and supplied raw, and borehole corrected logs to Soekor E&P. In this study, the log data are used for the following purposes:

- Sonic and density logs for synthetic seismic attribute generation and inversion, as well as calculation of sonic log.
- Resistivity logs for determination of fluid saturation, Gassmann fluid substitution, and overall quality control
- Gamma ray logs for lithology determination
- Caliper log to detect bad hole conditions

4.1.1 Sonic and Density logs

Figure 7 shows the velocity and density logs over the 13B interval. The velocity log is calculated from the sonic log, which records formation slowness, and the density log is derived from the litho-density log.

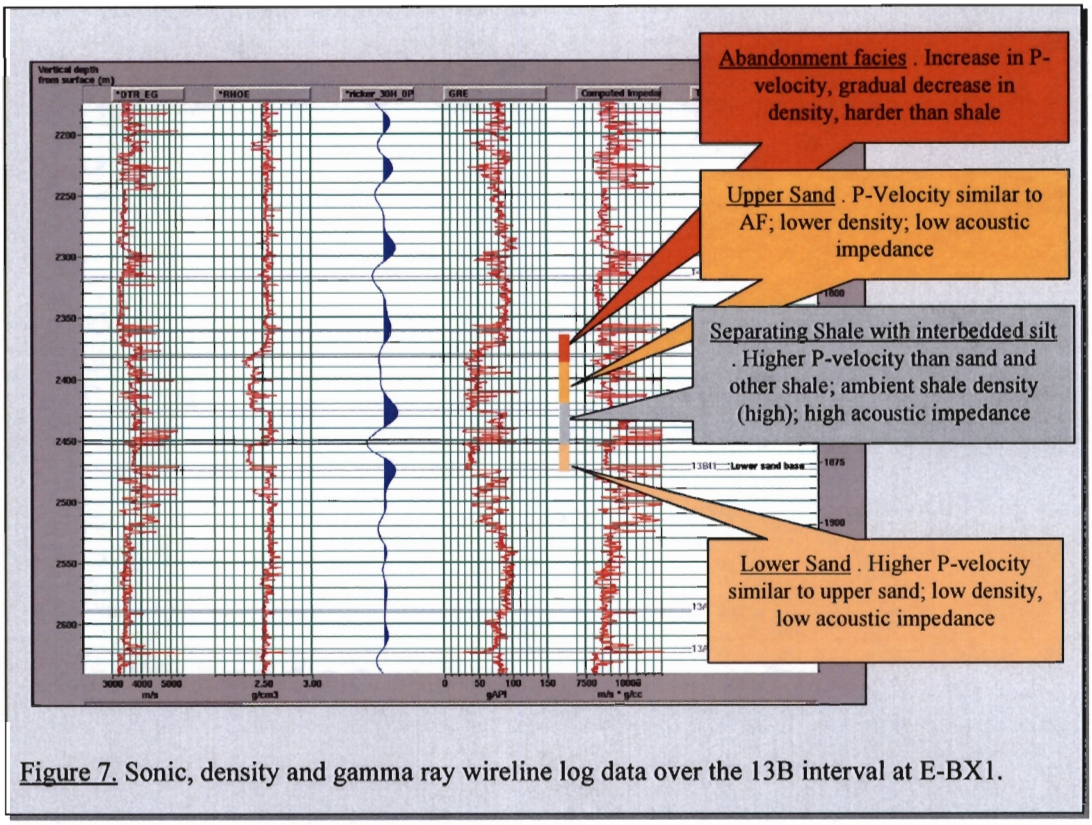

Figure 7. Sonic, density and gamma ray wireline log data over the 13B interval at E-BX1.

A sonic logging tool consists of a transmitter, which emits a sound pulse, and a receiver, which records the transmitted signal. The slowness is then determined by the time taken for the wave to travel from source to receiver (Figure 8).

The Litho-density tool consists of a chemical gamma ray source, and a gamma ray detector. The gamma rays interact with the formation in various ways, and are scattered back to the detectors. From the amount and type of backscatter, the density and lithology are derived (Figure 8).

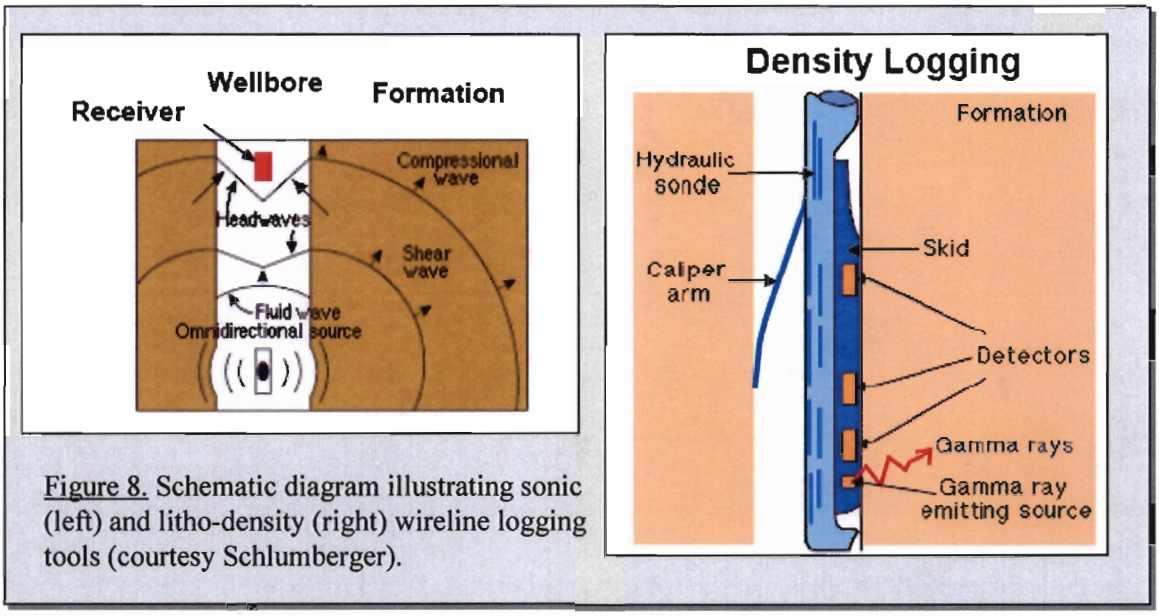

Figure 8. Schematic diagram illustrating sonic (left) and litho-density (right) wireline logging tools (courtesy Schlumberger).

Both the sonic and the density logs have a very shallow depth of investigation. This means that the tools record the immediate proximity of the borehole wall. In bad borehole conditions, where the borehole wall is rugged due to washouts, these tools will yield incorrect readings. For this reason the measurements are "borehole corrected". Another significant source of error in the sonic and density readings can occur if invasion of the drilling fluid into the formation occurs. Boreholes are drilled with a drilling fluid in the hole. This fluid circulates cuttings to the surface, lubricates the drilling process and stabilizes the borehole pressure. The fluid is usually a saline mixture (water based), but can also be an oil-based fluid. In permeable formations, the drilling fluid enters the pore space and displaces the original pore fluid. This process is called invasion (Figure 9), and changes the density and velocity of the formation around the borehole. This change occurs when the invading fluid is different from the original fluid. For example, if a borehole was drilled through an oil or gas bearing permeable formation with a water based mud, the sonic and density log will record values associated with the mud filtrate rather than with the oil or gas, since the depth of investigation is too shallow. The density tool's depth of investigation is generally shallower than that of the sonic tool, making the density invasion more severe than that of the sonic log. Both the sonic velocity and the density values recorded will be too high, since

hydrocarbons generally have a lower density and velocity than water. To correct the invasion effect, the amount of invasion needs to be determined. In other words, the volume ratio (or saturation) of the invading fluid versus formation fluid needs to be determined. Once this has been established, a linear correction for density is applied. The magnitude of this correction is determined by the relative difference of invading versus original fluid density, and their saturations. The sonic invasion correction is more complex, since it needs to be corrected through two steps of Gassmann fluid substitutions (Alberty, 1994).

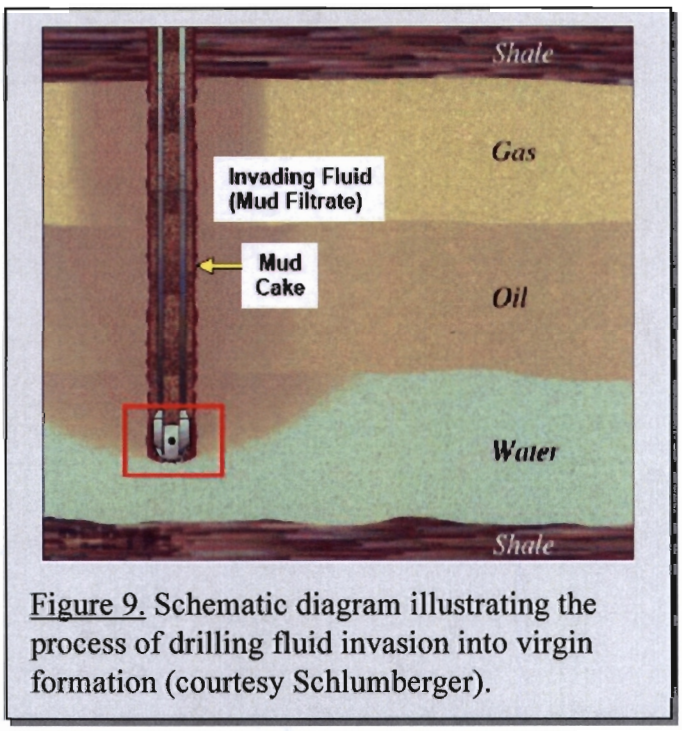

Figure 9. Schematic diagram illustrating the process of drilling fluid invasion into virgin formation (courtesy Schlumberger).

Determination of the amount of invasion is achieved with the resistivity logs (section 4.1.2). Borehole E-BX-1 was drilled with a water-based mud. After investigating the invasion effect, it was determined that although invasion may have occurred over the two 13B sandstone intervals, there is little difference between the acoustic properties of the mud filtrate, and the virgin formation water. This implies that further invasion-corrections on the logs are unnecessary.

4.1.2 Resistivity logs

Resistivity logging tools have an electric current source, which creates a series of equipotential surfaces around the source. The resistance of the formation is determined by measuring the current and potential difference in the circuit. Depending on the configuration of the tool, the resistivity can be measured at various distances (or depths) from the source. This implies that resistivity measurements can now be made in the invaded zone, close to the borehole, and in the virgin zone, further away from the borehole. Since the pore fluid resistivity contributes largely to the overall resistivity, invasion can be detected by comparing resistivity readings at different depths of investigation. Archie's equation can then be used to determine the virgin fluid resistivity and saturation. Using this formula, it was determined that both 13B sandstone units are water-bearing, and that the water resistivity of the 13B sandstone is 0.125 Ω.m, at a temperature of 74^{0}C (Klimentos, 1991). This corresponds to a salinity of 23 000 ppm NaCl, which in turn corresponds to a fluid density of roughly 1.03 g/cc and velocity of 1520 m/s. The density and velocity were calculated from the Batzle and Wang equations (Batzle and Wang, 1992). Since the fluid properties of the drilling mud are known, they can now be compared to those of the formation water. If a significant difference between the two exist, then an invasion correction through fluid substitution is necessary. In the case of the 13B sandstone units at E-BX1, no invasion corrections were required. The results of the resistivity log evaluation will be used for the synthetic attribute generation, where fluid substitution is required (chapter 5).

4.1.3 Porosity and Gamma ray logs

Porosity logs are usually derived from one of the following logs:

1. Neutron log
2. Density log
3. Sonic log

The neutron tool consists of a chemical or an electronic high-energy neutron emitter, and neutron detectors. The high-energy neutrons slow down to thermal levels via elastic scattering, mainly due to the collision with the hydrogen atoms in the formation, both in the fluid and the matrix. Assuming that the majority of the hydrogen atoms are present in the water or hydrocarbons in the pore spaces, and the pore fluid is know, the formation porosity can be determined.

Porosity calculated from the density or sonic log assumes that the density and velocity of the rock matrix and the pore fill are known. The porosity is then determined by calculating the relative amounts of matrix and pore-space, to match the recorded density or sonic.

Since no neutron log was acquired in borehole E-BX1, the density log was used to derive the porosity log. The sandstone component of the matrix was assumed to be quartz. The amount of sandstone and clay was obtained from the volume clay log, which is calculated from the gamma ray log. The following formula outlines the relationship between densities, porosity and volume clay.

$$\rho_b = (1-\phi)\left[\left(V_{qtz} * \rho_{qtz}\right)+\left(V_{CL} * \rho_{sh}\right)\right]+\left(\phi * \rho_{fl}\right) \qquad (6)$$

ρ_b bulk density

ρ_{qtz} quartz density

ρ_{sh} shale density

ρ_{fl} pore-fluid density

ϕ porosity

V_{qtz} volume proportion of quartz (=1- V_{CL})

V_{CL} volume proportion of shale

These data were then used to calculate the pore fluid properties from the resistivity log evaluation (section 4.1.2). No core was cut in E-BX1; otherwise

laboratory determined core porosities could have been used to calibrate the porosity log. The two 13B sandstone units at E-BX1 have relatively high porosities, varying from 16% to 18%.

A gamma ray (GR) tool records the natural gamma rays emitted from a formation. It consists of a detector and associated electronics to measure the gamma radiation originating in the volume of the formation near the borehole (Figure 10). The GR log has many applications, but is mostly used as a quantitative shale volume evaluator. Shale usually contains naturally radioactive elements, whereas clean sandstone usually does not. The GR log can thus be used to calculate the volume of shale in a formation. The assumption that clean sandstone is not radioactive does not always hold true, since sandstone can contain radioactive elements such as uranium. If uranium is known to occur in the area, then a spectral gamma ray tool is employed. This tool can differentiate radioactive source elements. In E-BX1, no occurrence of radioactive sandstone is known, and thus a normal GR log was run, and used as sand – shale differentiator. The GR log over the two 13B sand intervals at E-BX1 is shown in Figure 7.

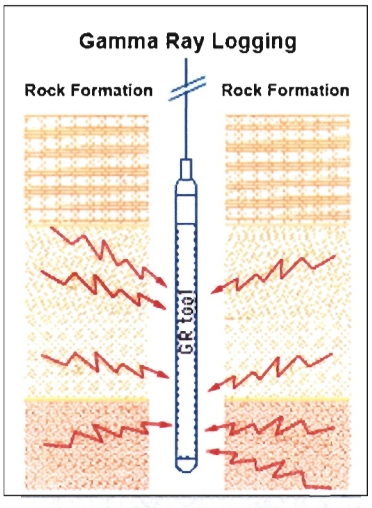

Figure 10. Schematic diagram illustrating a typical gamma ray wireline logging tool (courtesy Schlumberger).

4.2 Seismic data acquisition and processing

The 3D seismic data that are used for the study were shot in 1996. The data consist of approximately 15,800 km subsurface lines, covering 550 km^2 (Figure 6). The survey was shot by the Geoco-Prakla's *M/V Sapphire,* using two airgun sources and four 3000 m, 250-channel streamers. This acquisition geometry gives 50 fold seismic data. Recording time was limited to 5.120 seconds, at a 5 ms sample interval. The nominal acquisition bin size was 6.25 m x 37.5 m. The vessel acquired 8 subsurface lines in one pass with this configuration.

During 2001, Soekor E&P decided that the seismic data were not of sufficient quality for detailed amplitude analyses. Of main concern were the high levels of remaining noise in the data (both pre- and post-stack). This prohibited amplitude and AVO interpretation. The data were thus reprocessed at CGG (Compagnie Générale de Géophysique), in London. The reprocessing sequence was designed for maximum noise attenuation, whilst preserving amplitudes. The key noise-reducing processes are listed below:

Pre-stack noise attenuation processes

Swell noise attenuation

Tau-p noise attenuation

Despiking

External noise attenuation

Random Noise Suppression and Inline Interpolation

Demultiple

Post-stack noise attenuation processes

Frequency slice filtering

The frequency slice filtering was particularly successful. It converted the data into the frequency-space (f-x-y) domain and then performed a 2D median

filter on each frequency "slice". Parameters were chosen by scanning a range of filter sizes, across all frequencies, and then comparing the outputs at every 10 Hz. It was noted that the process was particularly effective at removing amplitude variations due to acquisition geometry

The data were also pre-stack time migrated. This approach produces better pre-stack data for AVO analyses.

A comparison of the original data, and the reprocessed data is shown in Figure 11. The reprocessed section appears smoother with much of the random and coherent noise and amplitude banding removed. The fact that the faults are imaged better, suggests that the reprocessing is a valid enhancement.

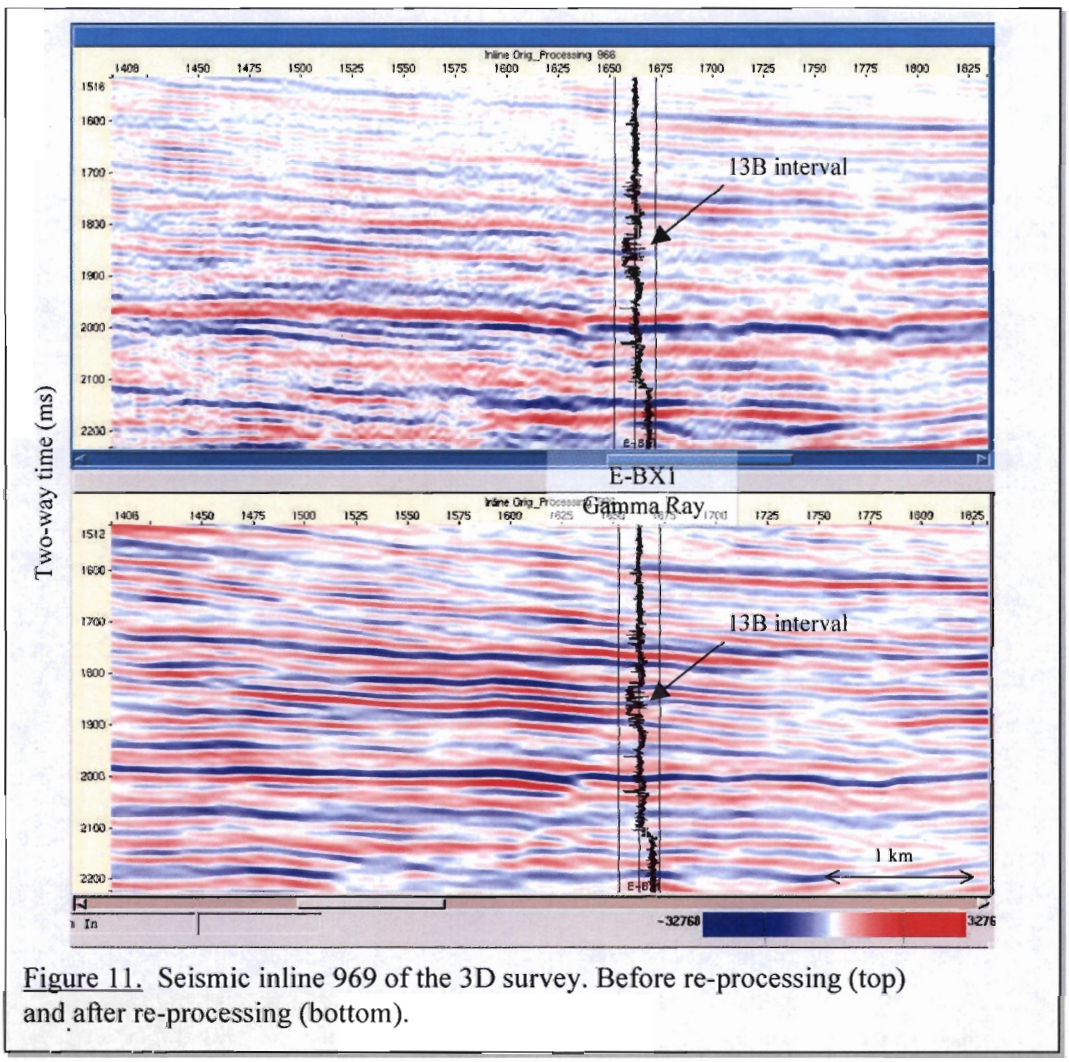

Figure 11. Seismic inline 969 of the 3D survey. Before re-processing (top) and after re-processing (bottom).

4.3 Seismic interpretation

The 13Bt1 unconformity formed during a third order sea level lowstand. On seismic data, it is generally recognised as a positive increase in acoustic impedance, which corresponds to a peak (black or red event) in the seismic data displayed in this study. The 13Bt1 marker at E-BX1 and surrounding boreholes was used to guide the seismic interpretation of the 13Bt1 unconformity. Figure 12 shows a two-way time map of the unconformity. Since the sediments above this horizon are not associated with strong lateral velocity variations, the general shape of the time pick will be preserved in depth, and may thus indicate the general shape of the 13B paleo-basin. E-BX1 is located roughly 6 km SE of the base-of-slope. The basin is gently dipping southeast at E-BX1.

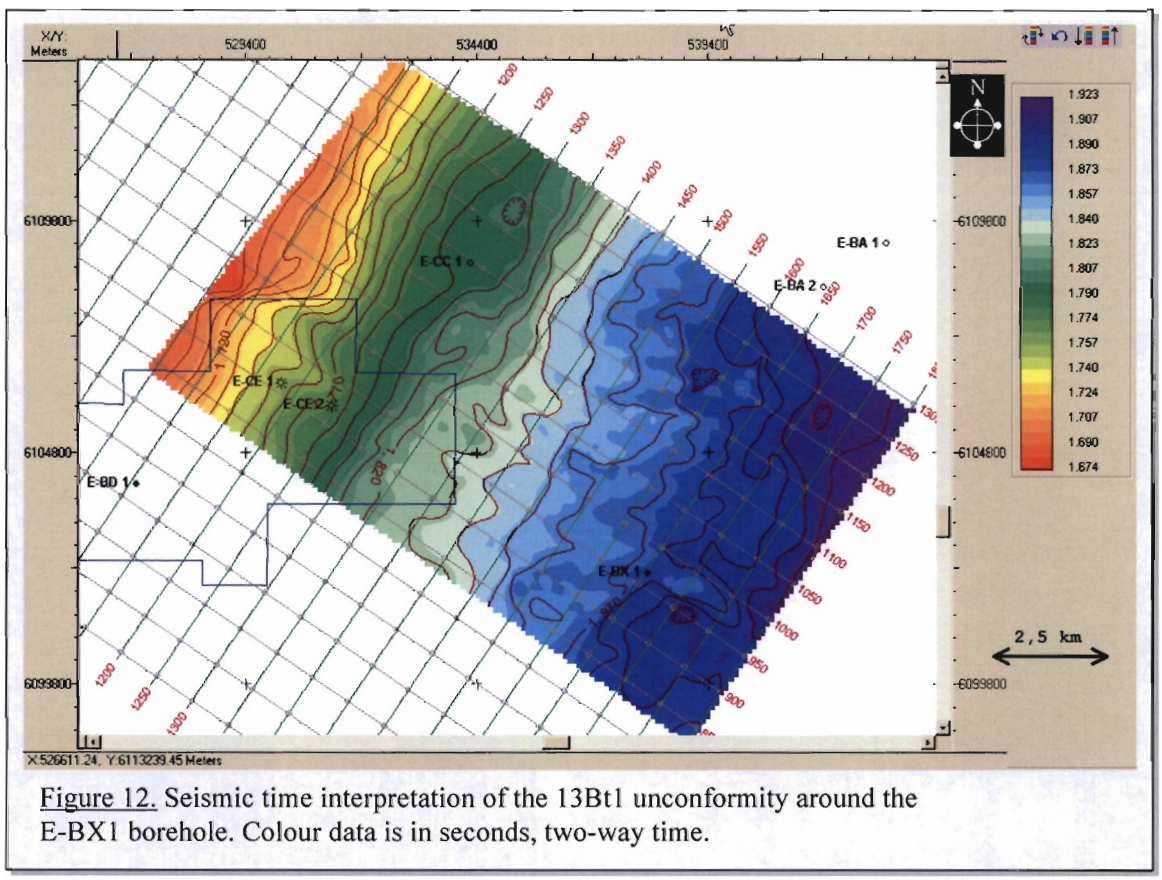

Figure 12. Seismic time interpretation of the 13Bt1 unconformity around the E-BX1 borehole. Colour data is in seconds, two-way time.

A number of graben-type faults were recognized in the 13B system around E-BX1. These faults controlled sediment deposition by creating a local depocenter northwest of E-BX1. Three graben-type faults were mapped around E-BX1 (Figure 13). The configuration is that of an east-west trending graben. This structure created accommodation space at 13B times, causing deposition of a locally thick 13B sandstone succession.

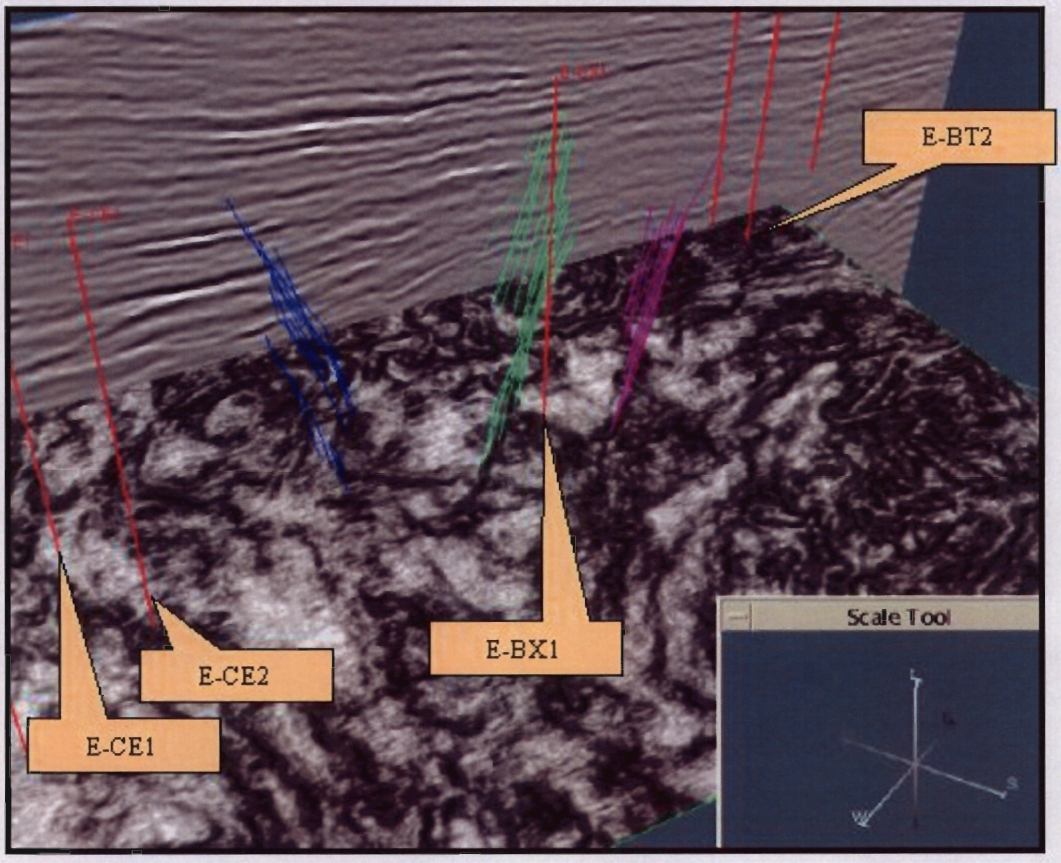

Figure 13. 3D view from southwest showing fault sticks of three graben-type faults around E-BX1. 3D view composed of horizontal coherence time slice and vertical 3D seismic in-line.

The prograding, lower 13B sand unit at E-BX1 directly overlies the 13Bt1 unconformity. The reflection from the base of the sand unit coincides with the 13Bt1 pick at borehole E-BX1. The 13Bt1 interpretation was thus used to extract lower sand attributes from the seismic data. In order to investigate the upper sand distribution, the trough relating to the reflection from its top, was

picked around E-BX1. Figure 14 shows a map of the two-way time pick along the top of the upper 13B sandstone. This pick was used to extract upper sand attributes from the seismic data.

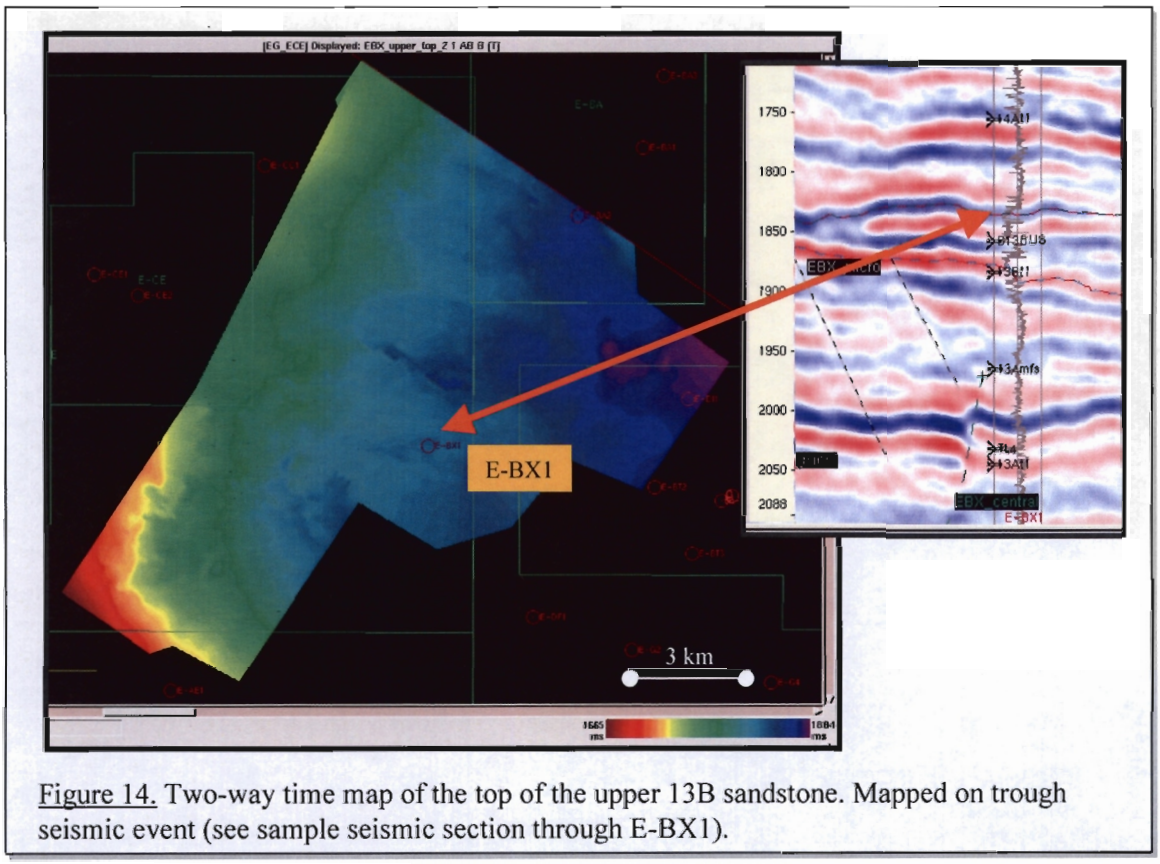

Figure 14. Two-way time map of the top of the upper 13B sandstone. Mapped on trough seismic event (see sample seismic section through E-BX1).

4.4 Geological model

The two 13B sandstone units at E-BX1 are massive with minor clay and dolomite stringers. Their stratigraphic location within the Bredasdorp Basin stratigraphic framework is shown in Figure 15 (compiled from information by Brown et al., 1995).

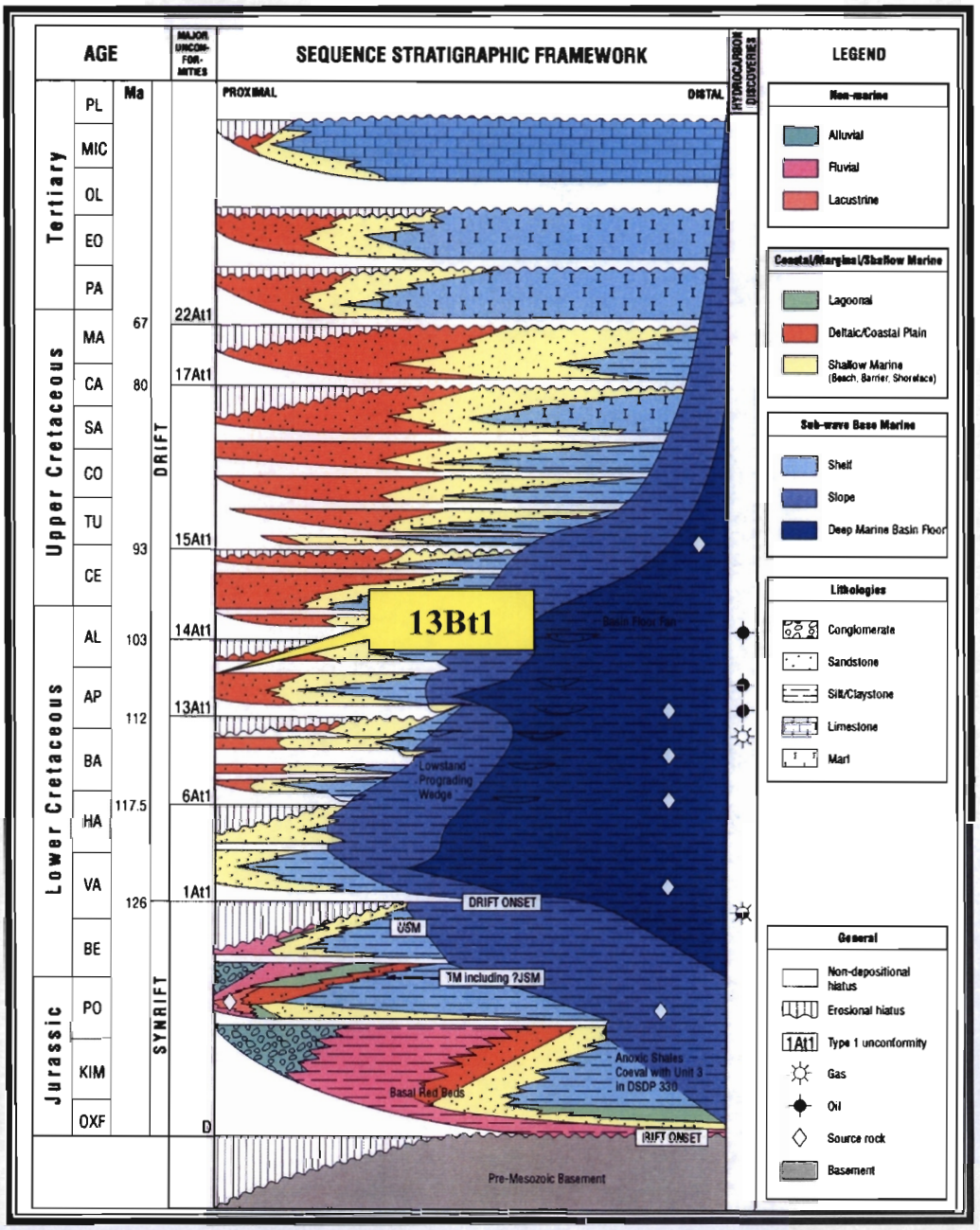

Figure 15. Sequence stratigraphic chart of the Bredasdorp Basin.

The 13Bt1 unconformity was picked at the base of the lower 13B sandstone, at the top of an underlying sand and clay succession. The sand lenses in this succession are pervasively cemented with calcite. One 3 m thick sand lens exhibits oil shows. This suggests that hydrocarbons migrated through the system but were only trapped in isolated sand lenses with low permeability.

The lower 13B sandstone is characterised by an upward coarsening and thickening succession of interbedded sandstone and claystone. These are interpreted as prograding units, overlying the 13Bt1 unconformity (Figure 7). No hydrocarbon shows were observed in the lower unit.

A 15 m thick layer of shale and interbedded silt separates the upper and lower 13B sandstone units. Some of the silty layers are calcite-cemented, similar to the silt layers in the succession underlying the lower massive sandstone (Figure 7).

The upper unit consists of a massive to interbedded 51 m thick sandstone with occasional clay and dolomite stringers. (Figure 7). The sand has a porosity range of 15% to 20%. No hydrocarbon shows were observed in the sandstone.

The upper sandstone is overlain by an upward fining, interbedded abandonment facies.

A regional geological model for the 13B sequence was generated by Soekor E&P. Their model characterises deposition of 13B basin sediments as slope-front and basin-floor prograding turbidites. The porosity in sandstone of the 13B sequence is mainly of a secondary type. Due to the high concentration of calcite, most sands were cemented soon after burial. The calcite was derived from shelly material off the shelf and concentrated close to the basin margins. The shelly material was dissolved, and circulated through the permeable 13B sandstone. Deposition of the calcite in the pore space cemented the primary porosity. Thin sand lenses were pervasively cemented, whereas thick 13B sand units retained some primary porosity. The retained primary porosity in the thick sands allowed entry of leached acids, formed during organic maturation of shale, to circulate through the sandstone at a later stage. This acid dissolved the calcite and formed a secondary porosity (Fraser and Winters, 1996). It is for this reason that the thin sands underlying the lower

13B sandstone at E-BX1 have a very low porosity, whereas the two thick sandstone units have a high porosity. Porosity in the 13B sandstone ranges from 11% to 23%. The grain size of the 13B sandstone varies from east to west from very fine to medium. The very fine material is well sorted whereas the sandstone with a medium grain size is poorly sorted. This inverse relationship has been attributed to different provenances for the eastern and western 13B deposits (Fraser and Winters, 1996). Glauconite content in the 13B sequence is in the order of 5%, indicating a relatively slow rate of deposition.

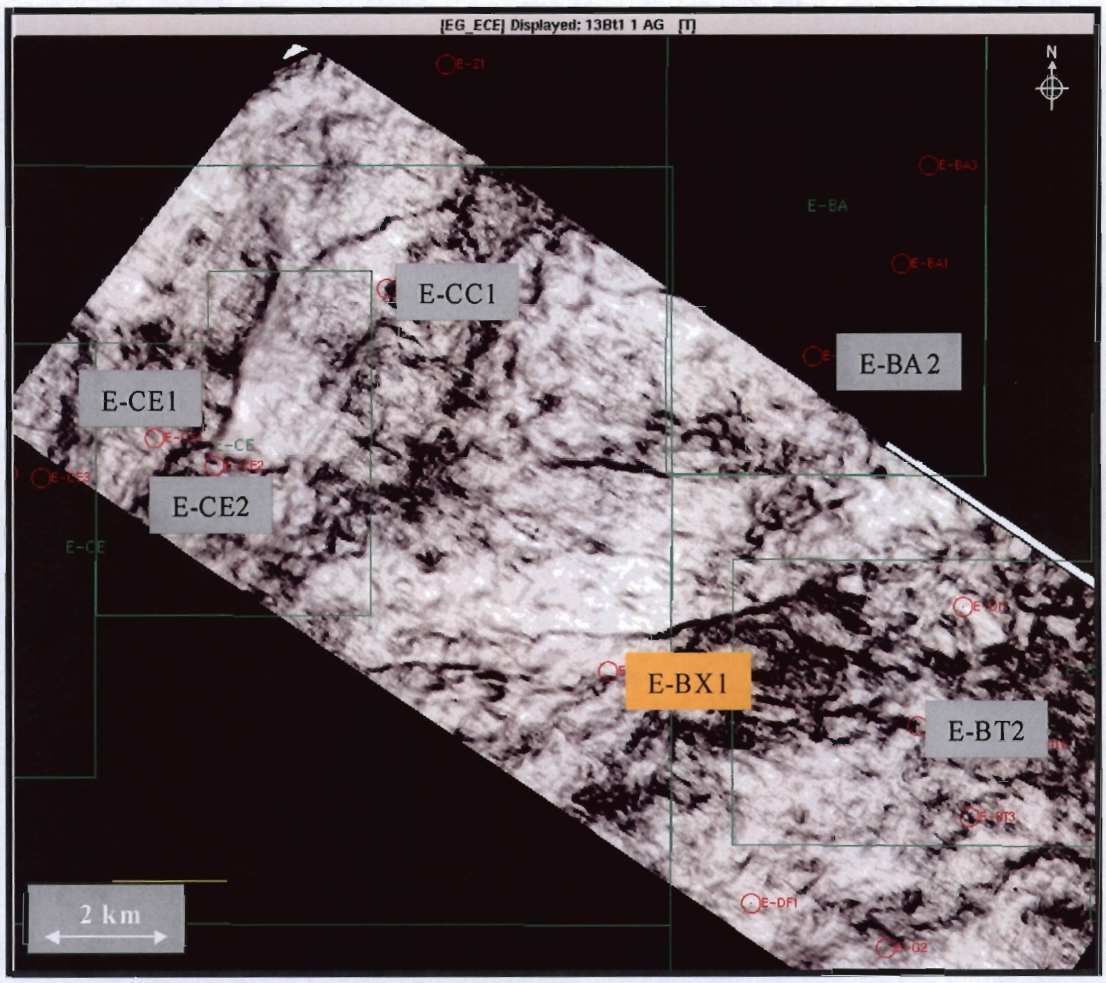

Figure 16. Coherence map extracted along the 13Bt1 unconformity. The map shows depositional and structural features relating to the lower 13B sandstone.

The E-BX1 sandstone was sourced from the west, where a large canyon (the 13Bt1 channel) has been identified on 2D seismic data. This channel lies roughly 15 km west of E-BX1. Regionally, the 13B sequence comprises only thin sandstone layers. The thick sandstone at E-BX1 formed due to the presence of a local depocentre.

Seismic amplitude and variance maps were used to assist in the generation of a local, 13B E-BX geological model for this study. The lower, upward coarsening sandstone unit directly overlies the 13Bt1 unconformity at E-BX1 and is associated with the first stage of basin-ward progradation. Lowstand oblique progradational wedges that downlap onto 13Bt1 can be identified on seismic data in an area encompassing the E-CE, E-CC1 and E-BX1 wells (Figure 16). The configuration of these prograding wedges suggests a broad sediment input from the west. This is in agreement with the basin configuration at 13B times. The basin-floor graben structure northwest of E-BX1 acted as a depocentre to higher energy turbiditic sediments emanating from the lowstand progradation. The lower, upward coarsening unit at E-BX1 is related to this progradational deposition. Since these sediments have a line source (the paleo-slope), they are not confined to individual channels, but rather exhibit a sheet-like depositional style. This can be seen on the variance map extracted along 13Bt1 (Figure 16). The sheet sandstone deposited in this manner may interfinger with the distal parts of the prograding wedges.

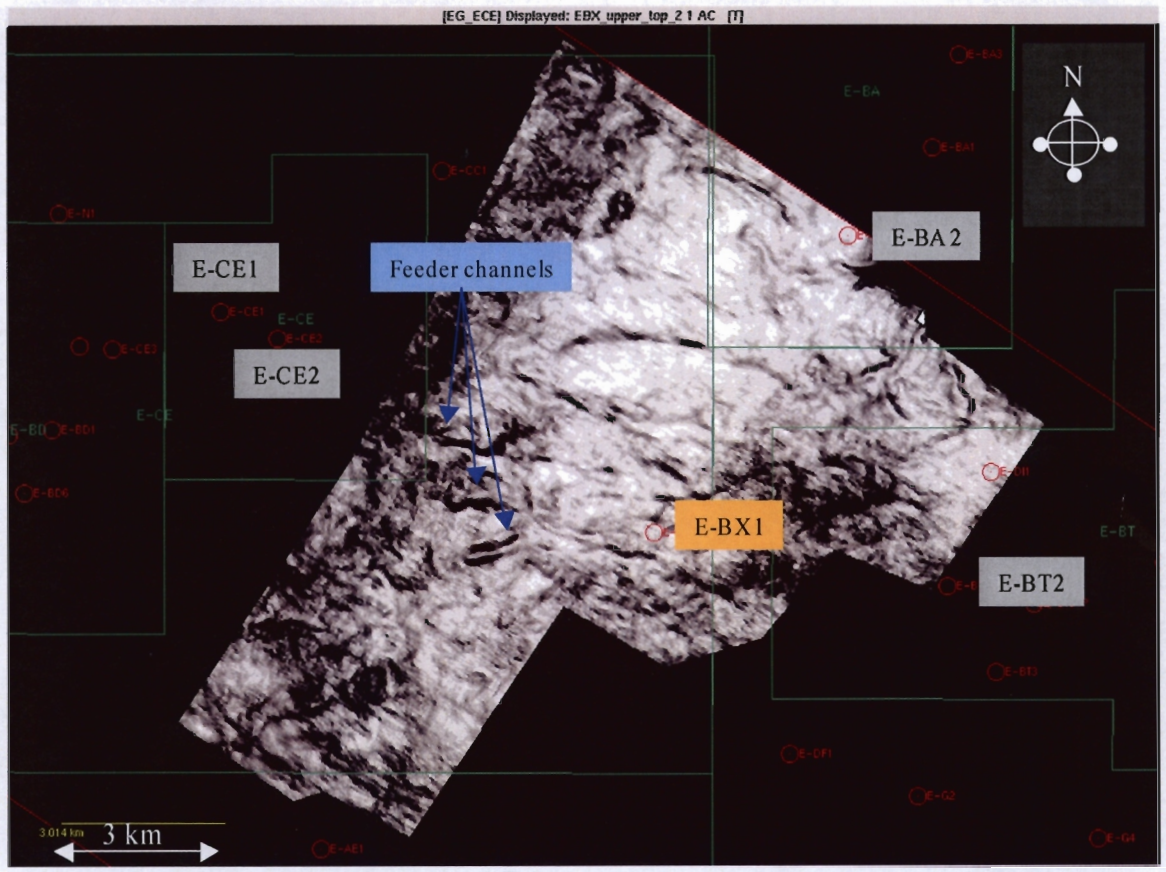

Figure 17. Coherence map extracted along upper 13B sandstone reflector. The map shows depositional and structural features related to the upper 13B sandstone unit.

As equilibrium between relative sea-level rise and sediment input was reached, progradation of the slope ceased, and relative sea-level rise caused a period of shale and silt deposition. This is evidenced by the 15 m interbedded shale and silt layer separating the upper and lower 13B sandstone units at E-BX1 (Figure 7).

Following the deposition of the interbedded shale and silt, a small relative sea level drop occurred, and with renewed energy, transportation of sediments into the basin occurred in the form of turbiditic channelised flows. The upper sandstone unit at E-BX1 is associated with this type of deposition. The coherence map extracted along the reflection of the upper sandstone top shows three individual feeder channels to the west of E-BX1 (Figure 17). These channels are cutting into the western boundary of the graben system.

This incision could have been as a result of subtle (compactional) movements along the graben faults. After a further relative sea-level rise, the sediment supply along these channels was abandoned. The feeder channels are of limited updip extent, which is most probably as a result of sediment bypassing the proximal slope. As sediment input from the shelf weaned, the abandonment facies was deposited on the upper massive sandstone. Deposition of sheet drape hemipelagic shale over this incised channel system may create a top-seal. There is thus potential for a thick pile of sandstone, detached from the shelf, updip of E-BX1.

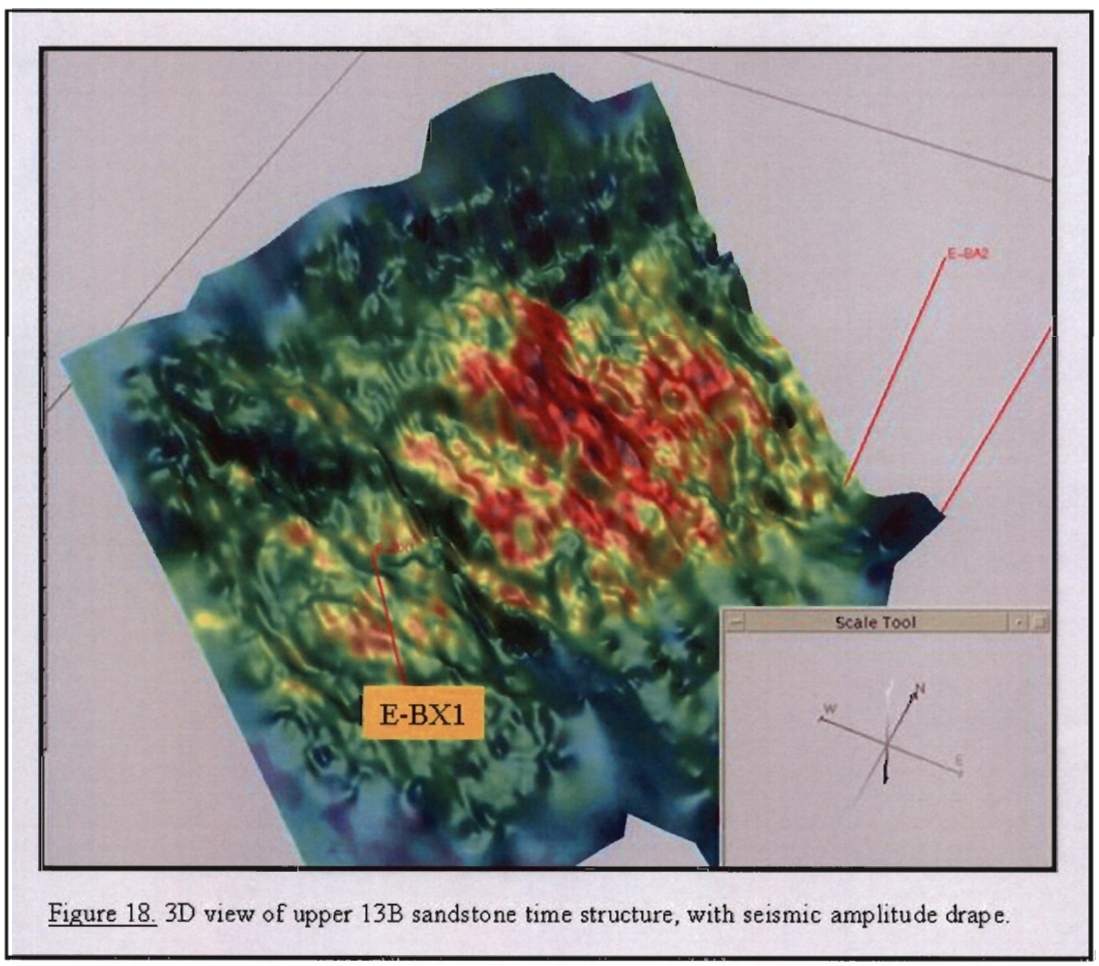

Figure 18. 3D view of upper 13B sandstone time structure, with seismic amplitude drape.

Extraction of seismic amplitudes along the upper sand-top reflection revealed a seismically anomalous zone to the north of E-BX1 (Figure 18). The seismic amplitude anomaly is associated with a structural nose into the graben. A random seismic section from E-BX1 to E-CC1 is shown in Figure 19. The

seismic response from the anomalous zone (hereafter referred to as "northern amplitude anomaly") suggests that it could be related to the upper sand unit at E-BX1. This would appear to increase the potential for hydrocarbon bearing sand up-dip of E-BX1. However, as will be shown in chapter 5, this interpretation is probably too simplistic.

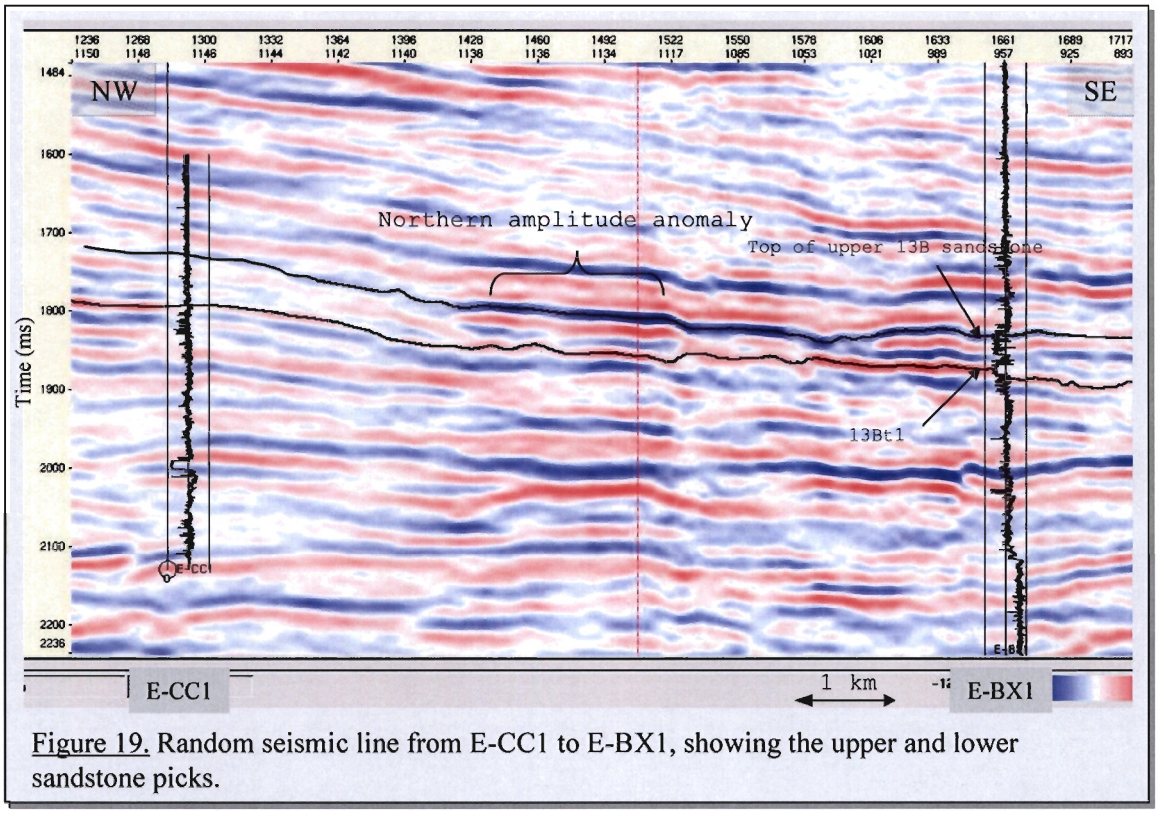

Figure 19. Random seismic line from E-CC1 to E-BX1, showing the upper and lower sandstone picks.

4.5 Synthetic seismogram tie

Both the log and the seismic data have been described in previous sections. Log data provide high-resolution information along the borehole trajectory, whereas seismic data provide lower resolution subsurface information over a large area. To integrate the two data types, they are "tied" at the borehole location. Two purposes of tying log and seismic data are to obtain a time depth relationship, and to estimate the phase of the seismic data. The time-depth relationship is used to plot log data on seismic lines at the correct two-way time.

Seismic data records the amplitudes and arrival times of reflections associated with subsurface layering. These data are not directly recorded by logging data, and need to be calculated from the density and sonic logs as a reflection coefficient log. The reflection coefficient log has a much higher frequency than the seismic data. For a meaningful well-tie, the reflection coefficient log is convolved with a zero-phase wavelet which has the same amplitude spectrum as the seismic data. The convolved product is referred to as a "synthetic trace". This trace is compared to the 3D seismic, to determine the optimum time and phase shifts for the tie.

The process outlined above is a post-stack synthetic tie, implying that the seismic data that were tied has been stacked, and the synthetic trace is a zero offset synthetic trace. Pre-stack seismic data can also be tied to well data, but information about the shear sonic velocities at the borehole is required. The full offset tie at E-BX1 is described in section 4.6.

The density and velocity of the 13B formations at E-BX1 are to a large extent controlled by the relative amounts of sand and shale, and also the porosity and amount of calcite cementation of the sandstone. The interbedded and pervasively calcite-cemented sand and shale succession underlying the lower 13B sandstone, is generally associated with the highest impedance. This is a result of a high density, and a high Vp, caused by pervasively cemented sand lenses, and the high density of the shale. The upper and lower 13B sandstone units are also associated with a high Vp, but a lower density than the underlying cemented succession, and also the separating interbedded shale and silt layer and abandonment facies overlying the upper 13B sandstone. This results in the upper and lower 13B sandstone units having a lower impedance than their encasing material. The top of the sandstone units are thus recognized as a trough event.

A normal incidence synthetic trace was calculated from the Vp and density logs over the 13B interval. This synthetic trace was used to tie the 3D seismic data to borehole E-BX1. Figure 20 shows the synthetic to seismic tie over the 13B interval. The blue trace is the synthetic, whereas the red trace is the 3D seismic trace closest to the well location. A window of 700 ms around the 13B interval was used for the tie.

The quality of a tie can be determined by the correlation coefficient (CC) between the seismic and synthetic traces. Besides the quality of the seismic and log data, the correlation coefficient is also affected by the following parameters:

- Time shift between seismic and synthetic traces
- Phase of the synthetic
- Type of wavelet for synthetic

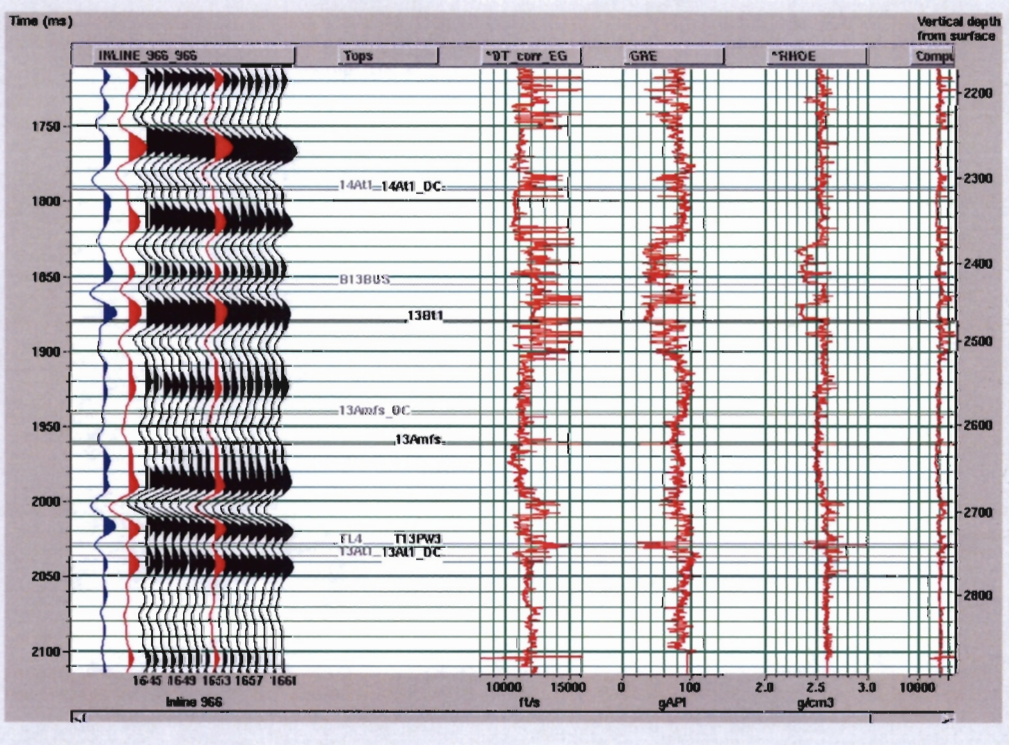

Figure 20. Normal incidence synthetic seismogram tie of E-BX1 log data to the 3D seismic data.

The phase of the synthetic needs to be adjusted to the seismic data. The phase cannot be determined by simply rotating the synthetic phase until a maximum correlation coefficient between the synthetic and the seismic is reached, since the correlation coefficient is also affected by time shifts. A global maximum of the correlation coefficient will reveal the most likely phase of the data, provided levels of noise in both seismic and log data are low. In order to determine the maximum correlation coefficient, the amplitude envelope, which is independent of phase, was used to determine the optimum time shift. After applying this time shift, the phase was rotated until a maximum correlation coefficient was reached. In this way, the phase and time shift of the seismic data can be approximated optimally.

In order to maximize the cross-correlation coefficient as outlined above, a phase of 62° needed to be imposed on the synthetic trace. The phase-rotated wavelet derived during the synthetic to seismic tie will be used for the seismic inversion. A maximum correlation coefficient of 73% was obtained for the E-BX1 tie, which is generally regarded a good 3D fit for the Bredasdorp Basin.

4.6 Vp Vs analysis

Acoustic wave propagation in a solid medium occurs as both primary (or pressure) and secondary (or shear) waves. The speed of propagation of these two waves differs, since it is governed by different elastic properties of the medium. The speed of pressure waves is denoted by Vp, and that of shear waves by Vs. The following formulae describe Vp and Vs in terms of the Lame's elastic parameters (section 5.1.1) and density:

$$Vp = \sqrt{\frac{K + (4/3)\mu}{\rho}} = \sqrt{\frac{\lambda + 2\mu}{\rho}} \qquad (7)$$

$$Vs = \sqrt{\frac{\mu}{\rho}} \qquad (8)$$

Vp – pressure wave velocity

Vs – shear wave velocity

K – bulk modulus

λ – Lame's elasticity parameter 'lambda'

μ – rigidity

ρ - density

Vp depends on λ, μ and ρ, whereas Vs only depends on μ and ρ. Since K and μ are always greater than zero, Vp is always greater than Vs. Shear waves are not transmitted through fluids, since their shear strength (or rigidity) is zero. Conventional offshore seismic data thus records mainly the P-waves, although some mode-converted energy from S-waves remains. This does not mean that the seismic data are unaffected by the Vs of the rocks; on the contrary, the Vp and Vs of the subsurface layers determines the amplitude variation with offset (AVO) recorded in the pre-stack seismic data. It is for this reason that a shear sonic log is required for a pre-stack seismic tie.

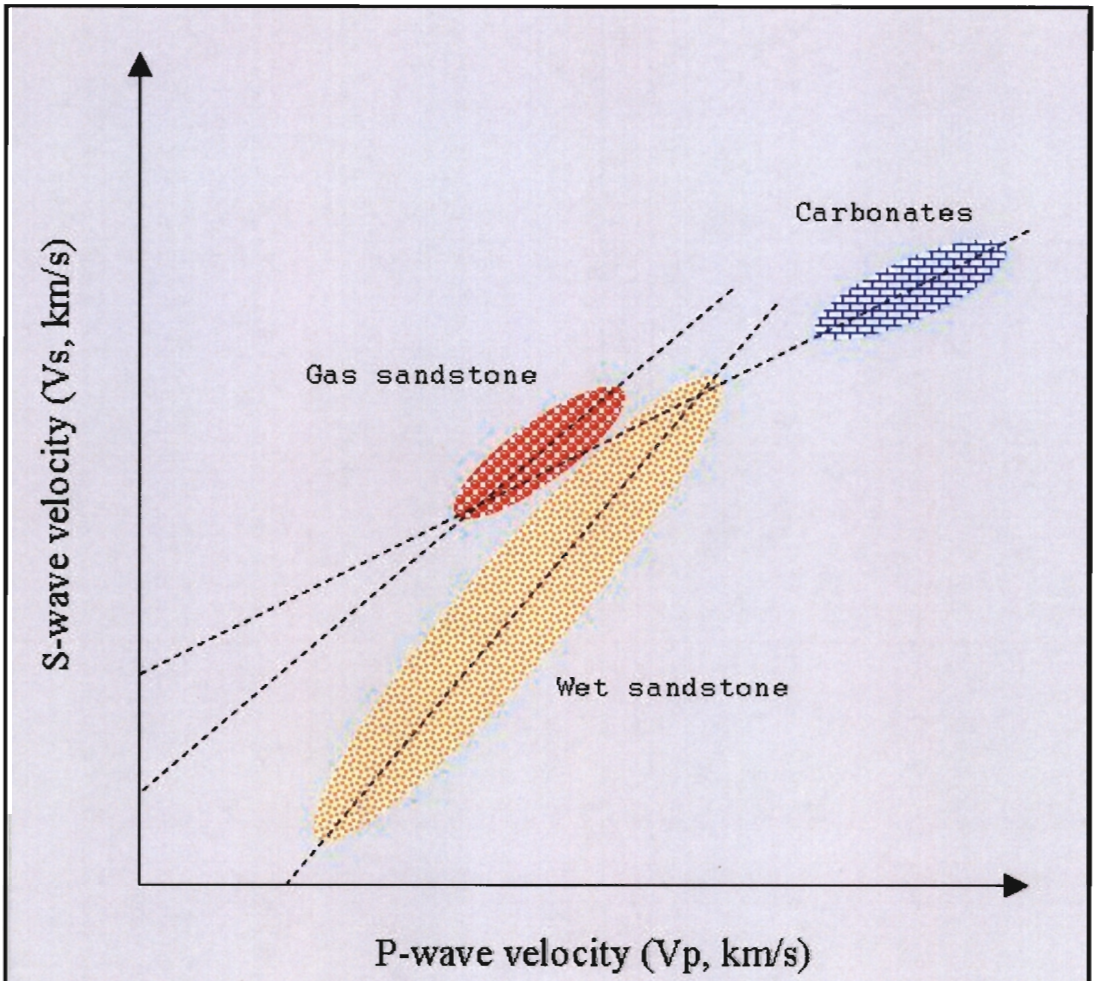

Figure 21. Sketch of typical Vp-Vs data for different lithologies and fluid fills

Unfortunately a shear sonic log was not run in E-BX1. In order to determine the Vs of the rocks, one must assume a Vp-Vs relationship, which is calibrated from shear sonic data from nearby wells. Castagna suggested an empirical equation relating Vp and Vs (Castagna et al., 1985). For sandstone and shale, a linear relationship is suggested;

$$Vs = a * Vp - b \qquad (9)$$

where a and b are constants calibrated to observed Vp and Vs data. Castagna noted a large difference between the constants "a" and "b" for water saturated and gas saturated sandstone (Figure 21). Castagna's most

recently published values of a and b for water-wet sandstone are (Castagna et al., 1993):

a = 0.804 (unitless)

b = 0.856 km/s

These values were derived from laboratory measurements of Vp and Vs on water saturated siliciclastics. It is important to note that the relationship needs to be calibrated locally, for reliable Vs estimations.

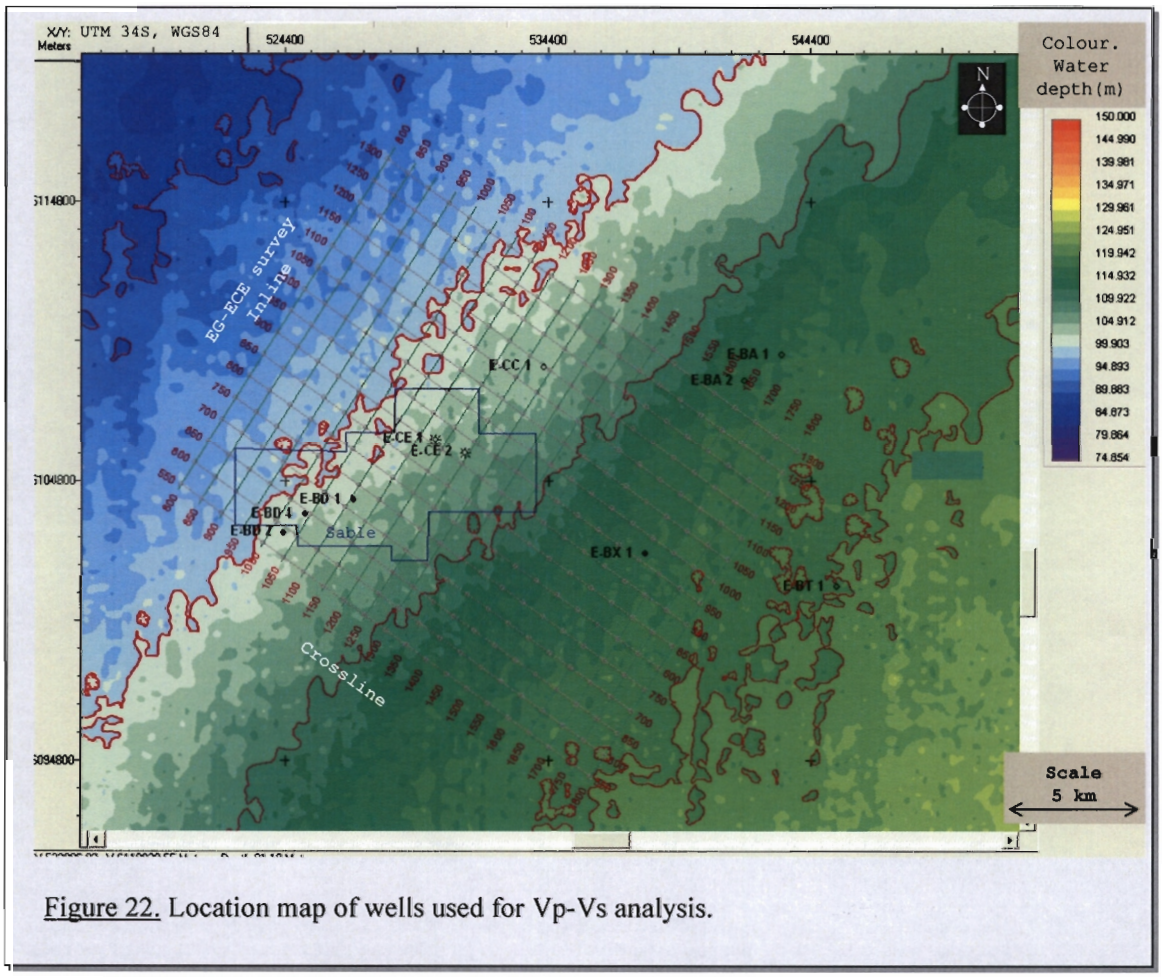

Figure 22. Location map of wells used for Vp-Vs analysis.

For the purposes of this study, two different approaches were followed to determine a Vp-Vs relationship for the 13B sandstone around E-BX1. They are:

1. Central Bredasdorp Basin calibrated Castagna relationship
2. Locally calibrated 13B Castagna relationship

As a first step, all the Vp and Vs logs were quality controlled for bad borehole conditions. Data recorded over bad borehole conditions were discarded. The central Bredasdorp Basin Castagna relationship was calculated from 10 wells in the central Bredasdorp Basin. The wells are shown in Figure 22.

As a further quality control, the range of Vp/Vs ratios calculated for each lithology and pore-fluid fill, was calculated and compared to published results. Figure 23 shows the range of Vp/Vs over the entire depth range for the various lithologies and pore fills, and also a similar plot published by Scott Pickford (Scott Pickford Core Laboratories, 2000). A good correlation is noted for sand and shale, but Scott Pickfords's Vp/Vs range for gas bearing sandstone is much narrower than that calculated from the ten Bredasdorp Basin wells. The reason for the discrepancy is probably related to invasion. Not all the sonic data from the Bredasdorp Basin were corrected for drilling mud invasion effects.

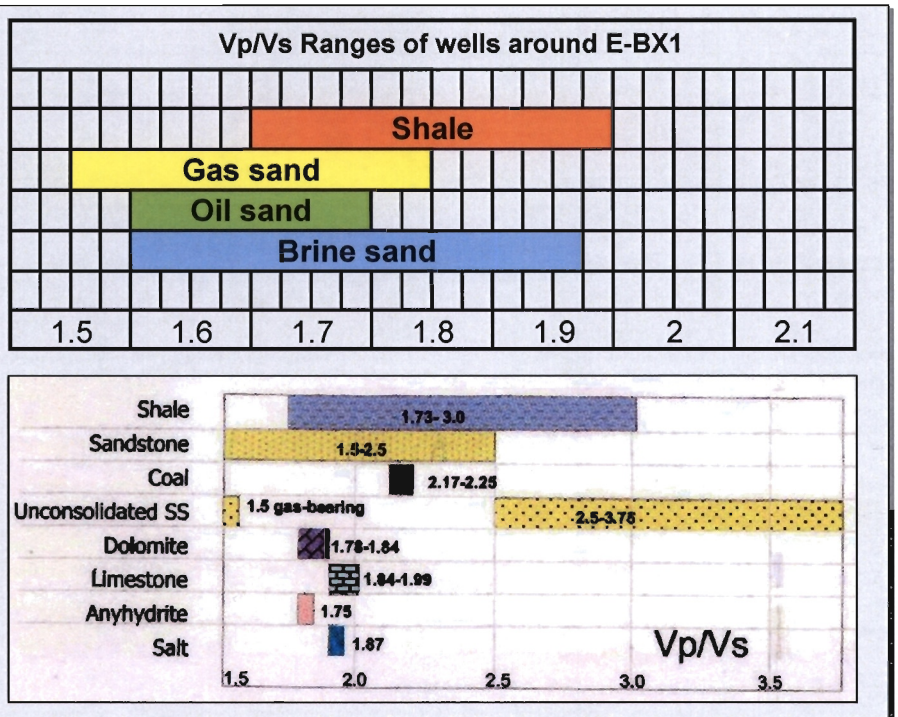

Figure 23. Comparison of Vp/Vs ratio ranges from 10 wells around E-BX-1 (top) and ranges published by Scott Pickford (Scott Pickford Core Laboratories, 2000).

Central Bredasdorp Basin calibrated Castagna relationship

Only the Vp and Vs log data around the 13B depth interval were used to determine a Castagna relationship. Since the 13B sandstone at E-BX1 is water-wet, only water bearing sandstone and shale data were used. Figure 24 shows the Vs Vp crossplot for the sandstone data, together with the best fit Castagna relationship, defined as :

$$Vs = 0.719Vp - 0.598 \quad \text{.....water-wet sandstone}$$

$$Vs = 0.696Vp - 0.519 \quad \text{.....water-wet shale} \quad \text{(km/s)} \qquad (10)$$

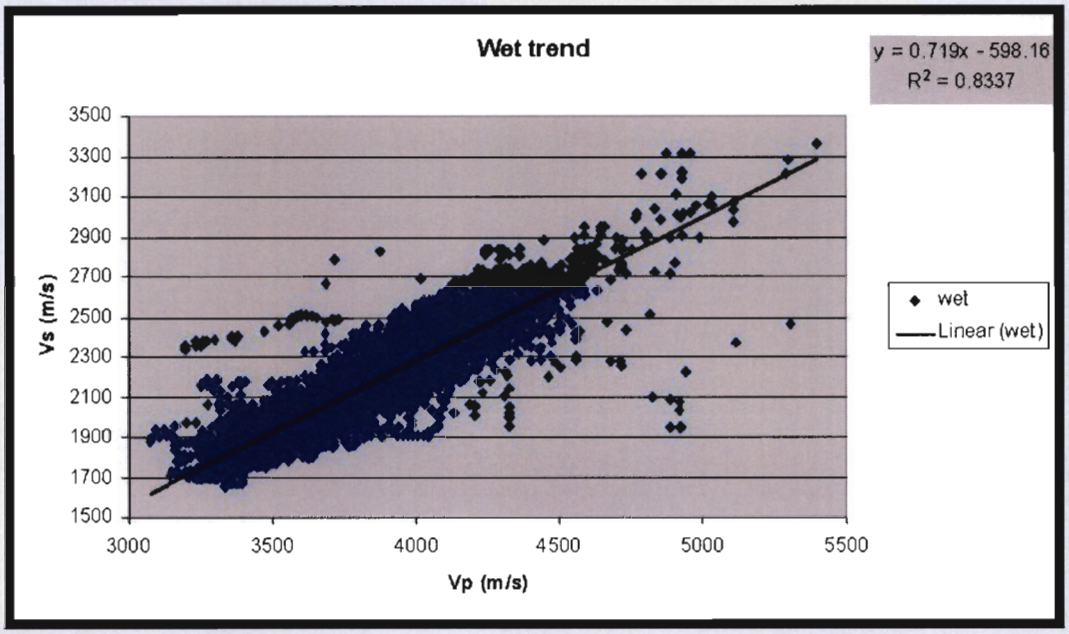

Figure 24. Linear fit to Vp and Vs data from wet sandstone intervals in 10 wells around E-BX1.

The variables "a" and "b" for sandstone are significantly lower than those determined by Castagna (Castagna et al., 1993). The Vp and Vs of the subsurface layers determines their AVO response on seismic data. A good check on the Vs values calculated with the central Bredasdorp Basin relationship, is to compare a full offset synthetic seismogram with the pre-stack seismic data around the well (provided the pre-stack seismic data are of

sufficiently good quality). A close resemblance between the two would suggest a correct Vp-Vs relationship.

In section 4.5, the zero offset, or normal incidence synthetic seismogram tie was discussed. The synthetic seismic trace calculated for the well tie, assumes that the seismic wave impinges vertically on geological layers, and is also reflected vertically back to the surface. In terms of seismic acquisition geometries, this would imply zero offset, since the source and receiver are coincident. At non-zero offsets, the seismic wave does not get reflected at right angles to the subsurface layers. The reflection and transmission coefficients controlling the propagation of the seismic wave now depend on the angle of incidence, and cause variations in the seismic amplitude with angle. This is the basis of AVO, since the angle of incidence is ultimately related to the offset between the seismic source and receiver. The Zoeppritz (1919) equations allow us to approximate full offset synthetic seismograms by calculating the AVO effects from the Vp, Vs, density logs and a seismic wavelet. A more detailed description of acoustic wave reflection, transmission and AVO effects are given in Appendix A.

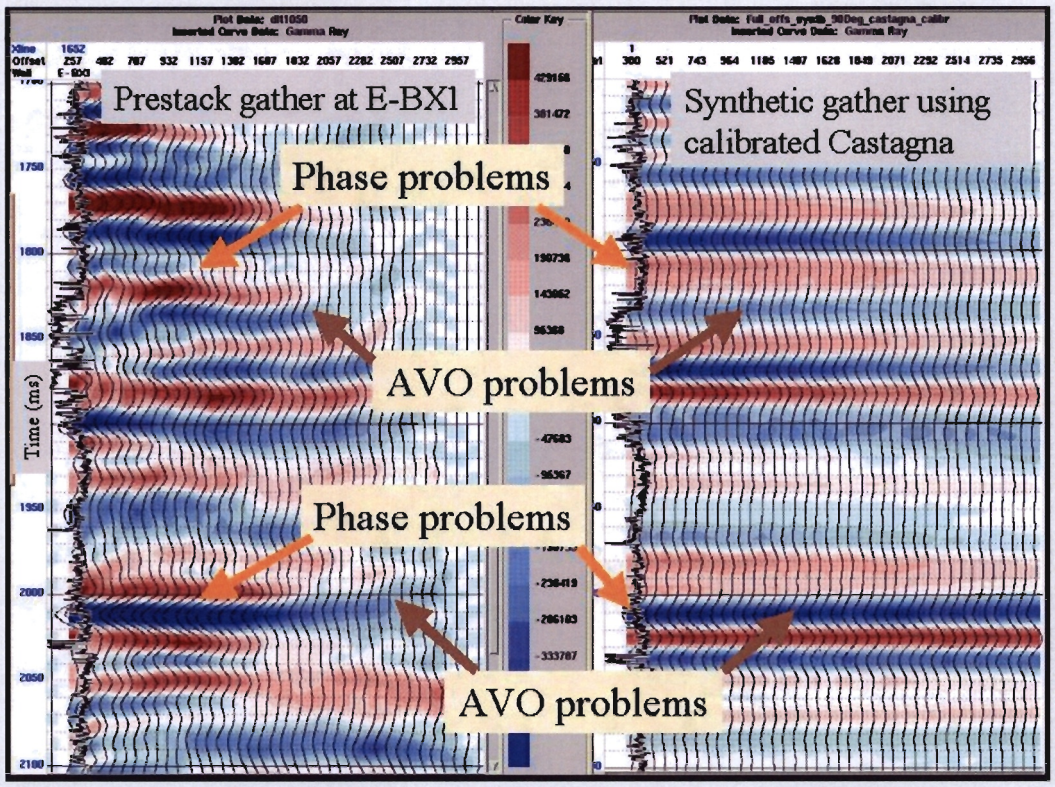

Figure 25. Comparison of a prestack seismic gather at E-BX1 (left) and synthetic pre-stack gather generated using the central Bredasdorp Basin calibrated Castagna Vp-Vs relationship

Figure 25 shows a comparison between the full offset synthetic calculated with the Zoeppritz equations and the Central Bredasdorp Basin calibrated Castagna Vp-Vs relationship, and the pre-stack seismic gather, closest to the E-BX1 well. The synthetic gather was converted from an angle gather to an offset gather using a smoothed E-BX1 sonic log. The real seismic gather has a mute zone, which increasingly reduces the offset from about 1950ms up. This mute was not applied to the synthetic gather. The GR log is plotted on the left to indicate the position of the upper and lower 13B sandstone units. Upon closer inspection it is noted that both phase and amplitude discrepancies exist. For example, the reflection from the top of the upper sand is associated with a trough (blue) on the synthetic gather, whereas it is associated with a peak (red) in the real seismic data. This event also shows a larger AVO effect on the synthetic than in the real data. Since the well

calibration is the critical link between the log and the seismic data, and since it is through this link that classification of the seismic data will occur, it is of utmost importance that the best possible well tie is achieved. For this reason, the Vp-Vs relationship was re-evaluated.

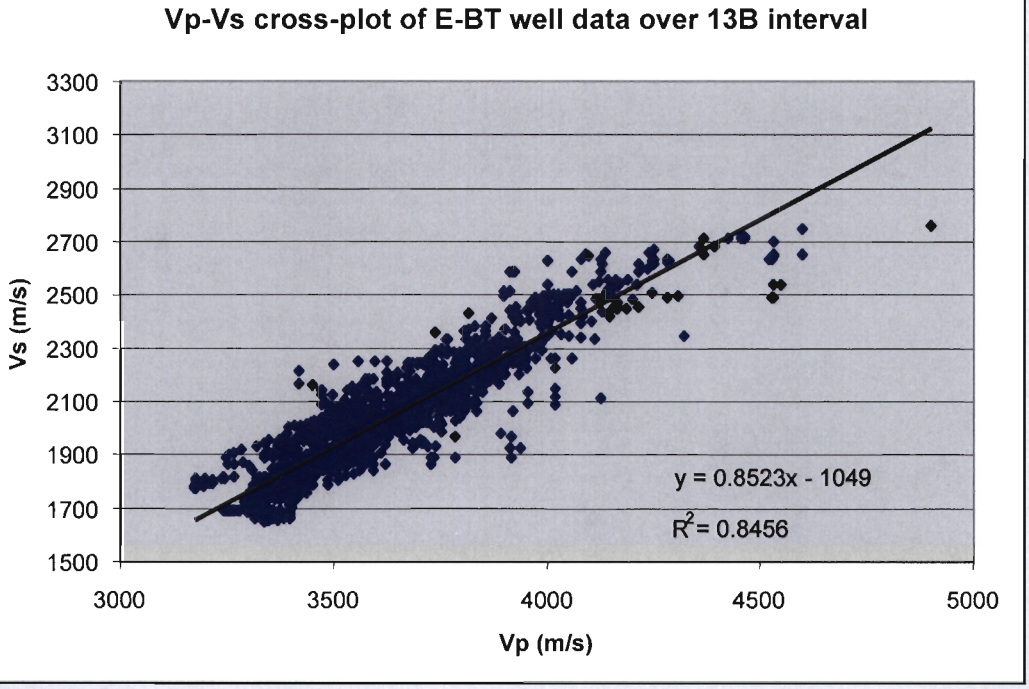

Figure 26. Locally calibrated Castagna Vp-Vs relationship .

Locally calibrated 13B Castagna relationship

The full offset synthetic seismic tie indicated some AVO misties (previous section). These may originate from errors in the sandstone Vp Vs relationship, which was used to calculate the synthetic. A better tie may be obtained by calibrating the Vp-Vs relationship using only sonic log data recorded over the 13B interval. Boreholes E-BT1 and E-BT3 (Figure 22) recorded Vp and Vs logs over the 13B interval. E-BT1 encountered 40m of water wet 13B sandstone, and E-BT3 encountered 35m of water wet 13B sandstone. Figure 26 shows a cross-plot of Vs and Vp. From this, the locally calibrated Castagna relationship has been established as:

$$Vs = 0.852Vp - 1.049 \quad \text{(km/s)} \quad (11)$$

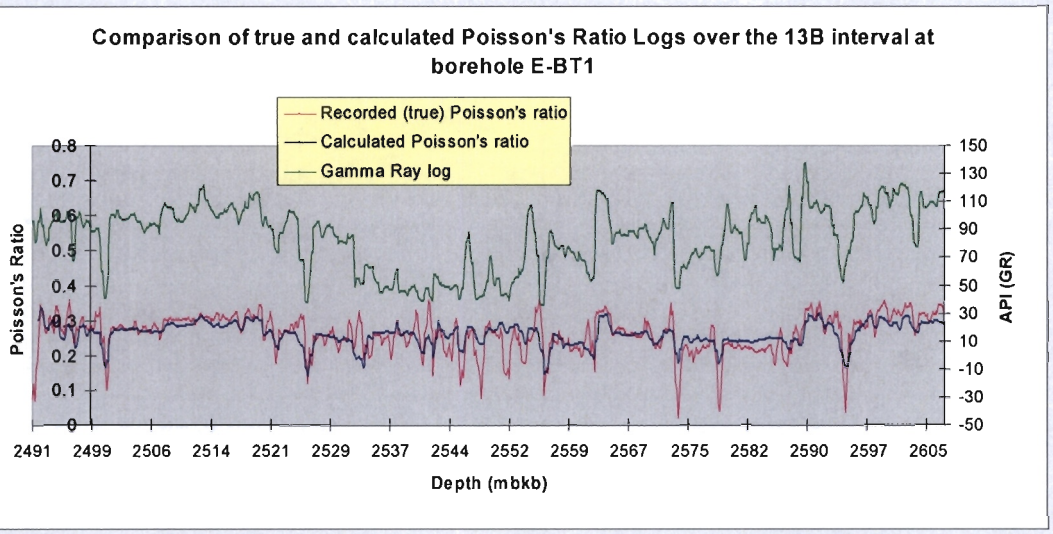

Figure 27. Comparison of the recorded and calculated Poisson's ratio log over the 13B sandstone interval at borehole E-BT1.

This relationship is very close to the original mudrock line of Castagna et al. (1985), which implies that the 13B sandstone around E-BX1 has very similar Vp and Vs values to those from the Gulf of Mexico used by Castagna et al. in 1985. From this relationship, a Poisson's ratio log was calculated for E-BT1, and compared to the actual Poisson's ratio log in borehole E-BT1. Figure 27 shows a comparison between the two logs. Another full offset synthetic was calculated for E-BX-1, using the Zoeppritz equations, this time with the local 13B Castagna relationship. The full offset synthetic seismogram, and an actual pre-stack seismic gather are shown in Figure 28. A slightly improved pre-stack tie is achieved using this relationship, which gives confidence in the Vp-Vs relationship. Remaining differences between the synthetic and the gather can be mainly attributed to seismic and logging noise.

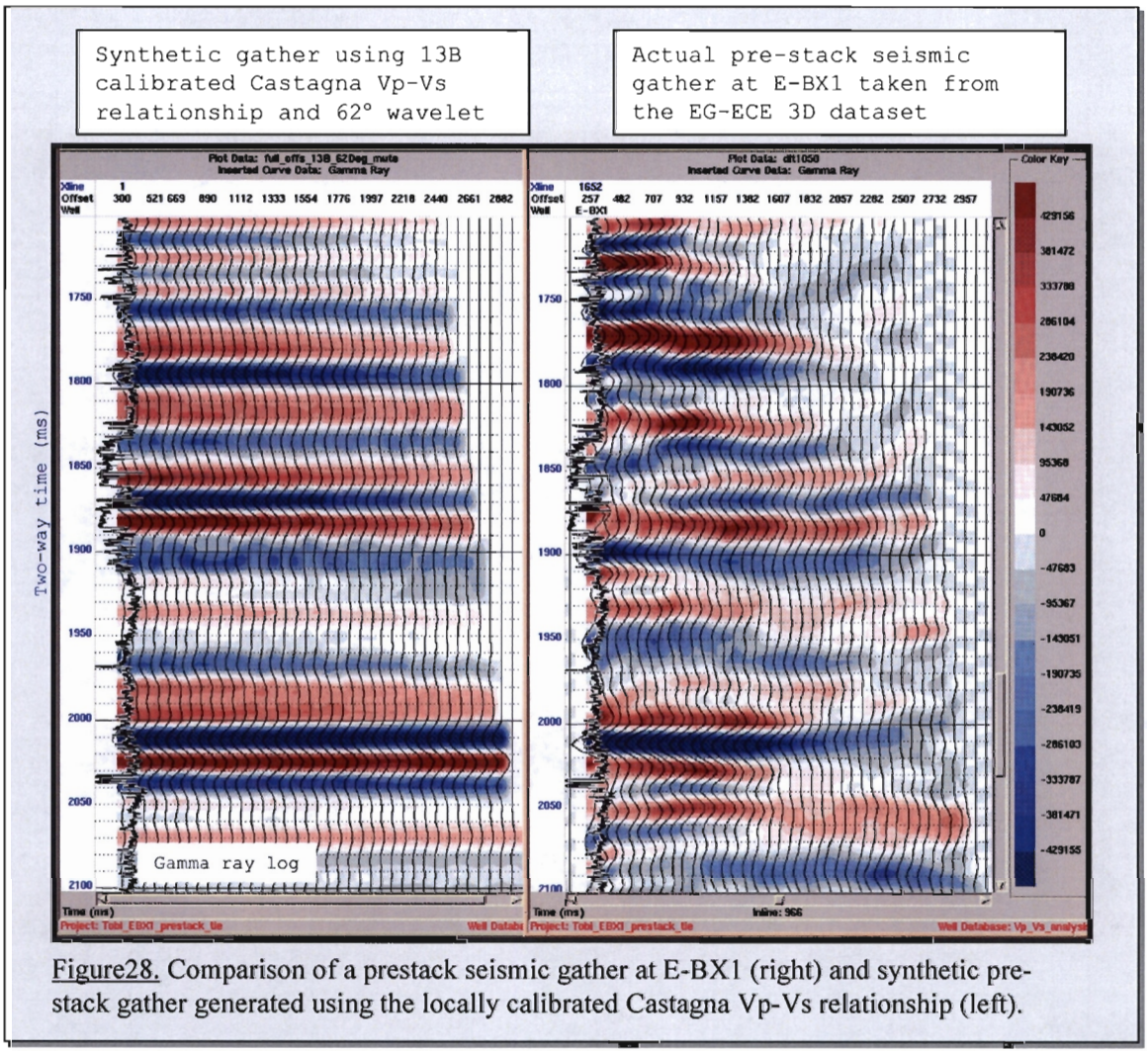

Figure28. Comparison of a prestack seismic gather at E-BX1 (right) and synthetic pre-stack gather generated using the locally calibrated Castagna Vp-Vs relationship (left).

4.7 Tuning analysis

A full offset tuning analysis was conducted in order to investigate the seismic response of thinning the sand units encountered at borehole E-BX1. The tuning analysis was also performed to evaluate the high amplitude response of the northern anomaly (section 4.4). A number of 2D wedge models were generated by varying the thickness of the upper and the lower 13B sandstone, and also of the intervening shale. The thickness of each unit was varied from 0 to 100m in the various models. The Zoeppritz equations were then used to calculate 21 full offset synthetic seismograms for each model (5m spacing from 0 to 100m). Each full offset synthetic seismogram was then

stacked, and plotted on the model. The reason for generating full offset wedge models, rather than to assume normal incidence, is to account for amplitude variations resulting from AVO effects. The seismic wavelet from the well tie (section 4.5), the recorded Vp, and the calculated Vs logs (section 4.6) were used to generate the full offset synthetics. The seismic response of these wedge models was then compared to real seismic sections. Not all the models can be shown here, but the best synthetic – seismic match along a dip line through E-BX1 was obtained where the upper sand and the intervening interbedded shale thins out. A comparison between this model and a seismic inline through E-BX1 is shown in Figure 29.

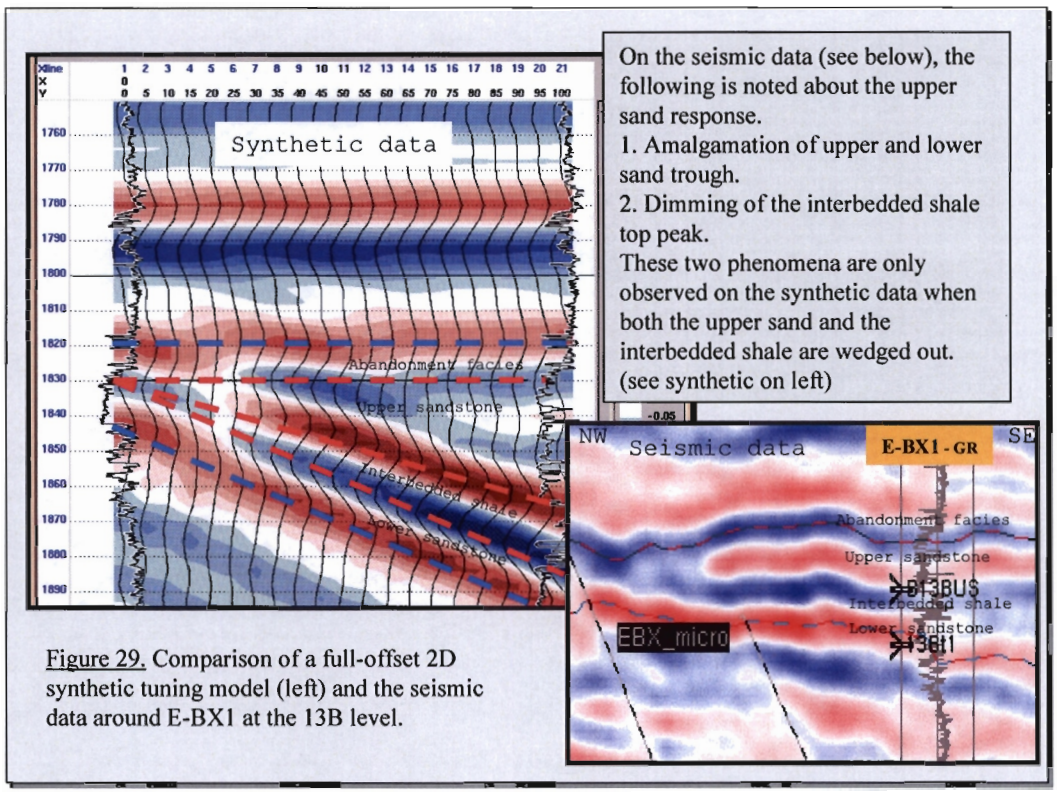

Figure 29. Comparison of a full-offset 2D synthetic tuning model (left) and the seismic data around E-BX1 at the 13B level.

This model is in agreement with the channelised depositional system envisaged for the upper sandstone. Assuming this model is true, then the increased amplitude observed in the real seismic in Figure 29, can be attributed to tuning. This can be used to determine if the northern amplitude anomaly may be associated with the upper sandstone thinning, and thus tuning. Figure 30 shows an amplitude extraction along the upper sandstone from E-BX1 to the northern anomaly. The amplitude of the northern anomaly

is roughly double that caused by tuning. The comparison suggests that the high amplitudes of the northern anomaly cannot be attributed to tuning effects alone. Other factors such as an increase in porosity, change in fluid-fill or a change in lithology are factors that could explain the high amplitudes in the seismic data.

The tuning analysis suggested that a more detailed approach, such as an inversion, is necessary to identify the cause of the anomaly.

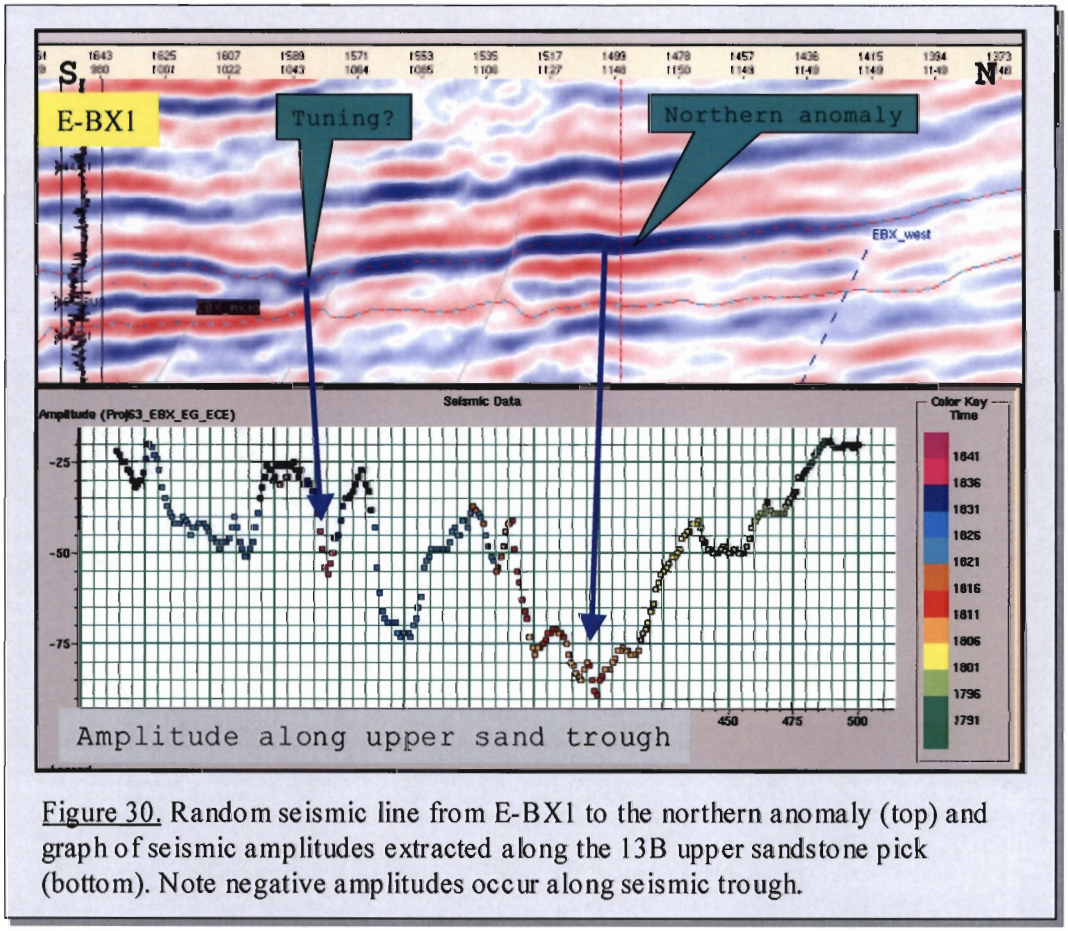

Figure 30. Random seismic line from E-BX1 to the northern anomaly (top) and graph of seismic amplitudes extracted along the 13B upper sandstone pick (bottom). Note negative amplitudes occur along seismic trough.

5 Seismic attributes and training data

In this chapter, the use of seismic attributes, the method of extracting them from seismic data, and the classification into lithology and fluid categories will be discussed. Seismic attributes have been used for many years, to help interpreters highlight geological features in seismic data. The link between seismic attributes and geological parameters is rock physics. Calculating rock parameters from seismic attributes is plagued by non-uniqueness (i.e. many geological "states" give the same attribute value), and seismic noise. It is for this reason that mineralogy, porosity, pressure or fluid saturation are difficult parameters to quantify from seismic data. Often these parameters are inferred from the geological knowledge, rather than from the seismic data. The statistical rock physics workflow presented here can overcome this limitation by extracting as much quantitative geological information from the data as statistically possible.

For the purpose of this study, the geological information that is being sought, is the presence and distribution of hydrocarbon bearing 13B sandstone, updip of borehole E-BX1. It should be noted that the workflow presented here is not limited to this output, and depending on the data quality and well control points, any geological parameter, which affects wave propagation, could be considered.

5.1 Seismic attributes

Conventional seismic data record the time and amplitude of subsurface P-wave reflections, which depend mainly on the variations of Vp, Vs and density of the subsurface. These properties are usually grouped into P-impedance (I_P) and S-impedance (I_S), which are the product of Vp and density and Vs and density respectively. Since S-waves only travel in solids, offshore data

mainly record reflections associated with P-waves. For this reason, seismic attributes associated with P-wave impedance (I_p) are generally of highest quality. When used alone, I_p attributes make poor fluid-, and sometimes also poor lithology discriminators. An additional measurement, such as S-impedance (I_s) attributes usually improves the discriminating ability greatly. Unfortunately I_s attributes are more noisy that I_p attributes. This is because information about the Vs of subsurface layers is hidden in the AVO behavior of conventional seismic data. AVO attributes are typically extracted pre-stack, which implies they do not benefit as much from the noise reduction which stacking adds to I_p attributes. Many ways of extracting the shear impedance information from conventional seismic data exist. One way, for example is to calculate an intercept and a gradient for events on pre-stack gathers. Another way is to invert the seismic gathers (pre-stack inversion), and use elastic impedance to determine the I_s. Once the shear information has been extracted, it can be used "as is", or transformed into new attributes, such as fluid factor, or LMR attributes (next section). This is usually done to create an optimal set of attributes for lithology and fluid classification.

5.1.1 LMR attributes

LMR attributes refer to the elasticity parameters λ (lambda) and μ (mu), and the density ρ (rho). The elasticity parameters λ and μ are also called Lamé's parameters, after the famous French mathematician Gabriel Lamé. He contributed substantially to elasticity theory by studying the stability of vaults, and the design of suspension bridges (O'Connor and Robertson, 2004). μ is the rigidity or shear modulus of a material, measuring how well that material resists shear strain. Fluids do not resist shear strain since they can flow into any shape, and thus have a μ of zero. Although λ has no obvious physical meaning, it is a parameter that is related to the bulk modulus (K) or incompressibility and μ of a material through the following equation;

$$\lambda = K - \frac{2}{3}\mu \qquad (12)$$

Goodway suggests that LMR attributes (generated by pre-stack inversion) are better lithology and fluid discriminators than other AVO attributes (Goodway et al., 1997). Smith has rewritten the 2-term Fatti et al. reflectivity equation in terms of $\lambda\rho$ and $\mu\rho$ as follows (Smith, 1999; Fatti et al., 1994);

$$4(\lambda\rho + 2\mu\rho)R(\theta) = \Delta(\lambda\rho)(1+\tan^2\theta) + 2\Delta(\mu\rho)(1+\tan^2\theta - 4\sin^2\theta) \qquad (13)$$

R - reflectivity

θ - angle of incidence

The original 1987 Smith and Gidlow two-term reflectivity equation is given in Appendix A.

Equation 10 allows extraction of the differences, $\Delta(\lambda\rho)$ and $\Delta(\mu\rho)$, directly from scaled seismic data, and represents a simple alternative to extracting the parameters through pre-stack inversion. Smith also demonstrates that the fluid factor and the $\Delta(\lambda\rho)$ parameter plot very close on an intercept-gradient cross-plot (Smith, 1999). In this study, $\lambda\rho$ and $\mu\rho$ attributes from seismic inversions will be used for the classification.

λ and μ cannot be extracted from seismic data separately from ρ, except by solving the AVO curves for higher-order terms. Usually $\lambda\rho$ and $\mu\rho$ are used instead. They are related to Vp and Vs through the following equations:

$Vs = \sqrt{\frac{\mu}{\rho}}$ which can be rewritten in terms of I_s as:

$$\mu\rho = (I_s)^2 \qquad (14)$$

and

$$Vp = \sqrt{\frac{\lambda + 2\mu}{\rho}}$$ which can be rewritten in terms of I_p and I_s as:

$$\lambda\rho = (I_p)^2 - 2(I_s)^2 \qquad (15)$$

$\mu\rho$ only depends on the I_s, whereas $\lambda\rho$ depends on both I_p and I_s. Since hydrocarbons are less dense and more compressible than brine, hydrocarbon saturated sandstone has a lower $\lambda\rho$ than brine-saturated sandstone. $\lambda\rho$ is thus used as a fluid discriminator. $\mu\rho$ on the other hand can be used as a lithology discriminator, since shear strength and density vary largely with lithology. Furthermore, $\mu\rho$ is not affected much by pore-filling fluids, since fluids have no rigidity, and thus μ is zero for any fluid.

Unfortunately $\lambda\rho$ and $\mu\rho$ are not only affected by variations in lithology and pore-fluid fill. Temperature, pressure, porosity and clay content also affect the incompressibility and rigidity of rocks, and variations in these need to be considered when using these attributes for seismic interpretation.

5.1.2 LMR attributes from seismic data

LMR attributes are calculated from I_p and I_s. The acoustic impedance of a rock is the product of velocity and density. It is a *layer property*, since it only depends on the density and velocity of that layer. Seismic reflections are not layer properties, since they depend on the difference in acoustic impedances between layers. These are called *boundary properties.* In order to extract layer impedance from seismic data, the data are inverted. Seismic inversion is non-unique. It is generally performed through iterative numerical algorithms, which attempt to minimize the error between a model and the actual seismic data. Many different inversion algorithms exist, and it is not within the scope of this study to discuss their details. Most inversions require a starting model, and a seismic wavelet. Usually the user can also define a

maximum tolerated deviation from the starting model. This tolerance allows the geological knowledge to be incorporated. In areas where many boreholes have been drilled, and the spatial variation (variogram) of the impedance can be evaluated for each layer, a geostatistical inversion can be performed. This ensures that the observed variability from the boreholes is preserved. Provided the correct variability can be determined from well-data, Dubrule suggests that geostatistical inversions give better results that normal, trace by trace (1D) inversions (Dubrule, 2003). Owing to insufficient well control, only trace-by-trace inversions were performed for this study. The implication of this is that the results may have a higher degree of variability than is geologically expected. This is as a result of noise in the seismic data, and causes attribute maps to also appear noisy.

Two inversion methods were performed in this study, namely post-stack inversion, and pre-stack inversion.

5.1.3 LMR attributes from post-stack inversion

The workflow to determine LMR attributes from post-stack inversion is shown in Figure 31. The calculation of P- and S-reflectivity cubes, and the post-stack inversions were done with the Hampson and Russell software. The term "post-stack" is not being applied here completely accurately, since the P- and S-reflectivity cubes are in fact generated from the pre-stack seismic data, using a least-squares weighting procedure based on the Fatti et al. (1994) equation (see Appendix A).

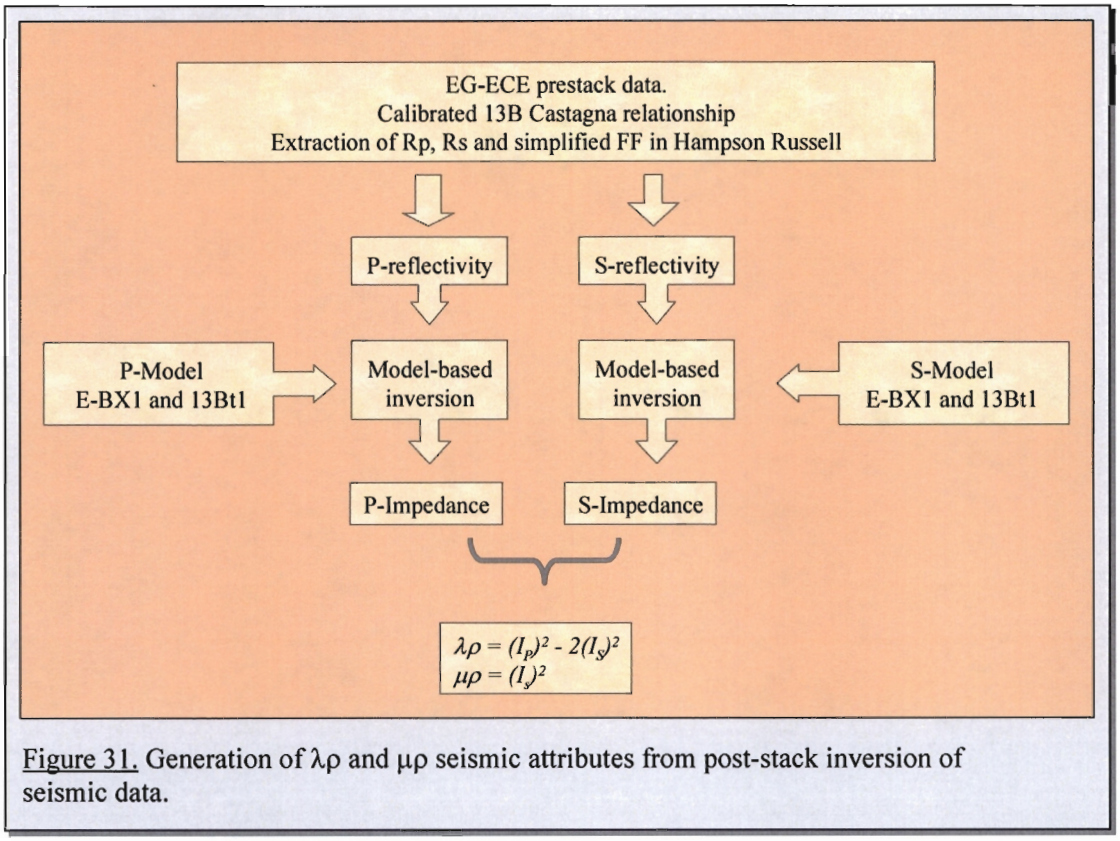

Figure 31. Generation of λρ and μρ seismic attributes from post-stack inversion of seismic data.

The first step of the workflow is to generate P- and S-wave reflectivity cubes. Since S-wave data are not recorded, it needs to be calculated from the P-wave data. It has been mentioned before that information about the Vp and Vs of subsurface layers is encoded in the amplitude variation with offset on pre-stack seismic data. In order to extract this information, intercept and gradient volumes are calculated from the pre-stack data. These are then used, together with the locally calibrated 13B Castagna Vp-Vs relationship (section 4.6), to calculate P- and S-wave reflectivity cubes. Figure 32 shows how the intercept and gradient were calculated from the pre-stack data at E-BX1. The next step involves inverting the P- and S-reflectivity cubes to I_p and I_s cubes. A model-based inversion was performed in Hampson and Russell's *Strata* software package. As an input model, the up-scaled I_p and I_s calculated from the E-BX1 logs was used (section 5.2). E-BX1's impedance profile was projected along the 13Bt1 horizon, to ensure an accurate starting model. The seismic wavelet from the post-stack well tie was used for both inversions (section 4.5).

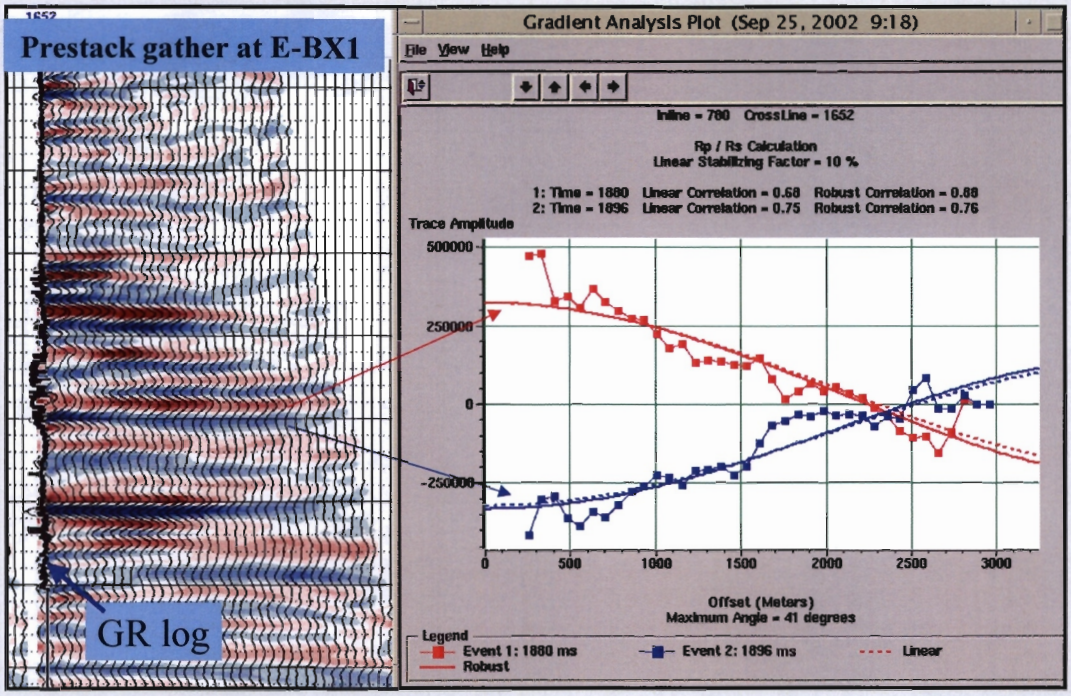

Figure 32. Extraction of the intercept and gradient from pre-stack seismic data.

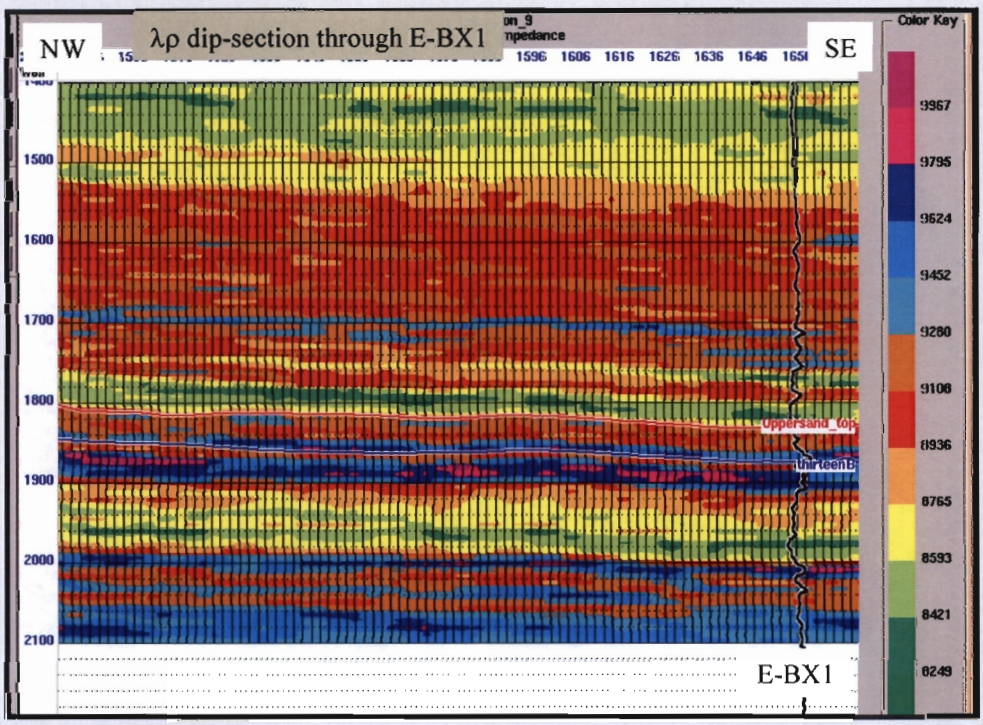

Figure 33. Post-stack inversion λρ dip section through E-BX1.

The final step of generating post-stack $\lambda\rho$ and $\mu\rho$ attribute cubes is to calculate them from the I_p and I_s volumes, as outlined in Figure 31. Figures 33 and 34 show the results of the two inversions along a section through E-BX1. The up-scaled $\lambda\rho$ or $\mu\rho$ log is shown at the well location on both figures. The inversion and the up-scaled logs show a good correlation. The $\lambda\rho$ and $\mu\rho$ response along the upper 13B sandstone is shown in Figures 35 and 36. These results will be discussed in more detail in chapter 6.

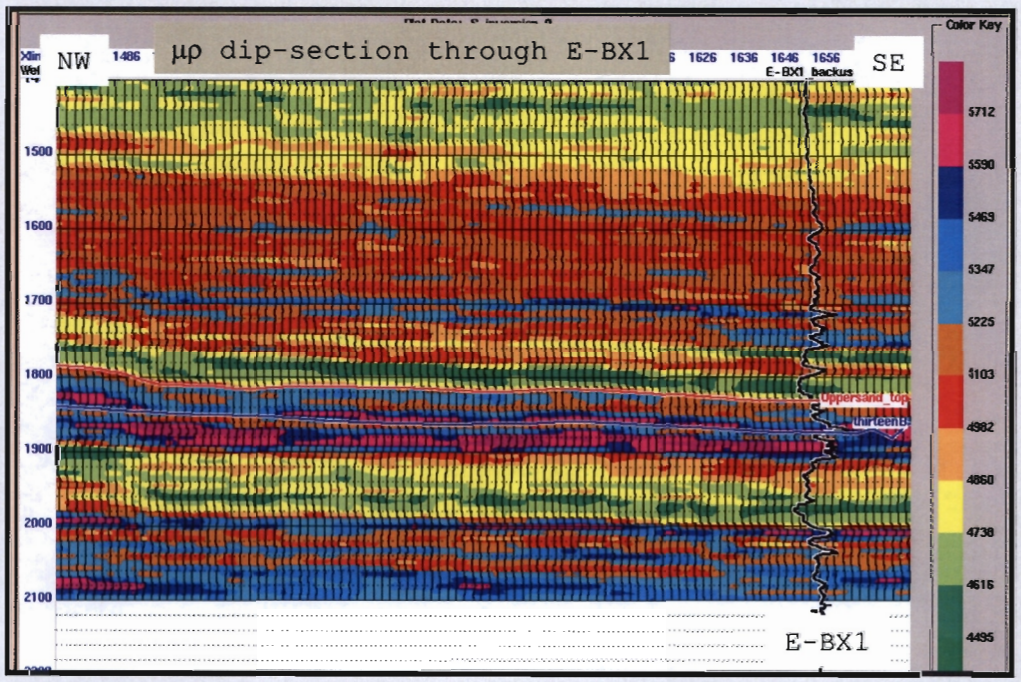

Figure 34. Post-stack inversion μρ dip section through E-BX1.

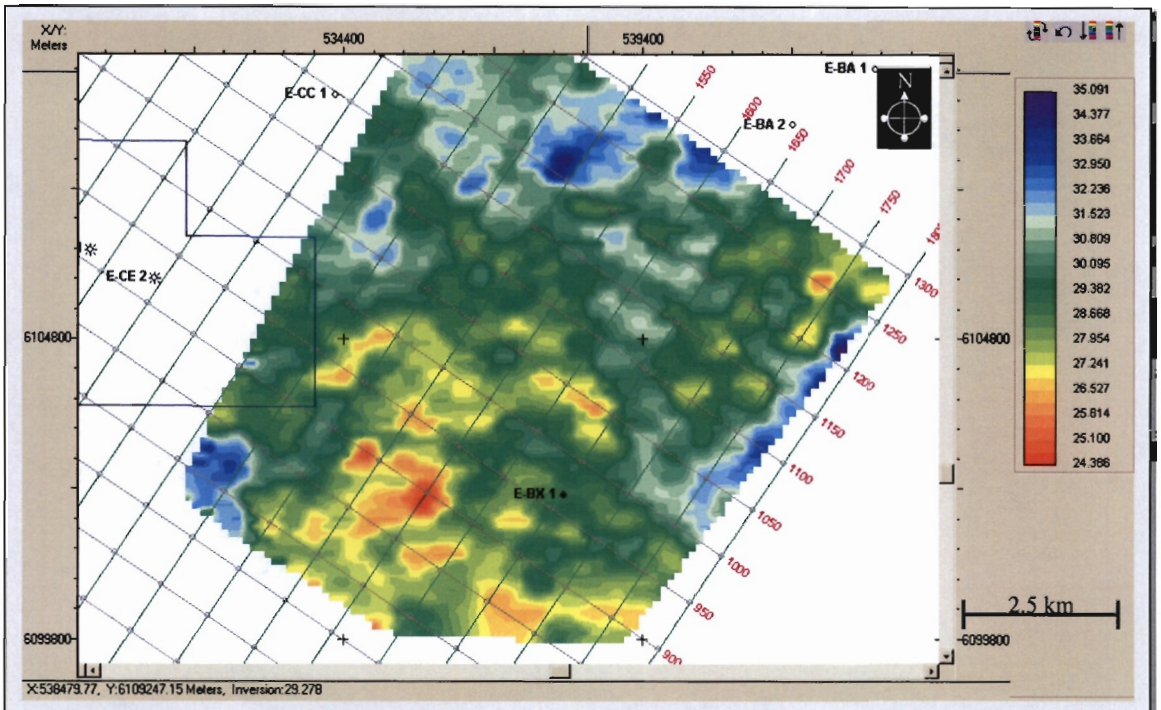

Figure 35. Post-stack inversion λρ map at 13B level.

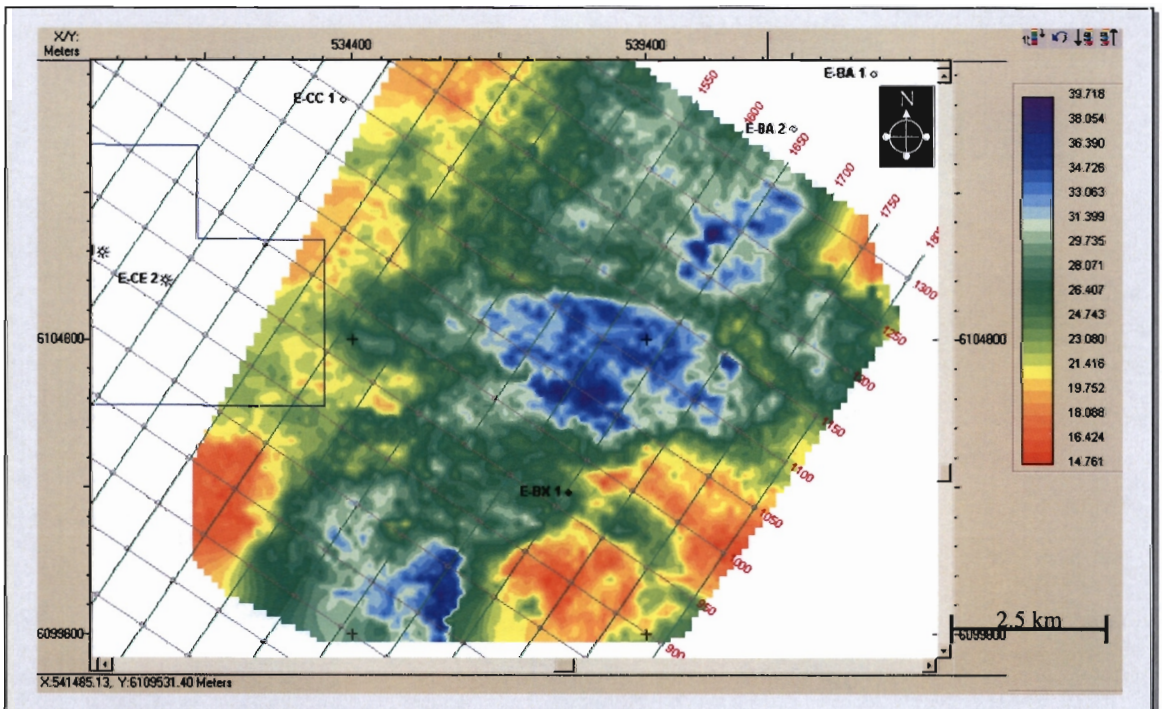

Figure 36. Post-stack inversion μρ map at 13B level.

There are various ways to determine the accuracy of a seismic inversion. A general rule is that the better the seismic data, the better the inversion. Also, the more wells to define the starting model, the better the inversion. If many wells are available as control points for an inversion, then a good inversion accuracy test is to systematically leave out wells from the starting model, and compare the "blind" inversion result with the well result. This technique is sometimes called the *"leave-one-out jackknife"* technique. Since this inversion was done with only one well, it its impossible to perform this test. The best alternative is to calculate synthetic $\lambda\rho$ and $\mu\rho$ attributes from the log data, and compare them to the seismically derived attributes at the well location. This comparison is shown in Figures 37 and 38. Generally there is a good correlation between the model, and the inverted results for both $\lambda\rho$ and $\mu\rho$. Based on a visual comparison, the $\mu\rho$ trace from the inversion seems to show a slightly better correlation to the model trace than $\lambda\rho$.

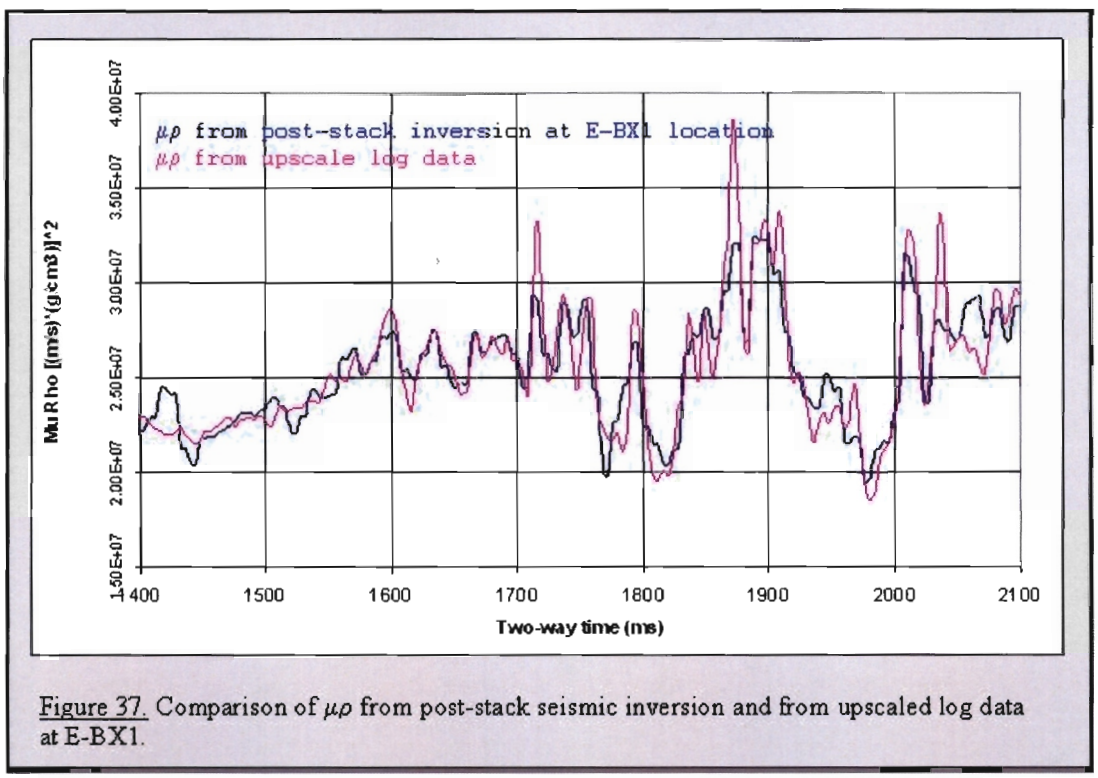

Figure 37. Comparison of $\mu\rho$ from post-stack seismic inversion and from upscaled log data at E-BX1.

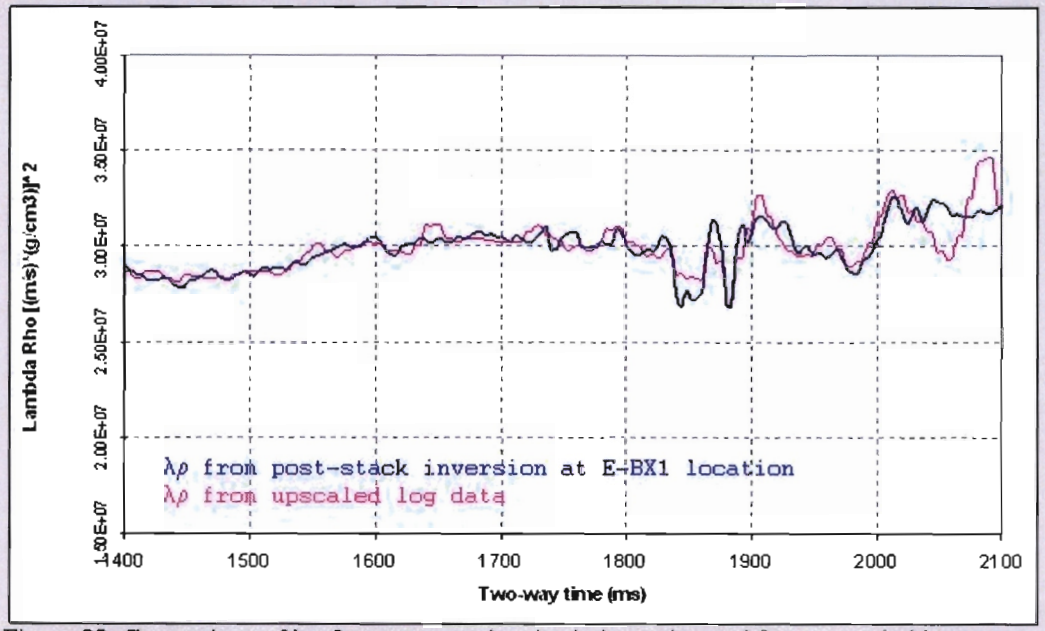

Figure 38. Comparison of $\lambda\rho$ from post-stack seismic inversion and from upscaled log data at E-BX1.

Of course the long wavelength trends in the seismic inversion in figures 37, 38, 47 and 48 com from the model rather than from the seismic data. Although the seismic inversion does not accurately reproduce the shortest wavelength details of the model, it is possible that the good correlation observed, especially for the $\mu\rho$ inversions, is partly a result of the influence of the model on the seismic inversion at frequencies above the seismic frequency band as well.

5.1.4 LMR attributes from pre-stack inversion

Generating fluid and lithology attributes from pre-stack seismic inversions is more difficult than the post-stack route. This is primarily because performing pre-stack inversions is more difficult than post-stack inversions. Pre-stack seismic data have the added dimension of offset (or angle), which is diminished during stacking. Pre-stack inversion involves inverting each offset, at each trace location separately. To simplify the process, the pre-stack data can be partially stacked. This is called *range-limited* stacking, and occurs

over a pre-defined offset or angle interval. Each range-limited stack is then inverted in the same way post-stack inversions are done. One difference is that the starting model for each "range" needs to be determined. For post-stack inversions, the starting model is simply the up-scaled acoustic impedance, calculated from well logs. For non-zero offset data the elastic impedance (I_e) is used as a starting model. Elastic impedance is similar to the acoustic impedance calculated at non-zero incidence angles (Mavko et al., 1998). I_e is related to seismic reflectivity through the following relationship:

$$I_e = e^{2\int R(\theta).dt} \qquad (16)$$

R(θ) is the reflectivity at angle *θ*.

The formula contains an integral, since impedance is a layer property, whereas reflectivity is a boundary property.

R(θ) can be calculated with the Zoeppritz equations (Zoeppritz, 1919), or any of the well-known approximations, such as Aki and Richards (Aki and Richards, 1980). In order to use an elastic impedance equation for seismic attribute extraction, further simplification is required. This is because Vp, Vs and ρ cannot be extracted separately from conventional seismic data. Connolly proposed, amongst others, the following equation for elastic impedance (Connolly, 1998);

$$I_e(\theta) = Vp^{(1+\tan^2\theta)} * Vs^{(-8K\sin^2\theta)} * \rho^{(1-4K\sin^2\theta)} \qquad (17)$$

Where

Ie(θ) Elastic impedance at angle *θ*

K Vs^2 / Vp^2

Elastic impedance is the imaginary acoustic impedance that would give rise to the zero offset reflectivity equivalent to the actual affoset reflectivity modeled using the Aki-Richards equation. It is not the same as the acoustic

impedance, but reduces the acoustic impedance at θ=0 degrees. Mathematically, the Aki –Richards equation is obtained by taking the natural logarithm, and then differentiating Connolly's elastic impedance equation.,

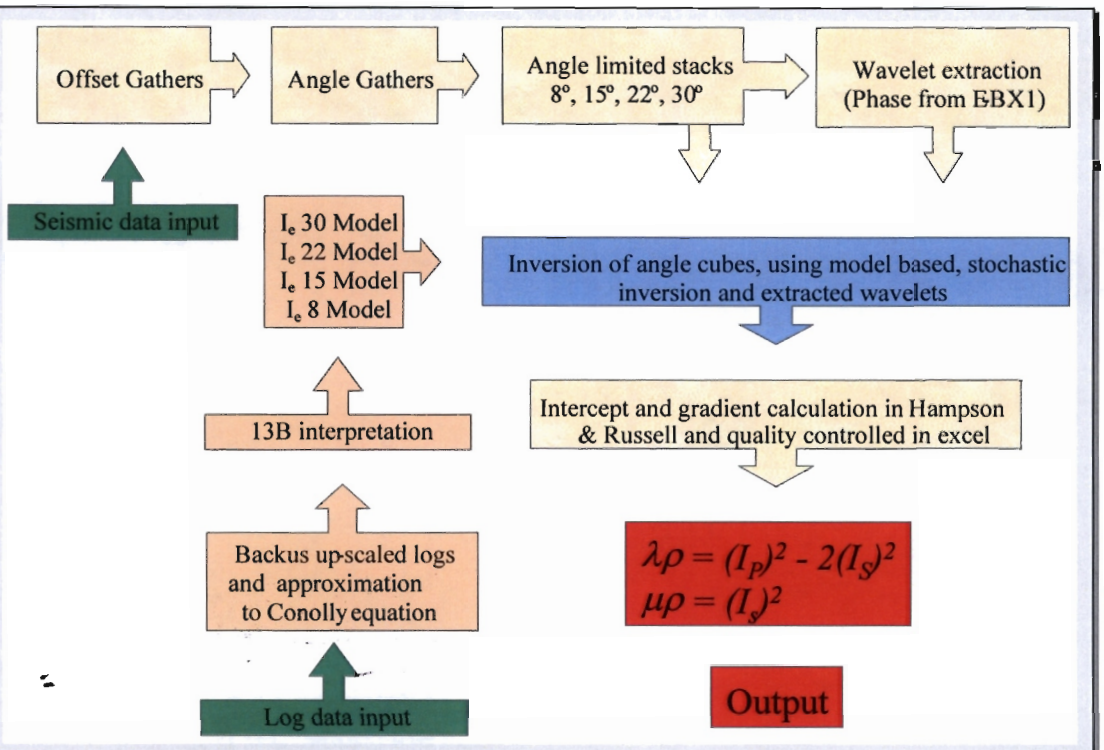

Figure 39. Workflow for generating pre-stack seismic $\lambda\mu\rho$ attributes.

The workflow for extracting LMR attributes from pre-stack inversion is shown in Figure 39. The workflow starts with converting the pre-stack seismic data from the offset domain to the angle domain. This was done using a 500ms smoothed sonic log from E-BX1. In the next step, the pre-stack seismic data were divided into four angle-limited ranges, namely

- 4° –12 ° (average 8 °)
- 12 ° – 18 ° (average 15 °)
- 18 ° – 26 ° (average 22 °)
- 26 ° – 34 ° (average 30 °)

These ranges were subsequently stacked into four range-limited stack at 8°, 15 °, 22 ° and 30 °, as shown in Figure 40. The amplitude spectrum of seismic data narrows with offset. This is as a result of the longer ray paths that far offset waves travel compounded by the effect of narrowing reflection hyperbolae, which implies that the seismic wavelet changes with angle. Since

the wavelet is required as an input for the pre-stack inversion, it can be extracted separately for each range-limited stack. Figure 41 and 42 shows the zero-phase wavelet, and amplitude spectra of the range-limited stacks. The loss of high frequencies at higher angles is clearly seen on these displays. Cambois suggests that inverting the range-limited stacks with different wavelets attenuates noise in the resulting attributes (Cambois, 2001). This is one of the main advantages of pre-stack inversion over post-stack inversion.

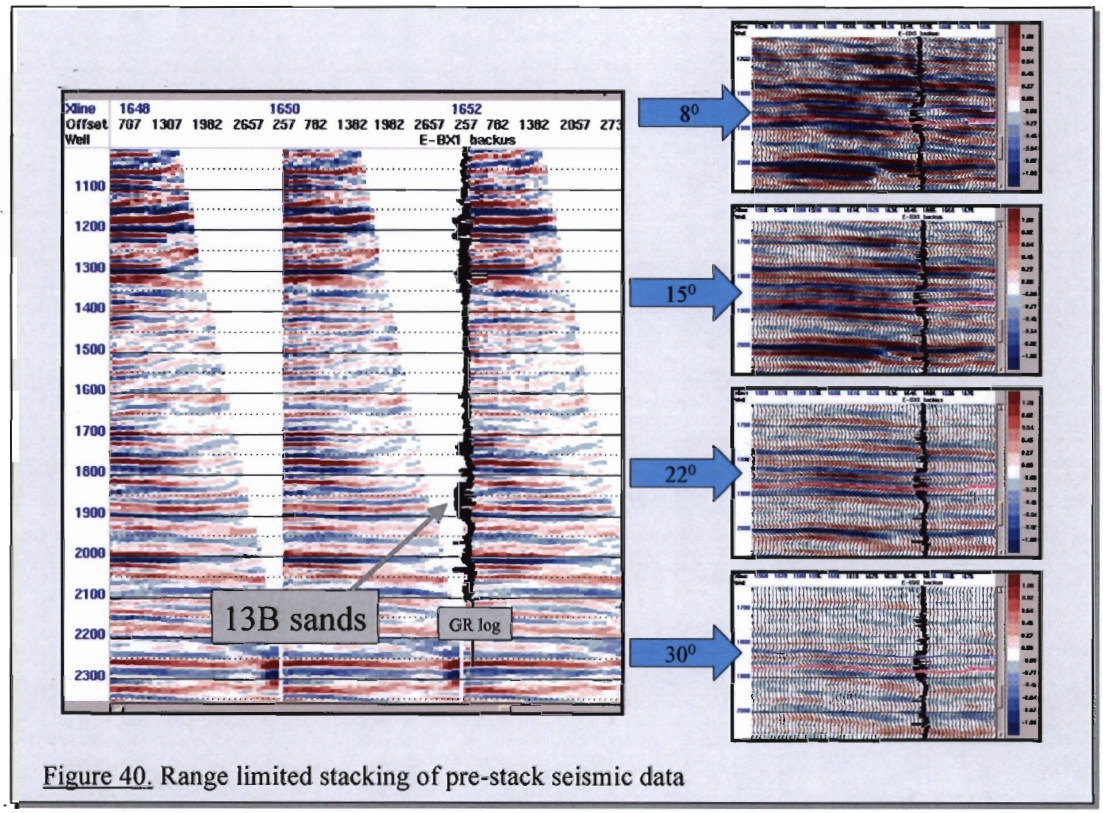

Figure 40. Range limited stacking of pre-stack seismic data

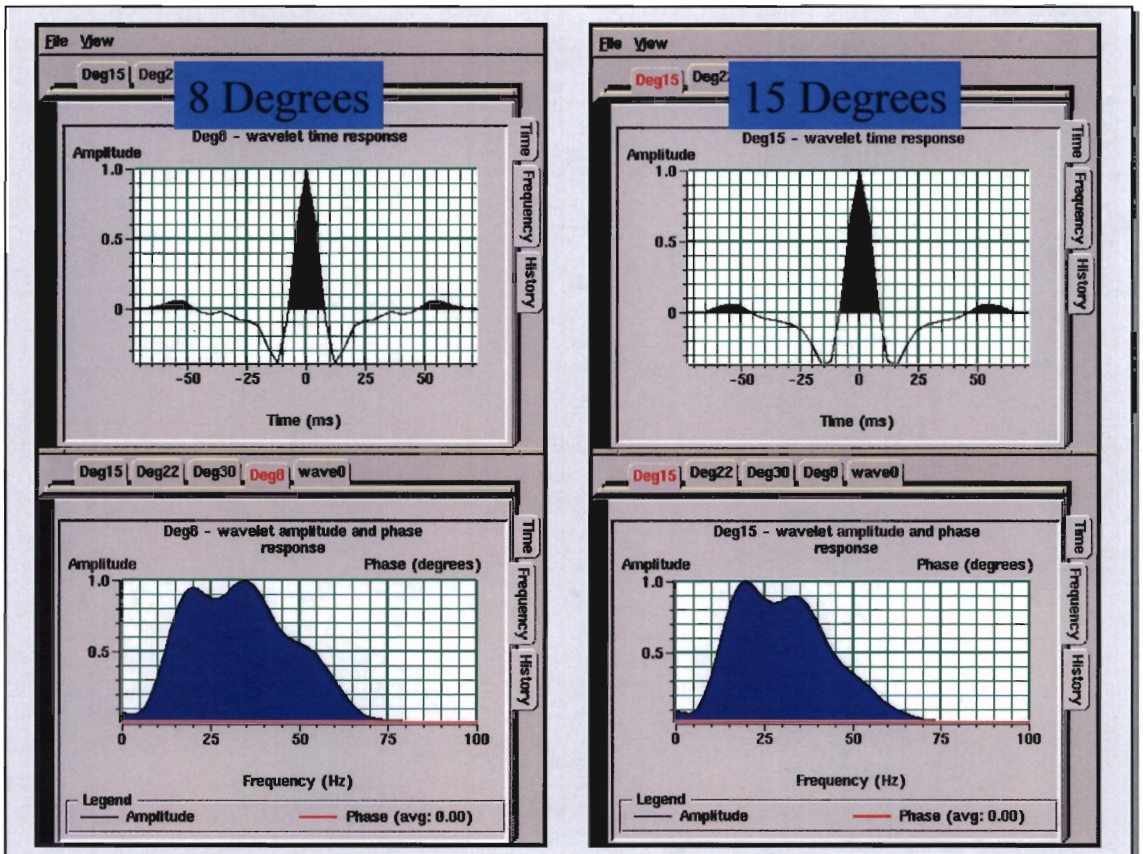

Figure 41. Zero-phase wavelet and amplitude spectrum of the range-limited stacks

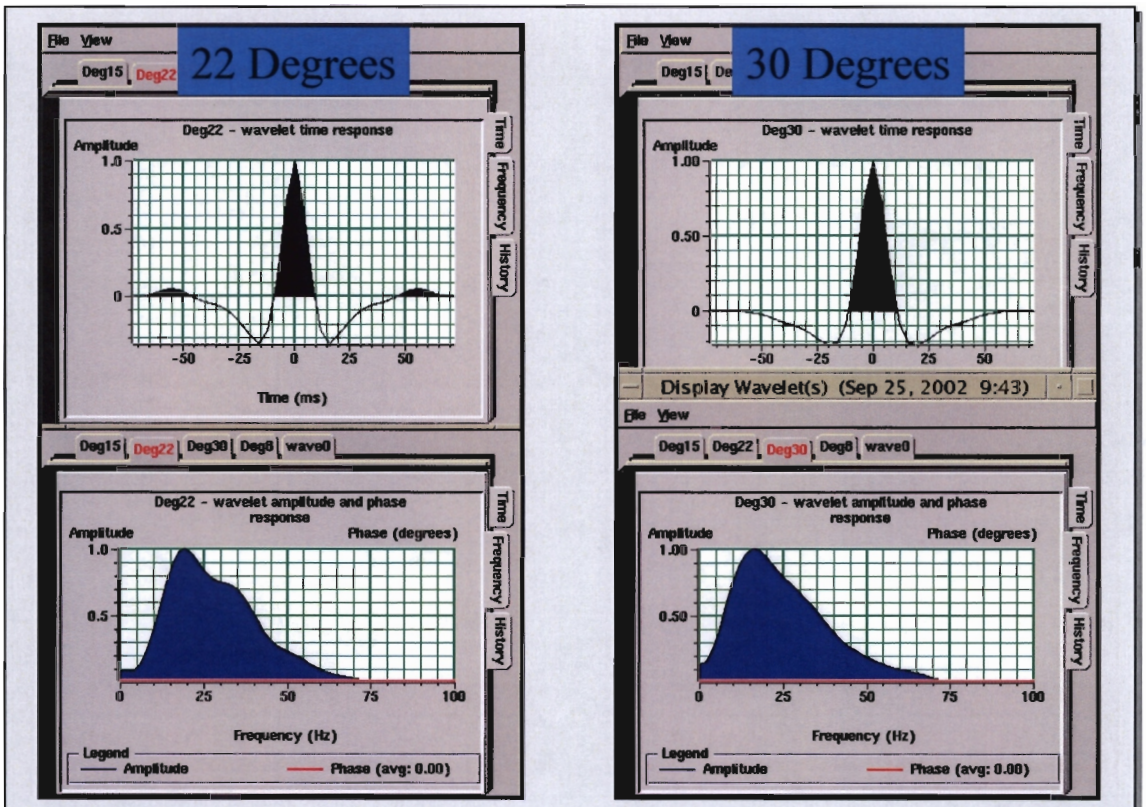

Figure 42. Zero-phase wavelet and amplitude spectrum of the range-limited stacks

The next step of the workflow involves generating the starting models for the inversion. This is done using the log data. Connolly's equation for elastic impedance, together with the Backus up-scaled (section 5.2) sonic and density logs of E-BX1 were used to generate elastic impedance logs for the four angles. Each of these was extrapolated along the interpretation of the 13Bt1 horizon for a 3D low frequency model, which was the starting model for the elastic impedance inversion. The extracted wavelets and the phase, together with the starting models, were then used to invert each range-limited stack. Figure 43 shows a section along E-BX1 of the four I_e cubes. The Backus up-scaled I_e log is plotted at the borehole location. The inversion was done using the Hampson & Russell "Strata" software package which offers a number of trace-by-trace 1D inversion algorithms. All the different inversion algorithms were tested on a single trace at borehole E-BX1. A model based inversion algorithm was chosen as yielding the best results, based on a comparison of the inverted trace and the up-scaled log data. This algorithm uses a starting model, the seismic data and a wavelet to find a lowest-error fit inversion to the seismic traces.

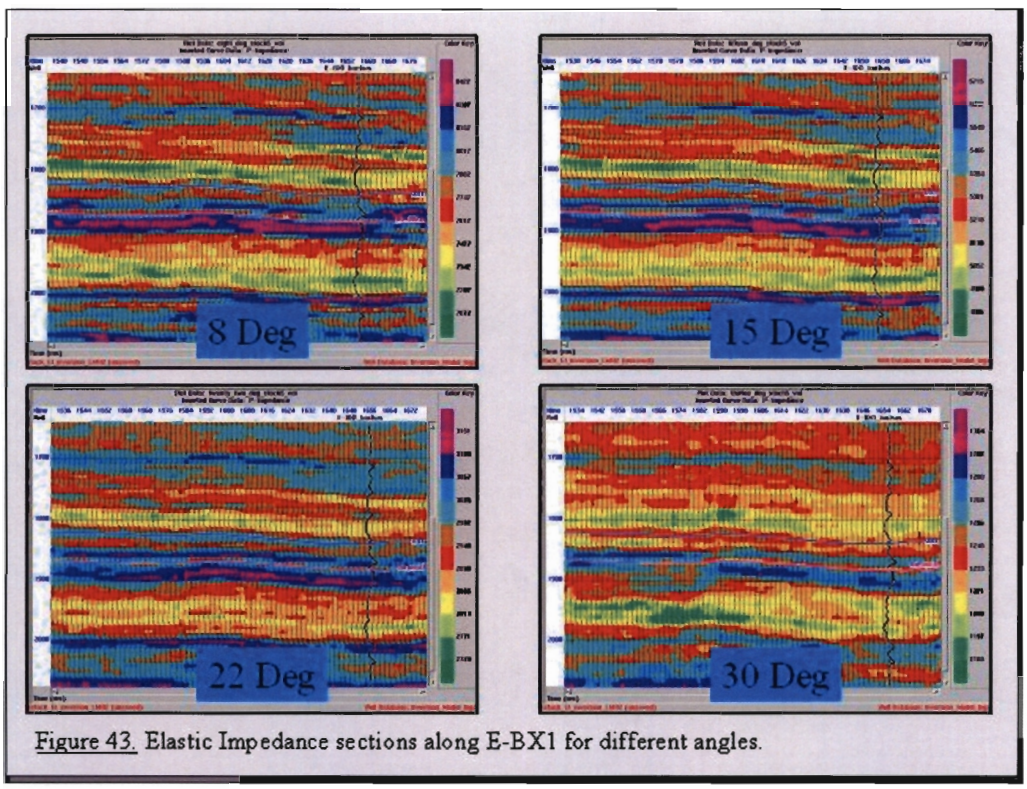

Figure 43. Elastic Impedance sections along E-BX1 for different angles.

The last step of the process involved extracting $\lambda\rho$ and $\mu\rho$ attributes from the I_e volumes. At each trace location, and at each 5ms time sample, the four I_e values were used to calculate an intercept and a gradient. These relate to the rate of change of I_e with angle. Connolly's I_e equation is then used to calculate I_p and I_s, which in turn are used to calculate $\lambda\rho$ and $\mu\rho$, as shown in Figure 39. It should be noted at this stage that four data points were used to extract an intercept and gradient, rather than just two. This was done because using four range-limited inversions better captures the wavelet variations in the pre-stack seismic data.

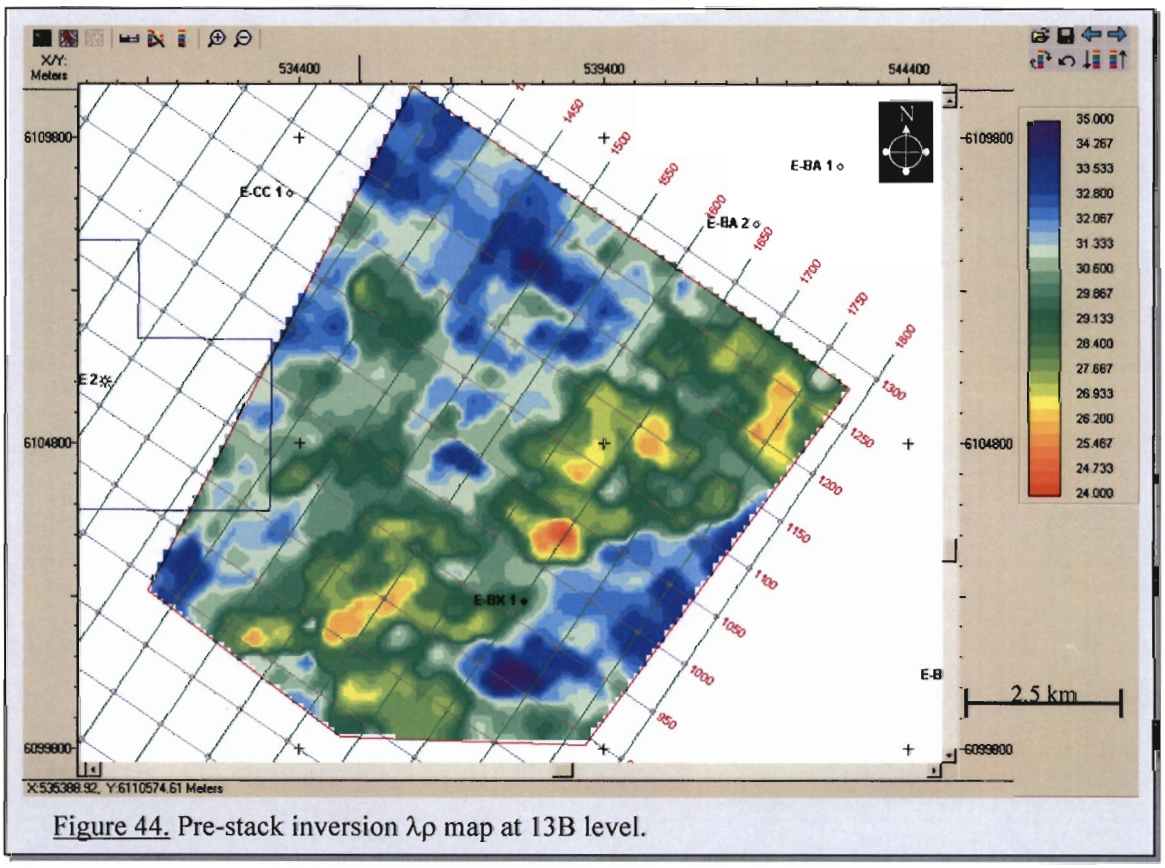

Figure 44. Pre-stack inversion $\lambda\rho$ map at 13B level.

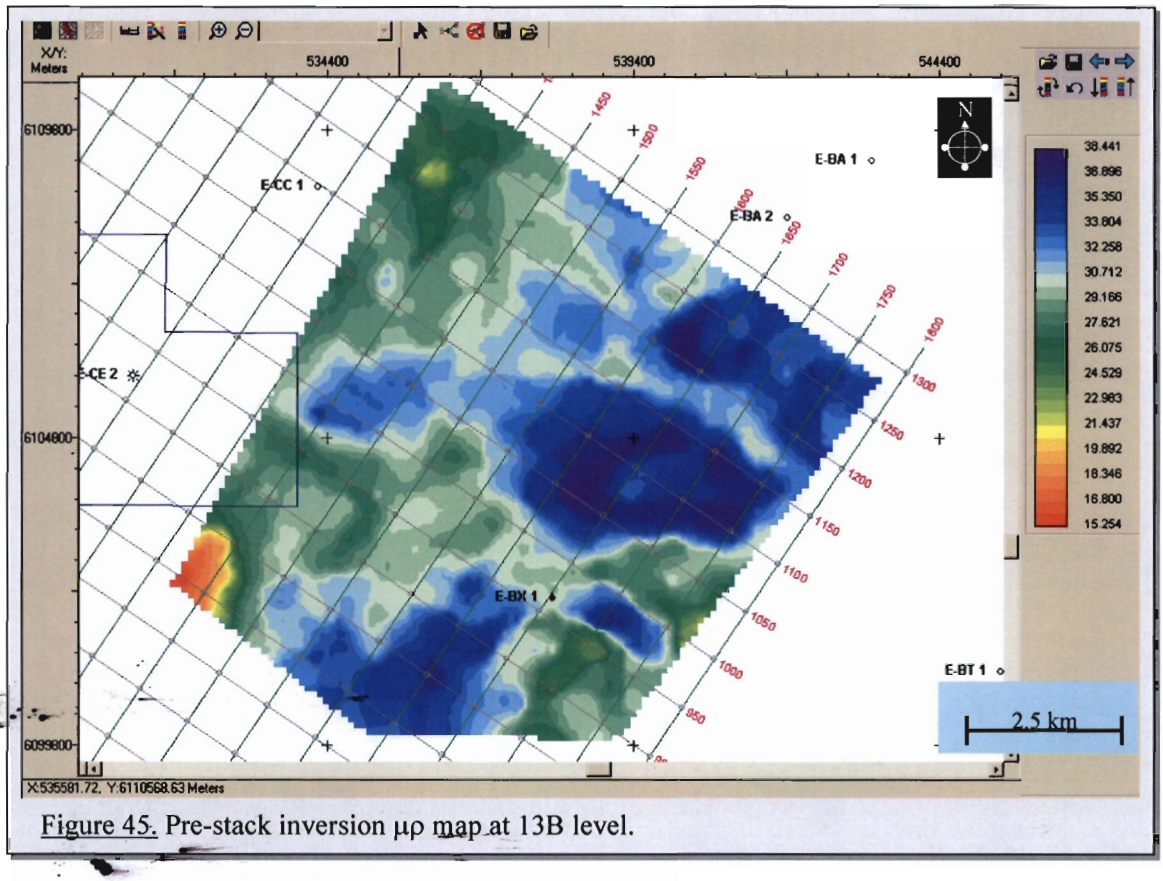

Figure 45. Pre-stack inversion μρ map at 13B level.

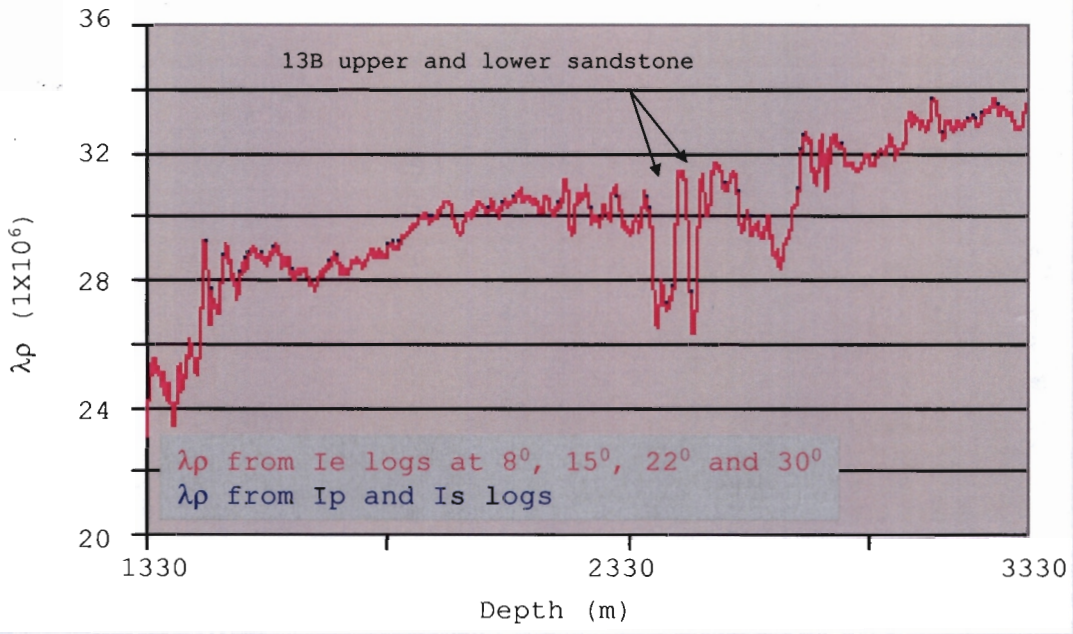

Figure 46: Comparison of λρ from Ip and Is logs (exact), and from four Ie logs at E-BX1.

The λρ and μρ response along the upper 13B sandstone is shown in Figures 44 and 45.

Several quality control steps were added to the pre-stack inversion workflow, to ensure good results at each step. The first potential source of error is not related to the inversion, but rather due to calculating $\lambda\rho$ and $\mu\rho$ from four elastic impedance values by inverting an approximation to Connolly's elastic impedance equation. The log data from E-BX1 were used to determine if a loss of resolution occurs during this step. Figure 46 shows a comparison of the $\lambda\rho$ log calculated from the Vp, Vs and density well logs (exact), and one calculated from four synthetic elastic impedance logs (synthetic inversion). A very good match is obtained between them, indicating no loss of resolution during this step. The same elastic impedance approximation as is tested here, was used to perform the $\lambda\rho$ and $\mu\rho$ calculation on the elastic impedance cubes obtained from the seismic inversion data.

The previous quality control test showed that virtually no error is introduced due to using the Connolly elastic impedance approximation. The remaining sources of error are thus attributed to:

- Seismic noise
- Errors in the low frequency inversion starting model
- Seismic wavelet variations
- Inversion errors (caused by non uniqueness)

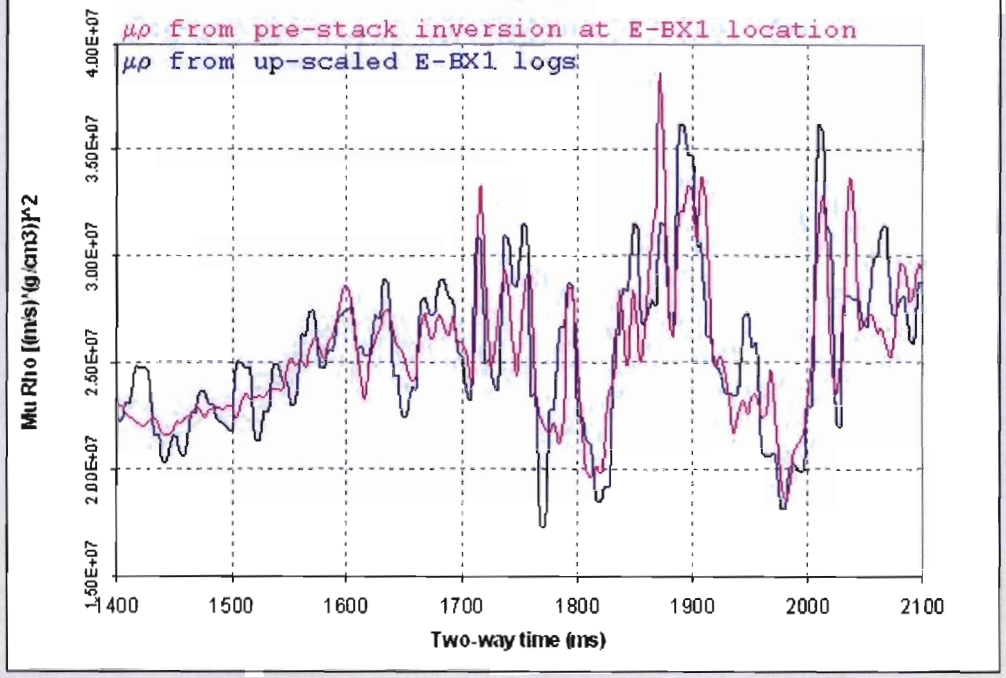

Figure 47. Comparison of $\mu\rho$ from inversion and from up-scaled logs at E-BX1.

Unfortunately the above errors cannot be isolated, and their combined effect was approximated at one location only, namely the well location. Figures 47 and 48 show a comparison of the Backus up-scaled $\lambda\rho$ and $\mu\rho$ logs, calculated from the E-BX1 log data, and the $\lambda\rho$ and $\mu\rho$ trace from the pre-stack inversion. The trace closest to the E-BX1 borehole location was chosen for the comparison. A moderate level of noise is observed in the $\mu\rho$ trace (Figure 47), and a high level of noise is observed in the $\lambda\rho$ trace (Figure 48). It is proposed that most of this noise can be attributed to noise in the seismic data, since the seismic wavelet and low frequency inversion model were calculated from the log data at E-BX1.

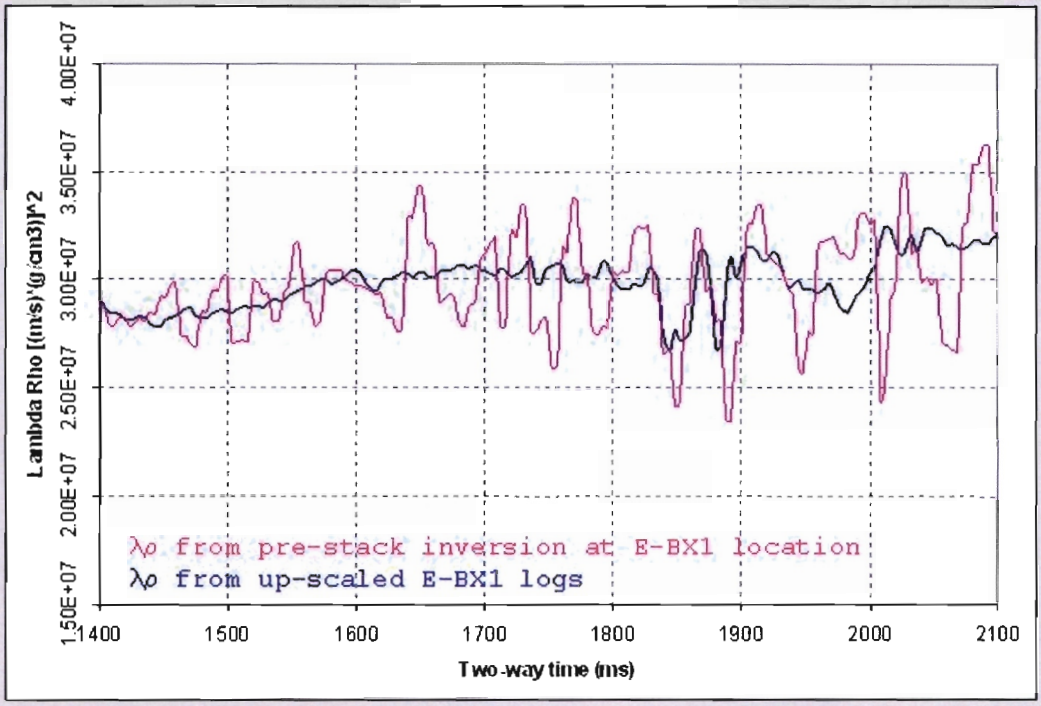

Figure 48. Comparison of λρ from inversion and from up-scaled logs at E-BX1.

The lithological variation recorded by the μρ log is larger than the background noise level. This indicates that the inverted μρ can be used as a lithology discriminator with a relatively high degree of confidence, provided the layers are not below seismic resolution.

The level of noise in the λρ trace is quite high, as can be seen by the ~$6x10^6$ $[(m/s)*(g/cm^3)]^2$ variation around the Backus up-scaled log (Figure 48). λρ is most sensitive to fluid fill. Since no fluid variations are present at this trace (this interval at E-BX1 is water wet), this comparison may not be a fair evaluation of the noise levels in λρ. In section 5.2.2, the Gassmann fluid substitution is discussed in more detail. In this section, it will be shown that an oil saturated 13B sandstone will cause a drop of ~$10x10^6$ $(m/s)*(g/cc)^2$ in λρ. This drop is larger than the estimated background noise, indicating that it is still viable to use λρ as a fluid discriminator at this level.

A comparison of the noise levels in the pre- and post-stack λρ data seem to suggest that the pre-stack λρ is noisier (comparison of Figures 38 and 48).

This was investigated in great detail. The most probable cause of the high levels of noise in the pre-stack attributes is small vertical shifts in the elastic impedance cubes. During the intercept and gradient calculation, the same event may thus not be aligned in the four I_e cubes. Ideally micro-layers need to be introduced during the inversions. These micro layers need to be identical for all starting models, and remain fixed during the inversion. If this "simultaneous" inversion can not be done with the available software, then the post-stack route for generation $\lambda\rho$ and $\mu\rho$ is probably a better approach.

5.2 Training data

The ability of an attribute to discriminate lithology and fluid categories can be determined from log data. At a borehole location, the subsurface lithology and the attributes are known. The attributes are called synthetic attributes, since they are calculated from the log data, rather than from the seismic. It is thus possible to cross-plot the synthetic attributes for different lithology and fluid categories at a borehole. This will show how well the attributes separate the categories. The larger the separation, the better the discriminating power. It is important to realize that log data are recorded at a much higher frequency than seismic data. Since seismic attributes will be used to classify data away from the borehole, it is important to up-scale the synthetic attributes to seismic frequencies prior to cross-plotting them. Backus describes a method of up-scaling data to lower frequencies. This process uses a harmonic average for seismic velocities (Backus, 1962). Figure 49 shows the original and Backus up-scaled sonic and density logs. The 13B interval is at a depth of about 2400m, and can be recognized by a relatively low density. Synthetic LMR attributes were calculated from the up-scaled logs, and cross-plotted over the 13B interval. Figure 50 shows this cross-plot of up-scaled $\lambda\rho$ versus $\mu\rho$ logs over the 13B interval at E-BX1. The data fall into three discrete zones. Each zone represents a lithology with unique elastic parameters. A short discussion on each zone is outlined below;

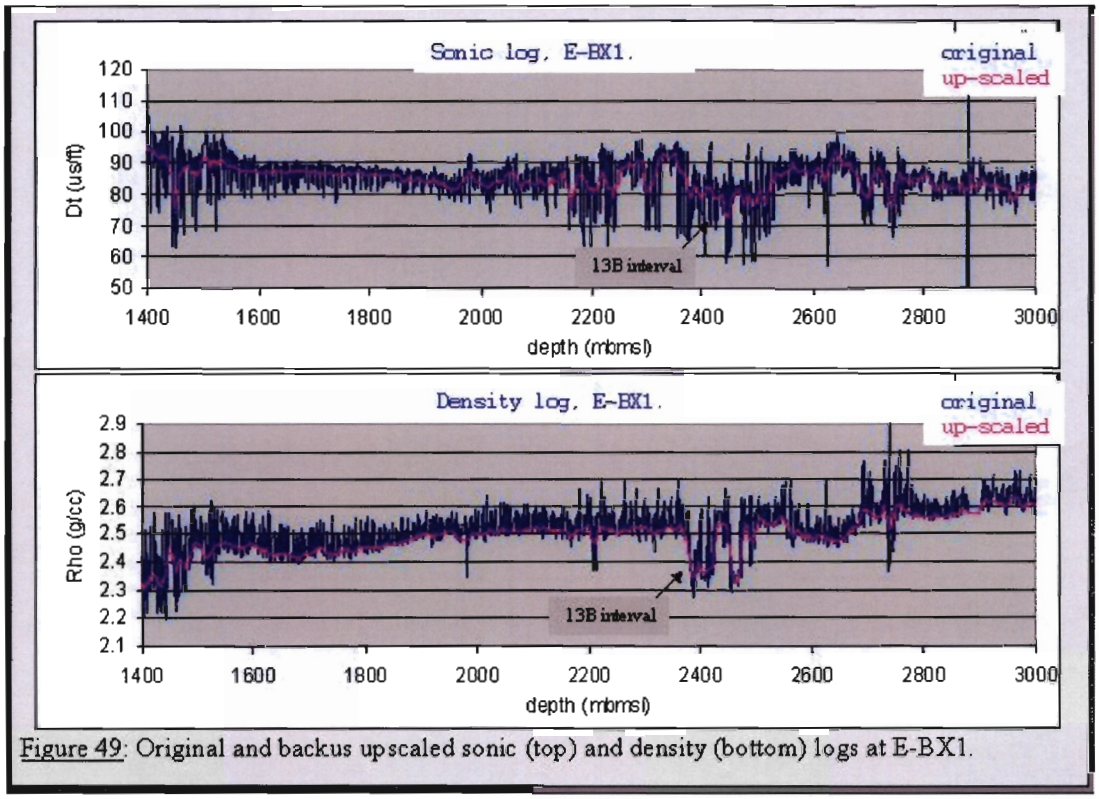

Figure 49: Original and backus upscaled sonic (top) and density (bottom) logs at E-BX1.

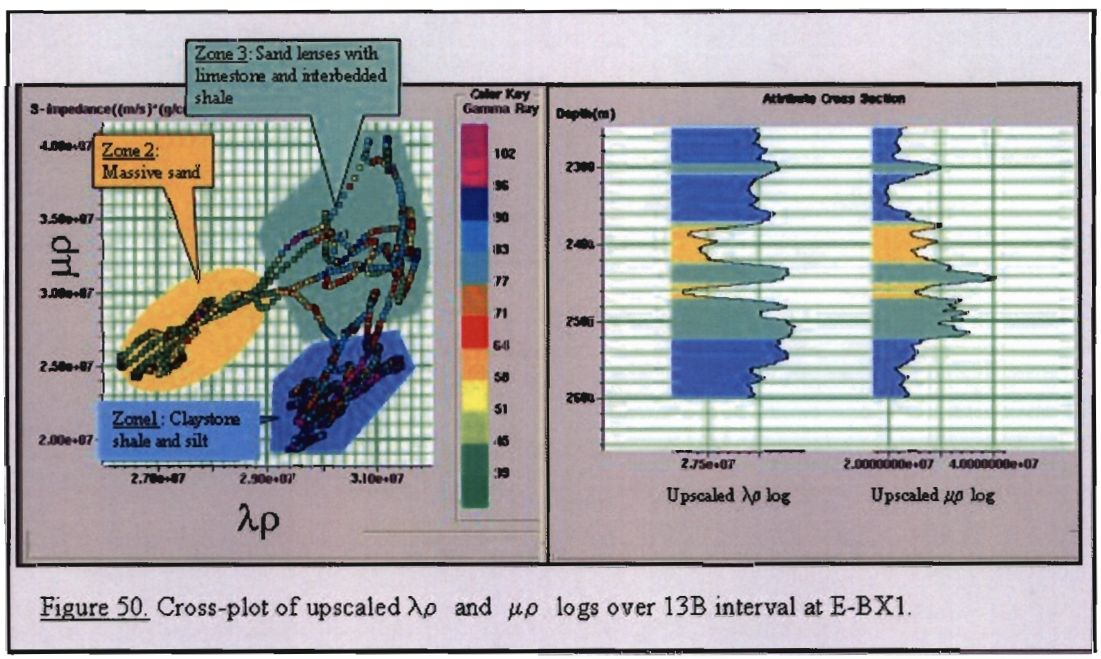

Figure 50. Cross-plot of upscaled $\lambda\rho$ and $\mu\rho$ logs over 13B interval at E-BX1.

· Zone 1, high $\lambda\rho$ and low $\mu\rho$: Claystone / shale is usually associated with a high density and a high incompressibility. This implies that shale / claystone is usually associated with a high $\lambda\rho$ value. The composition and

texture of shale and claystone is usually such that they have a low rigidity. This means that these rocks do not resist shear strain. Despite their high density, they are usually associated with a low $\mu\rho$ response.

· Zone 2, low $\lambda\rho$ and intermediate $\mu\rho$: Massive sandstone encountered at E-BX1 has a lower density than the surrounding shale and interbedded units. The interconnected pore space of sandstone decreases incompressibility and hence a low $\lambda\rho$ is associated with this lithology. The 13B sandstone at E-BX1 has a higher rigidity than the shale. This is owing to the fact that the inter-granular strength of sandstone is higher than that of shale.

· Zone 3, high $\lambda\rho$ and high $\mu\rho$: Calcite-cemented sandstone and silt lenses interbedded with shale. Since these lithologies are interbedded and thin, the up-scaled logs cannot resolve the individual components. The elastic response is thus an average of the various lithologies. The interbedded units fall in the upper right quadrant on the $\lambda\rho$ $\mu\rho$ cross-plot. This is caused by a high density, incompressibility and rigidity. The high density is mainly a result of the shale and dolomite. The high incompressibility (λ) is probably caused by the lack of interconnected pore-space and the high rigidity (μ) is caused by pervasive calcite-cementation of sand and silt lenses. Dolomite is also associated with a high rigidity.

At the E-BX1 well, the distinction between these three lithology groups, as documented in the mudlogger's report, can be achieved best with the density and GR logs over the 13B interval. The cutoffs are shown in Table 1.

	Gamma ray (API)	Density (g/cm^3)
Porous sandstone	GR<70	Rho<2.5
Shale	GR>70	Rho>2.5
Cemented sandstone	GR<70	Rho>2.5

Table 1. Petrophysical cutoffs for the three lithology classes identified over the 13B interval at E-BX1.

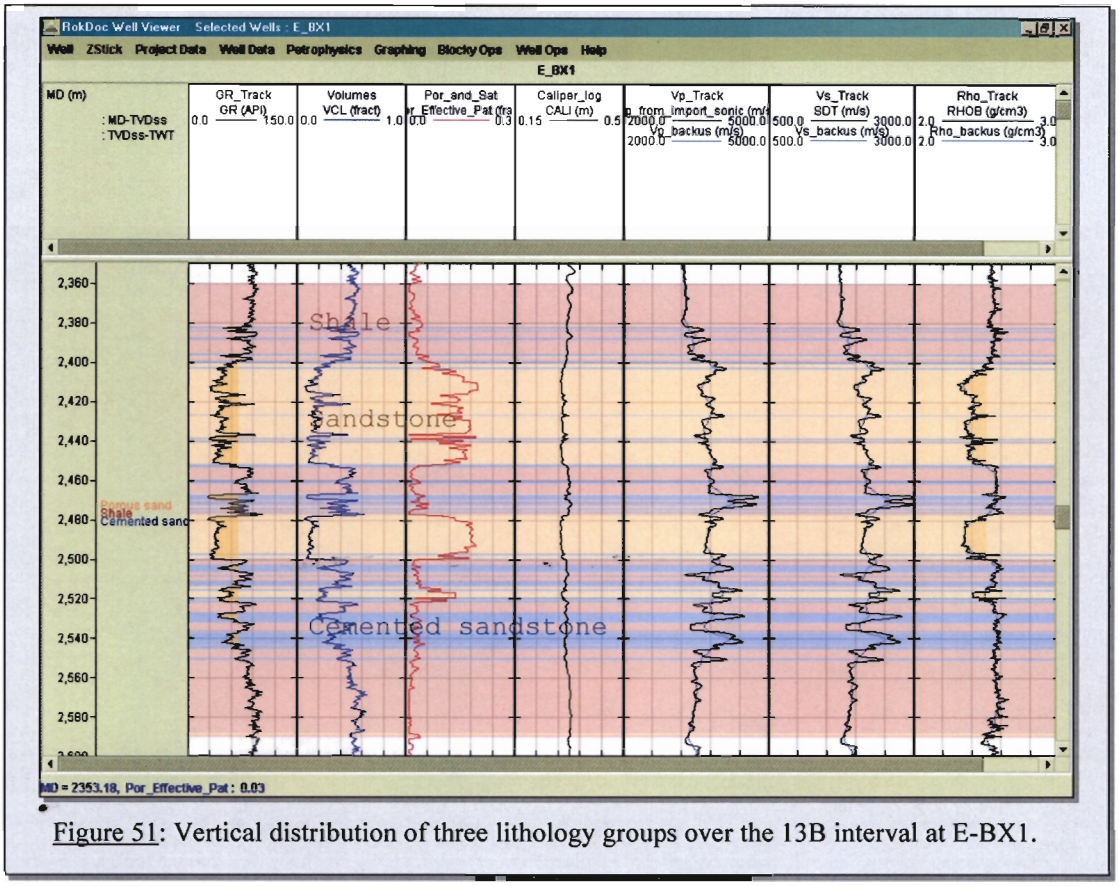

Figure 51: Vertical distribution of three lithology groups over the 13B interval at E-BX1.

Figure 51 shows the vertical distribution of the three lithology groups over the 13B interval at E-BX1. This grouping was used to extract the up-scaled $\lambda\rho$ and $\mu\rho$ values for the training data. This is shown in Figure 52, and forms the basis of the training data for the classification. The ability to discriminate between the three lithology classes is a function of the amount of overlap between data of the classes. This discriminating ability (or amount of separation) can be measured. As a first step, the 2-dimensional probability density function (PDF) for each class is calculated. This is in essence a plot of the probability of a sample belonging to one of the three classes, given the training data. Since a third dimension (namely probability) is introduced in a PDF, it can be displayed either as a contour plot (Figure 53), or as a 3D plot (Figure 54). The discriminating ability of a training dataset can also be calculated numerically through validation (section 3.2.1). Validation calculates all permutations of the probability of a sample belonging to different classes.

Validation is expressed as the classification success ratio matrix (P). The matrix P for the un-extended training data are shown in Table 2.

Classified group	Actual group		
	Sandstone	Shale	Cement
Sandstone	91%	3%	6%
Shale	0%	92%	8%
Cement	1%	20%	80%

Table 2. Classification success ratio matrix (P) of the un-extended training data.

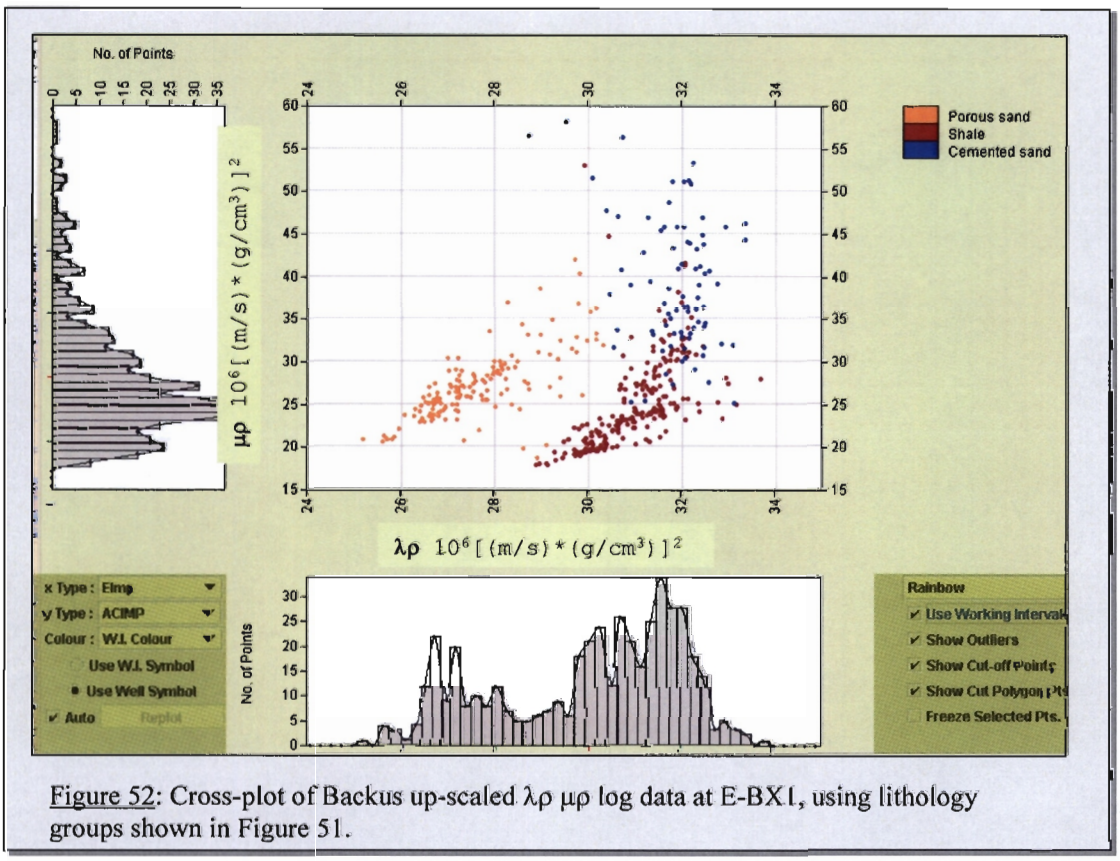

Figure 52: Cross-plot of Backus up-scaled λρ μρ log data at E-BX1, using lithology groups shown in Figure 51.

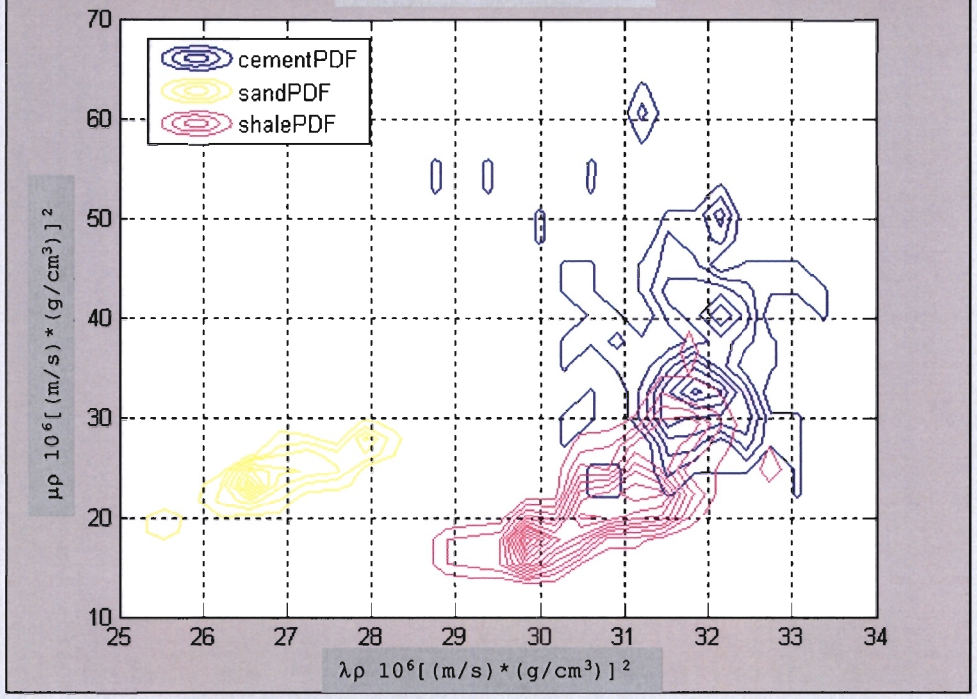

Figure 53. Contour plot of the raw PDFs of the un-extended training data.

The diagonal elements of P are the probability that the data corresponding to a certain class are correctly classified. The "cement" class has the lowest chance of being correctly classified, whereas the "shale" class has the highest chance. The differences arise from the shape of the training data cloud. A higher overlap with other groups results in a greater chance of misclassification. The off-diagonal elements of P represent the various chances of misclassification. For example, the chance of a shale sample being classified as cement is 20%, and the chance of a cement sample being classified as shale is 8% and so forth.

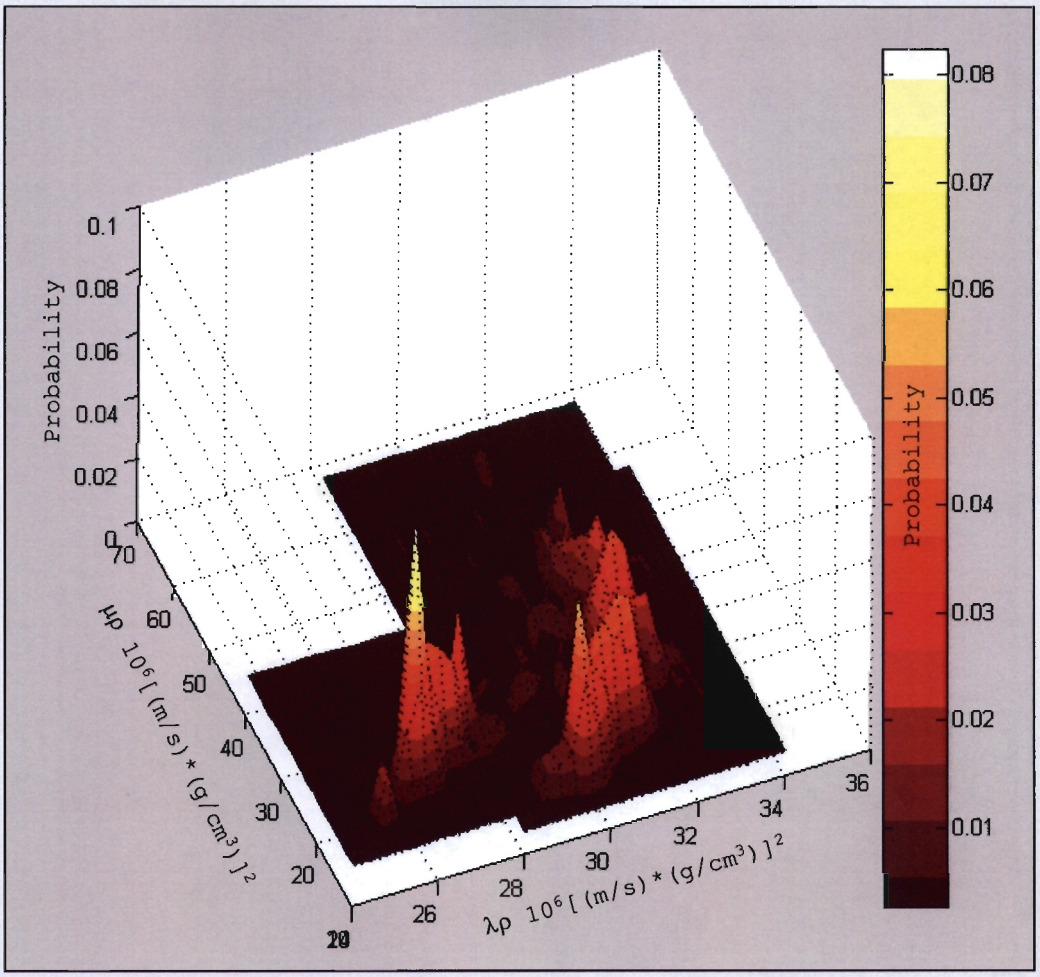

Figure 54: Probability plot of the raw PDFs of the un-extended training data.

Once the PDFs and the classification success ratio matrix have been calculated from the training data, one is now in a position to classify any data into the various categories. A nice way to visualize the classification is to input a regular sample grid, for example a grid of $\lambda\rho$ and $\mu\rho$ points at an interval of 2.5 X 10^6[(m/s)*(g/cm^3)]^2 (Figure 55). These sample data are input to a "Mahalanobis" classification, using the log data as training data (also called "prior" or "supervisor"). Figure 56 shows the results of the Mahalanobis classification on the regular input grid. The classification was done in the statistics toolbox in Matlab. Both the training data and the classified sample data are shown. In areas of overlapping training data, misclassification occurs, as described by the off-diagonal elements of the classification success ratio matrix (P), shown in Table 2.

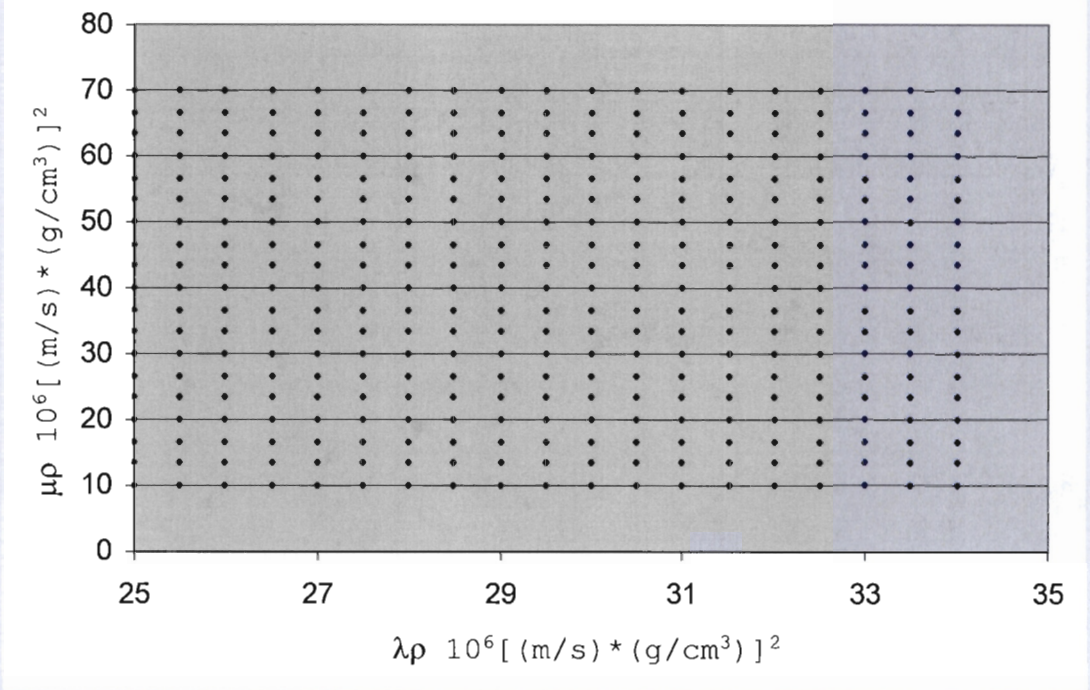

Figure 55: Regular sample data grid to test classification

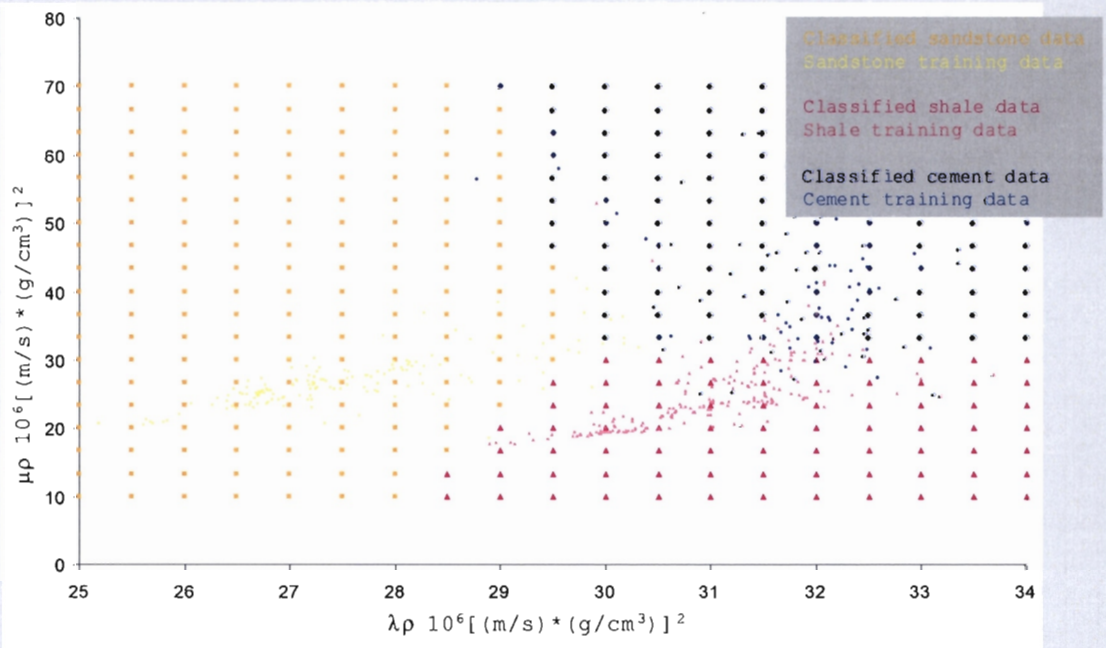

Figure 56. Mock classification using un-extended training data.

5.2.1 Extending the training data

The training data used for the classification in the previous paragraph were derived from wireline log data at borehole E-BX1. Due to lateral lithology and fluid variations, the log data are not a representative sample of the expected $\lambda\rho$ and $\mu\rho$ values of the 13B sequence away from E-BX1. This implies that the log data alone are not suitable as training data for lithology and fluid classifications. The training data need to be extended to incorporate the true variability over the study area. Unfortunately the true lithology and fluid variability of the 13B sequence around E-BX1 is not known, and in order to obtain a representative sample of the variability, the log data need to be extended through fluid and lithology substitution.

Extending of training data can be done in two ways. Firstly, additional groups can be added to the training data, and secondly, additional data points can be added to existing groups. In this study, the fluid substitution will add a fourth group (or class) to our training data, namely, oil-saturated sandstone. The lithology substitution, on the other hand, will only add data to one existing group, namely water-bearing sandstone.

5.2.2 Extending the training data through fluid substitution

The $\lambda\rho$ of a saturated rock decreases when its pore-filling brine is replaced with oil or gas. The 13B sequence is situated in an oil-prone fairway, and the aim of the seismic classification is to detect the presence of oil-saturated sandstone. In order to achieve this, the training data from the water-wet 13B sandstone at E-BX1 needed to be extended to include the seismic response from oil-bearing sandstone. The Gassmann equations are commonly used for fluid substitutions (section 3.1.6). The equations were set up using the rock properties of the 13B sandstone at E-BX1. The wireline log data, and Vp Vs analysis (section 4.1 and 4.6) were used to calculate the elastic rock

properties, which are required as input data. Furthermore, the fluid properties of the initial pore-fluid were calculated from the temperature and salinity of the 13B brine, as recorded at E-BX1. The fluid properties for the oil were obtained from known parameters of the nearby Sable oil field's E-BD wells (Figure 6). The following table summarizes the fluid parameters used for the fluid substitution. The values labeled "E-BX1" in the first row show the parameters used, and the values labeled "Default" in the second row are average values from data around the world, shown for comparison.

	Water			Oil		
Name	Density (g/cm^3)	Vp (m/s)	K	Density (g/cm^3)	Vp (m/s)	K
E-BX1	1	1631	2.66	0.845	1088	1
Default	1	1600	2.56	0.8	1200	1.152

Table 3. Fluid parameters used for the fluid substitution.

The Gassmann equations were used to derive the Vp, Vs and density of oil saturated 13B sandstone. Two oil-saturations were used, namely 85% and 75%. These saturations encapsulate the common range of oil saturations in nearby fields. The fluid-substituted data were Backus up-scaled and subsequently used to calculate $\lambda\rho$ and $\mu\rho$ values for the oil-saturated sandstone, which is the fourth data-class for the training data. This modeling was done using the RokDoc software. Figure 57 shows the cross-plot of the four training groups.

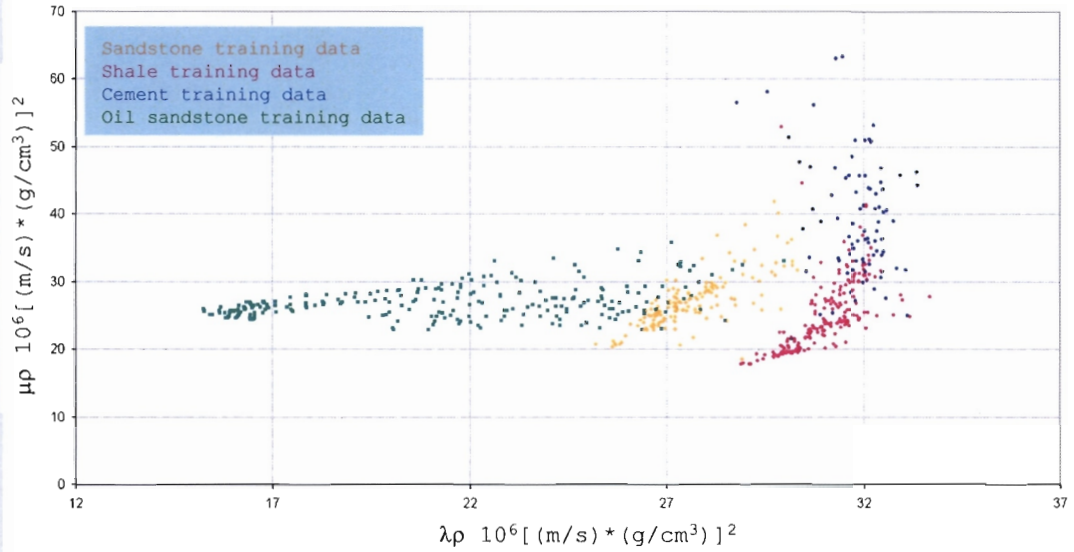

Figure 57. Fluid-extended training data.

Since the training data have changed, the discriminating ability has also changed. The classification success ratio matrix of the new training set can measure the change in discriminating ability. The classification success ratio matrix (P) for the new training data, which includes a new group of oil-saturated sandstone, is shown in table 4.

Classified group	Actual group			
	Sandstone	Shale	Cement	Oil sandstone
Sandstone	92%	2%	7%	0%
Shale	0%	92%	8%	0%
Cement	1%	19%	80%	0%
Oil sandstone	26%	0%	1%	73%

Table 4. Classification success ratio matrix (P) of the fluid-extended training data.

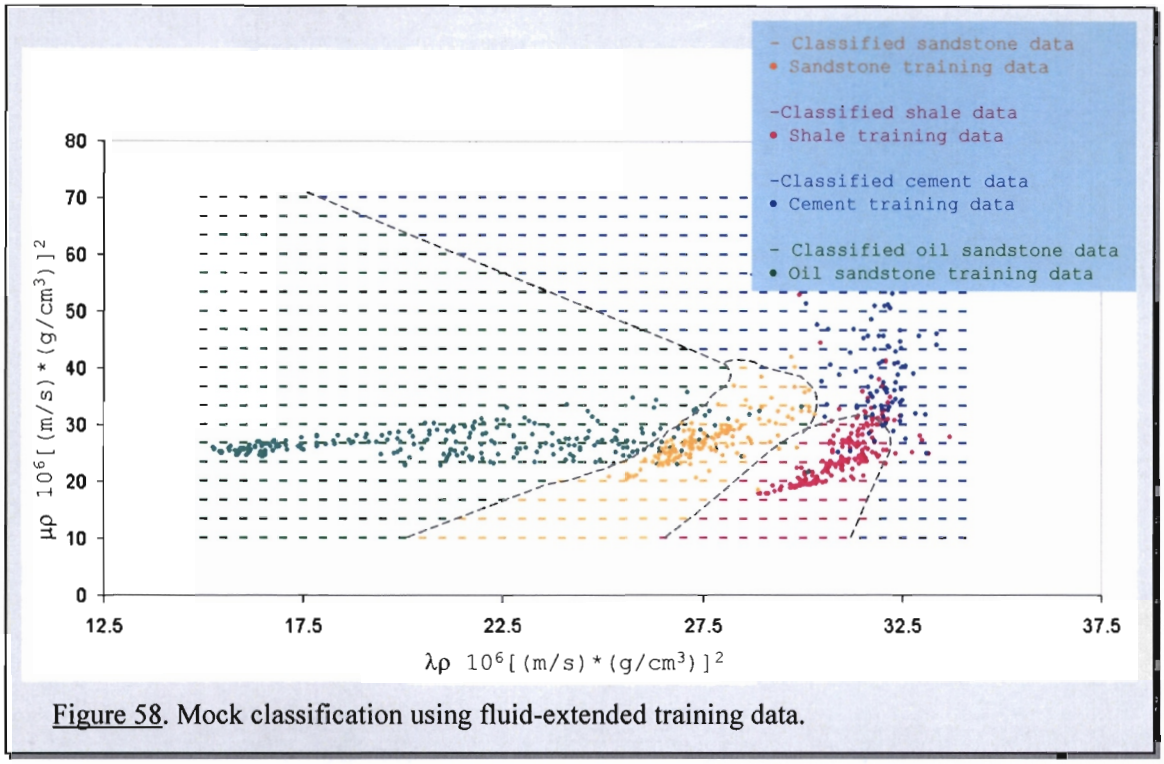

Figure 58. Mock classification using fluid-extended training data.

Another way to visualize the discriminating ability of the fluid-extended training data is through a mock-classification of a regular data grid. Figure 58 shows how regular $\lambda\rho$ and $\mu\rho$ data will be classified when using the fluid-extended training data. Note that both the classified data grid and the training data are plotted. The classification was done with the Mahalanobis classifier.

5.2.3 Extending the training data through lithology substitution

In the previous section, a fourth group was introduced to the training data through fluid substitution. In this section, the oil- and brine filled sandstone groups will be extended through lithology substitution. This implies that the effect of changing the porosity and clay content in the sandstone will increase the variability in the $\lambda\rho$ and $\mu\rho$ values associated with the groups. This in turn can reduce the ability to discriminate between groups, by increasing the amount of overlap with other groups. The lithology substitution of the sandstone groups is performed with the Xu-White (1995) equations (section 3.1.7), using the RokDoc software. The Xu-White algorithm uses the Kuster

and Toksöz (1974) differential effective medium equations to calculate the change in elastic properties when the porosity and clay content in sandstone is varied.

In their paper, Xu and White propose that a large amount of scatter is present in the velocity-porosity relationship of water-bearing sandstone (Xu and White, 1995). This scatter can be mainly attributed to clay particles that have a different shape from sand grains, and thus propagate sound waves differently. The following figure is taken from the Xu and White paper of 1995, showing the common amount of scatter in the velocity-porosity relationship of sandstone.

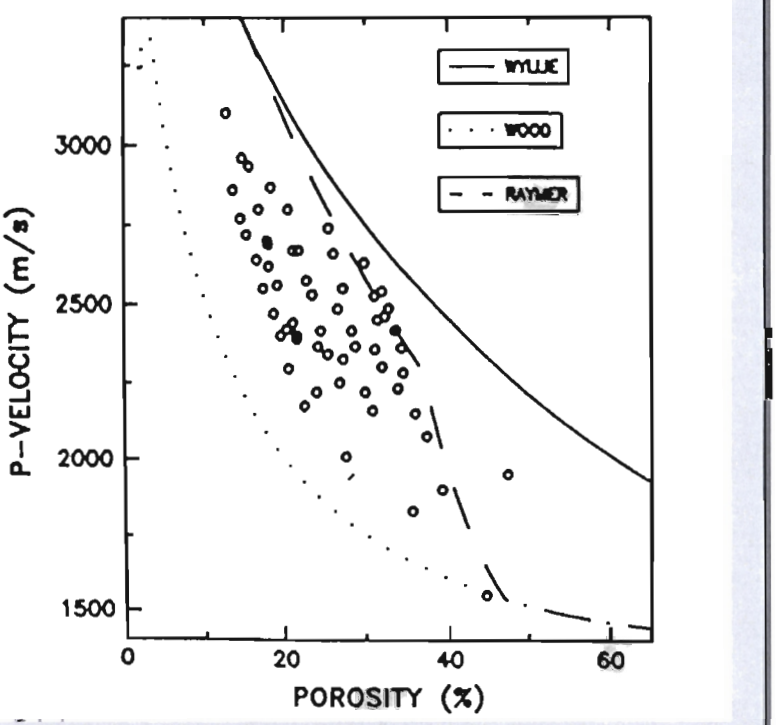

Figure 59. Cross plot of Vp and porosity data from Gulf of Mexico sandstone (taken from Xu and White, 1995).

The velocity-porosity plot for the 13B sandstone at E-BX1 looks very similar, and is shown in Figure 60.

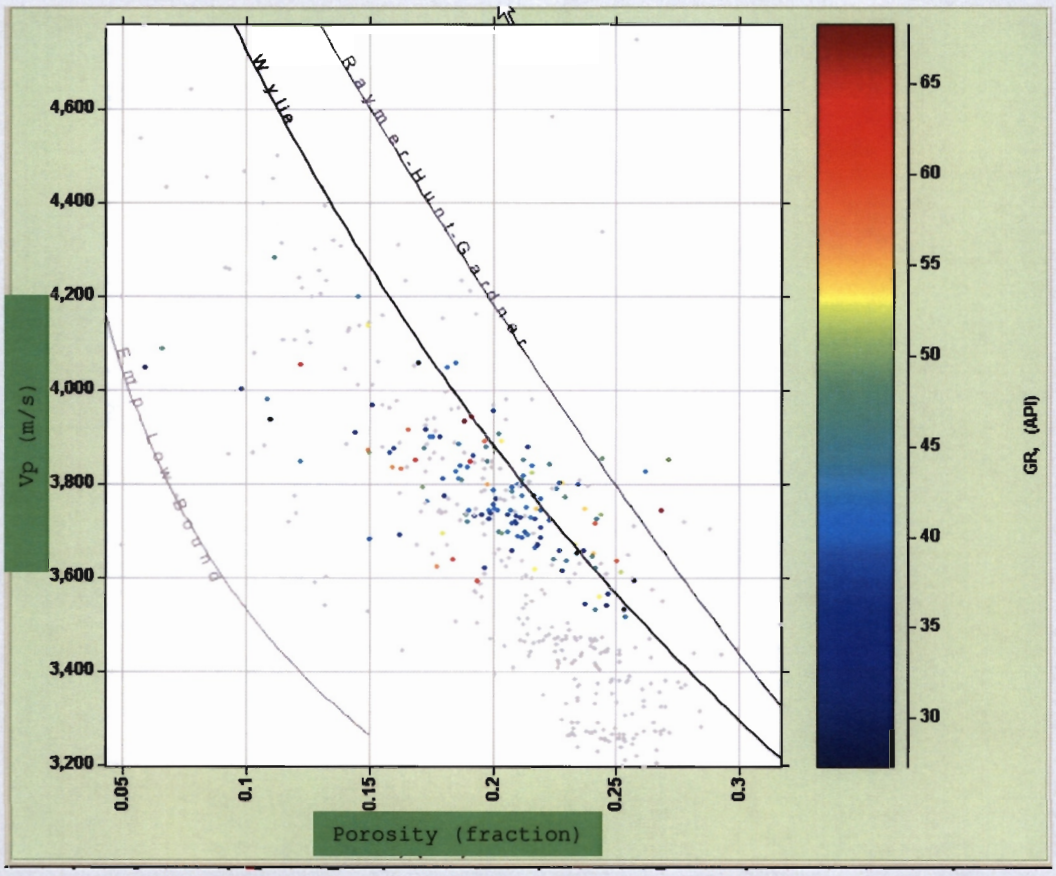

Figure 60. Cross plot of Vp and porosity log data of the 13B sandstone interval at E-BX1. Colour of data points indicates the gamma ray value of data points. The grey data points are data from outside the 13B interval.

For the purposes of lithology extension, this implies that the true variability of sandstone Vp, is larger than predicted with, for example, Wyllie's equation. The Xu-White equation is better suited for lithology extension since it is capable of predicting the scatter of Vp through inclusion of the clay particles in the effective medium. The details of the Xu-White equations have been discussed in section 3.1.7. It has been mentioned that the equations require knowledge of the elastic properties of the sand and clay particles, as well as the aspect ratios of the pore space associated with each. These parameters can be determined with laboratory analyses of core samples. Unfortunately there are no core samples for the 13B sandstone from E-BX1. The wireline log data (mainly the sonic velocity and density log data) was used to calculate

the elastic properties of the 13B sandstone and shale. In order to estimate the aspect ratios of the sand and shale pores, the Xu-White relationship was calibrated to fit the log data. This calibration can be done in several ways. One way is to cross-plot Vp and volume clay (VCL) log data over the sandstone interval. This is shown in Figure 61.

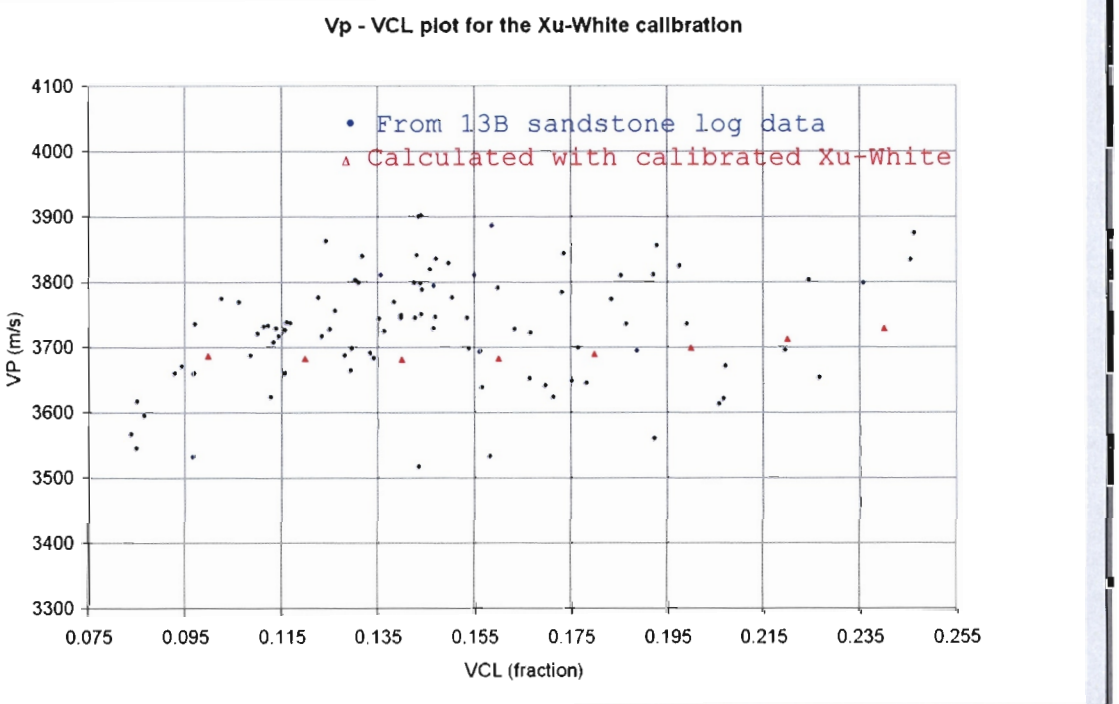

Figure 61. Cross plot of Vp and VCL data for Xu-White calibration.

The blue data points in Figure 61 show the recorded log data over the 13B interval at E-BX1. A general increase in velocity with clay volume is noted. These data were used to calibrate the Xu-White relationship. Eight VCL values were chosen as calibration points. They are shown as red triangles in Figure 61. Three parameters were calibrated to match the red calibration points with the Vp values of the blue data points in Figure 61; namely the sandstone- and the shale pore aspect ratios, and the relationship between porosity and VCL. Changing the pore aspect ratios has a large influence on the magnitude of Vp. A reasonable match was obtained using a sandstone pore aspect ratio of 0.4, and a shale pore aspect ratio of 0.2. Furthermore, in

order to match the increase of Vp with VCL, an inverse relationship between porosity and VCL was used. This relationship is given below, and was derived from log data over the 13B interval at E-BX1.

$$VCL = -0.96\phi + 0.34 \qquad (18)$$

VCL *Clay volume (fraction)*

ϕ *porosity (fraction)*

Another way to calibrate the Xu-White equation is on a $\lambda\rho$ $\mu\rho$ cross-plot. Since $\lambda\rho$ and $\mu\rho$ are calculated from Vp, Vs and density (the three outputs of the Xu-White equation), this is a more comprehensive calibration than only calibrating Vp. Figure 62 shows the $\lambda\rho$ $\mu\rho$ cross-plot with all the training data thus far. The 13B sandstone values at E-BX1 are plotted in yellow. Superimposed in red, are the $\lambda\rho$ and $\mu\rho$ values calculated using the Xu-White equations with the elastic rock and fluid parameters from E-BX1. In order to match the extent of the $\lambda\rho$ and $\mu\rho$ values of the 13B sandstone at E-BX1, the following variability of input parameters to the Xu-White equations was required;

1. Aspect ratios: 0.3 to 0.5 for sandstone, and 0.1 to 0.3 for shale.
2. Porosity values: 12% to 20%
3. VCL: 12% to 23%.

The variation of porosity and VCL required to match the $\lambda\rho$ and $\mu\rho$ data extents of the recorded data, as shown in Figure 62, fits well with the variation in porosity and VCL values of the 13B sandstone at E-BX1. This was a good quality control check to ensure correct application of the Xu-White equation. The inverse relationship between porosity and VCL mentioned in the Vp calibration (Figure 61), was also imposed for this calibration, but with a certain degree of flexibility, as indicated by the scatter in the actual log data.

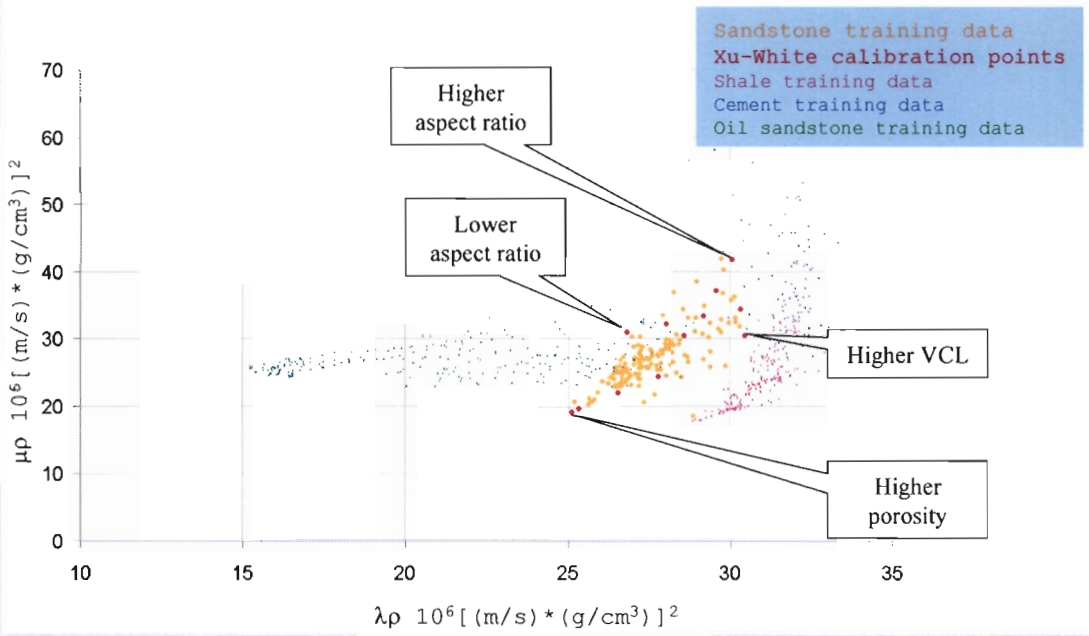

Figure 62. Cross-plot of λρ and μρ for Xu-White calibration.

Once the Xu-White relationship had been calibrated, the next step was to determine the expected variation of porosity and VCL of the 13B sandstone in the study area. The variations of these parameters needed to follow from the geological depositional model of the sandstone. It is a subjective matter, and the accuracy of this prediction depends on the amount of regional information and knowledge about the paleo-depositional environment and subsequent diagenesis of the rocks.

The depositional model for the 13B sandstone around E-BX1 was discussed in detail in section 4.4. The information that follows from this model is described briefly below.

Sandstone belonging to the 13B sequence around E-BX1 was deposited as slope-front and basin-floor prograding turbidites. Figure 63 shows a model for these depositional environments (Reading and Richards, 1994).

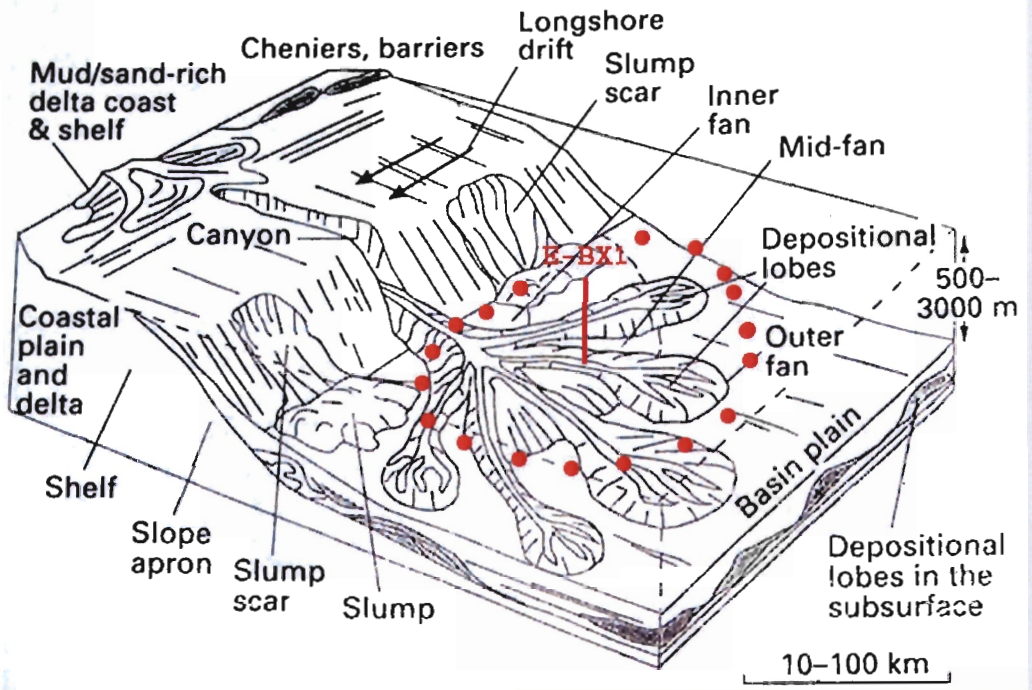

Figure 63: Depositional model for mud and sand rich submarine fans (taken from Reading and Richards, 1994)

Borehole E-BX1 was drilled close to one of the channel axes of the mid-fan, as indicated in the figure. The red dots in Figure 63 outline the approximate extent of the study area. The model suggests that the data at E-BX1 sample high porosity, low clay-content 13B sandstone. The porosity may increase slightly towards the upper fan channel axes, but may decrease significantly towards the outer fan, and away from channel axes. It should be kept in mind that the porosity is mainly of secondary nature (section 4.4) due to early calcite cementing and later leaching. Despite this, the highest porosity is still expected in massive channel sandstone with a high permeability, where leaching acids migrated through the pores. For the purposes of the lithology extension, a porosity variation from 10% to 24% was used. For the VCL in the 13B sandstone, the model again suggests a large variability. Borehole E-BX1 sampled the low end of VCL in the 13B sandstone, because it was supposedly drilled close to the channel axis in the mid-fan. VCL is expected to decrease slightly towards the inner fan, but mainly increase towards the outer fan and away from the channel axes. For the purposes of lithology

extension, a VCL range of 10% – 30% was used. It should be noted that the geological model supports an inverse relationship between VCL and porosity, as the E-BX1 wireline log data suggest (Figure 61).

The Xu-White lithology extension was divided into two parts. Firstly, the response from inner fan channelised sandstone was calculated (Figure 63). This sandstone is expected to have a higher porosity and a lower VCL than at E-BX1, which is located more distally. A porosity range of 20% to 24%, and a VCL range of 10% to 18% was used in the Xu-White equations to calculate the response of the high porosity, massive sandstone of the inner fan. The second part of the lithology extension was to calculate the response of the more shaley outer fan 13B sandstone. A range of 20% to 30% VCL; and a range of 10% to 15% porosity was used in the Xu-White equation to determine their response.

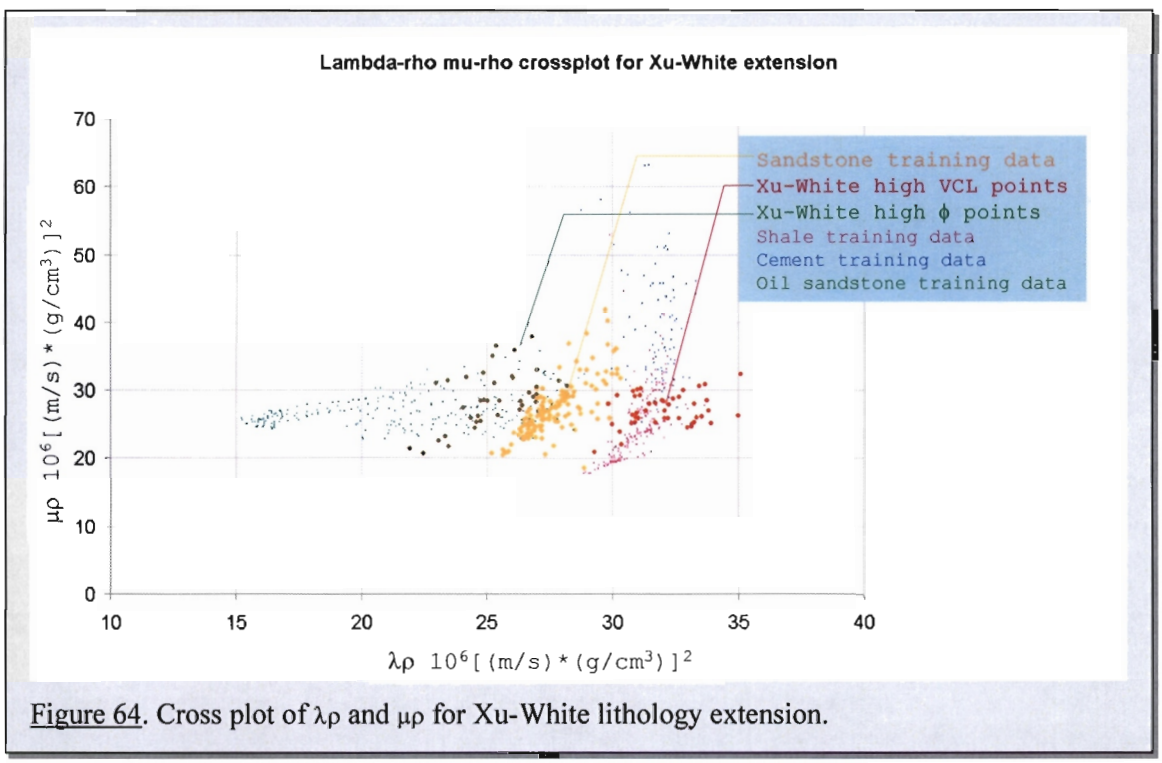

Figure 64. Cross plot of λρ and μρ for Xu-White lithology extension.

The data from the lithology extension are shown in Figure 64. The response from the high porosity inner fan sandstone is shown in bold green points. These points have a lower $\lambda\rho$ value than the 13B sandstone at E-BX1, and overlap with the values of the oil-substituted sandstone values. The response from the higher VCL sandstone of the outer fan is shown as bold red points in Figure 64. These data have a higher $\lambda\rho$ response than those of the 13B sandstone at E-BX1, and overlap with the parts of the shale data points of the training data. Some points of the extended training data have even higher $\lambda\rho$ values that the shale values. The cause of this phenomenon was investigated in some more detail. A closer review of the shale training data suggests that the intervals from which the data were derived (Figure 51) contain a fair amount of silt. This may explain the discrepancy.

This concludes the extension of the training data. As has been mentioned before, the fluid extension (section 5.2.2) added a fourth group to the training data, namely oil-saturated sandstone, whereas the lithology extension only added variability to the water sandstone group, by including a larger range of VCL and porosity. The effect of this increase in variability decreases the ability to discriminate between groups, because more overlap between groups occurs. This can be demonstrated by calculating the classification success ratio matrix (P) for the extended training data, and comparing it to that of the un-extended training data.

Classified group	Actual group			
	Sandstone	Shale	Cement	Oil sandstone
Sandstone	72%	17%	5%	6%
Shale	3%	90%	7%	0%
Cement	1%	19%	80%	0%
Oil sandstone	24%	5%	0%	70%

Table 5. Classification success ratio matrix of the fluid- and lithology-extended training data.

The lithology extension has decreased the ability of the training data to discriminate between groups. Most severely affected is the sandstone group, whose classification success rate has dropped by 20%, from 92% (Table 4) to 72% (Table 5). The classification success rate for the shale and the oil-saturated sandstone has also decreased by extending the training data. Further extensions on the training data are possible, for example, the oil-saturated sandstone data could be extended to different porosity and VCL ranges. Similarly, the calcite and dolomite ratios of the cemented sandstone data could be varied, as well as the silt content in the shale intervals. For the purpose of this study, only the water-bearing sandstone was lithology-extended, in order to determine if variations in porosity and VCL can overshadow fluid effects in the 13B sandstone around E-BX1.

A mock classification, using a regular $\lambda\rho$ and $\mu\rho$ data grid was also performed using the final, extended training data and the Mahalanobis classifier. The results are shown in Figure 65.

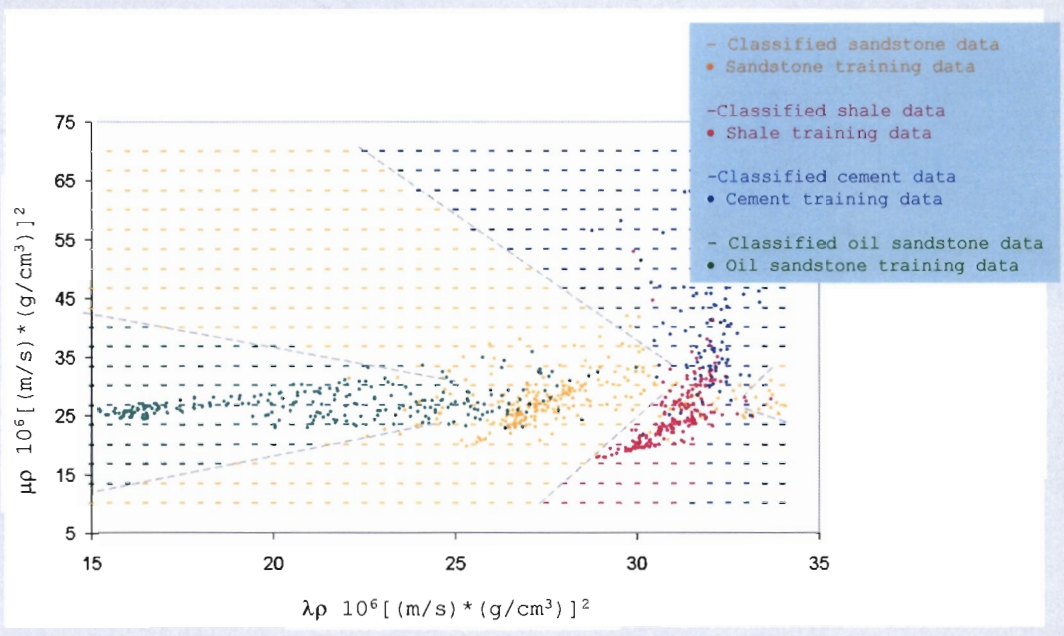

Figure 65. Mock classification using the fluid- and lithology extended training data.

In Figure 65, there is a large area that will be classified as water-bearing sandstone (for example), despite being far away from any training data. This is simply as a result of a lack of training data with those values, and the algorithm being forced to assign the data to a category. This problem is overcome by calculating the probability of the data belonging to a group. In areas far away from training data, the probability of the data belonging to a training group will be zero. This is discussed in more detail in the following paragraph.

The classification algorithm can also be used to calculate the probability that the data belong to a certain group. The probability of sample "i" belonging to group "j" is expressed as Pij, which can be calculated for each sample in the training data, and for each group. The PDFs for each group are used to derive the probabilities. Avseth suggests that the PDFs are smoothed before they are used to calculate probabilities (Avseth et al., 2005). This ensures that data sampling artifacts are removed. For this study, the PDFs were smoothed with a two dimensional Gaussian filter. The size of the filter was chosen such that the overall shape of each training group and the interference between groups was preserved, but data spikes were removed. The filter also honored the requirement that the sum of probabilities at any point may not exceed 1. The PDF calculations were performed in Matlab, and are best illustrated with the regular training data grid. Figures 66 to 69 show the probability of data belonging to the following groups respectively; water-bearing sandstone, shale, calcite-cemented sandstone and oil-saturated sandstone, using the extended $\lambda\rho$ and $\mu\rho$ training data.

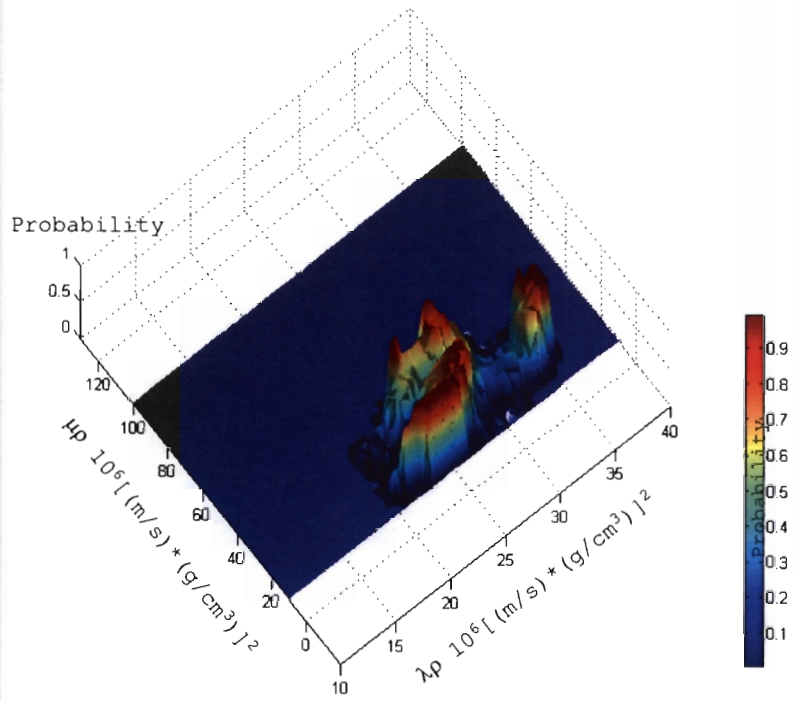

Figure 66. Probability of water-bearing sandstone, on regular data grid.

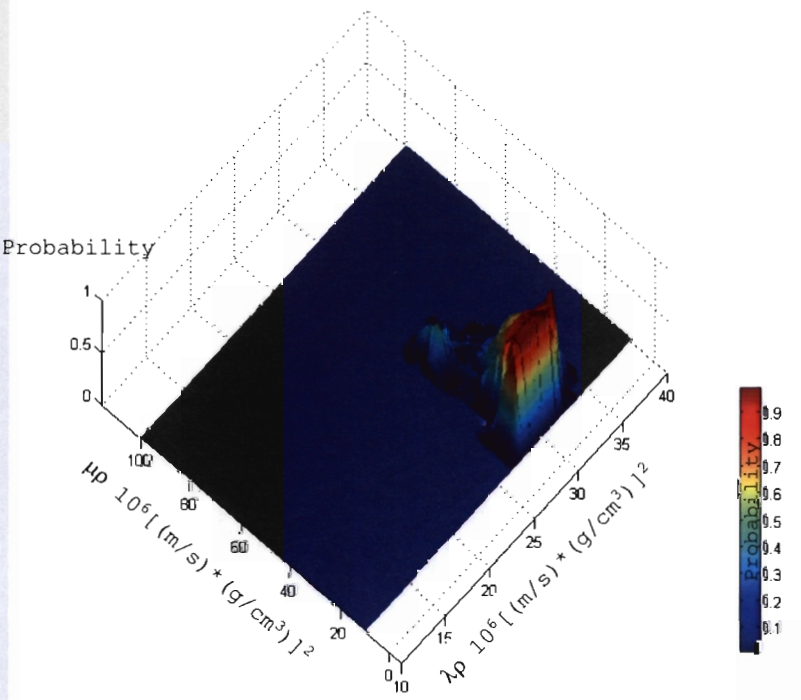

Figure 67. Probability of shale, on regular data grid.

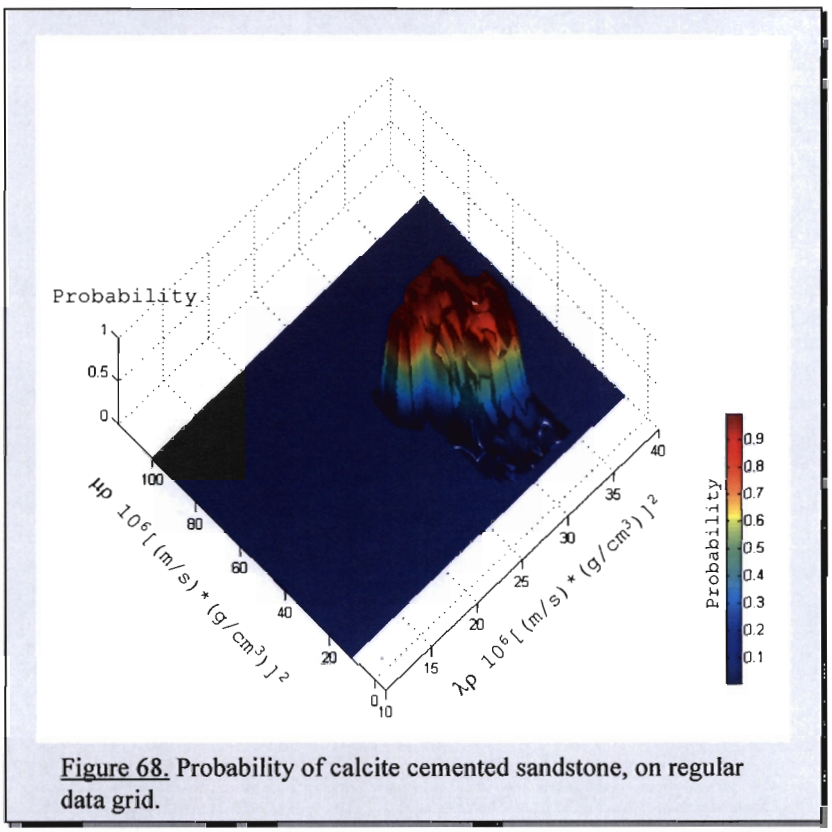

Figure 68. Probability of calcite cemented sandstone, on regular data grid.

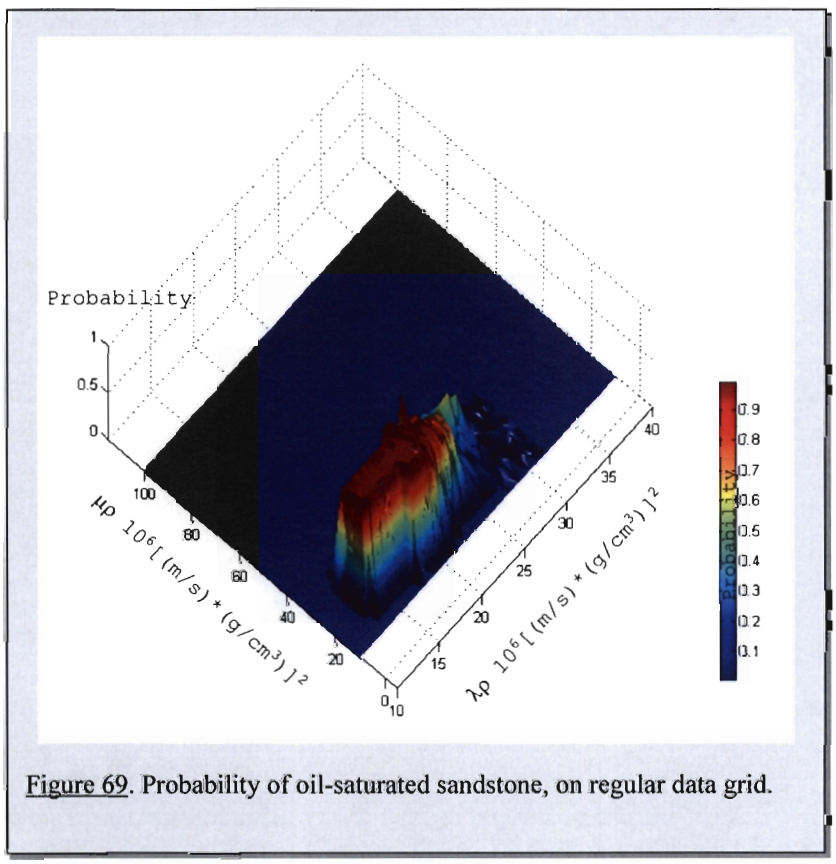

Figure 69. Probability of oil-saturated sandstone, on regular data grid.

6 Results and Conclusions

In this last chapter, the results of the classification on real data will be presented and discussed. Two sets of classifications were performed, one with the post-stack inversion $\lambda\rho$ and $\mu\rho$ attributes, and another with the pre-stack inversion $\lambda\rho$ and $\mu\rho$ attributes (section 5.1). Both classifications were performed with the fluid- and lithology-extended training data (section 5.2). Figures 70 to 73 show maps of the probability of the four classification groups, namely water-bearing sandstone, shale, calcite-cemented sandstone and oil-bearing sandstone, as calculated from the post-stack inversion $\lambda\rho$ and $\mu\rho$ attributes. The results apply to an interval corresponding to the upper 13B sandstone.

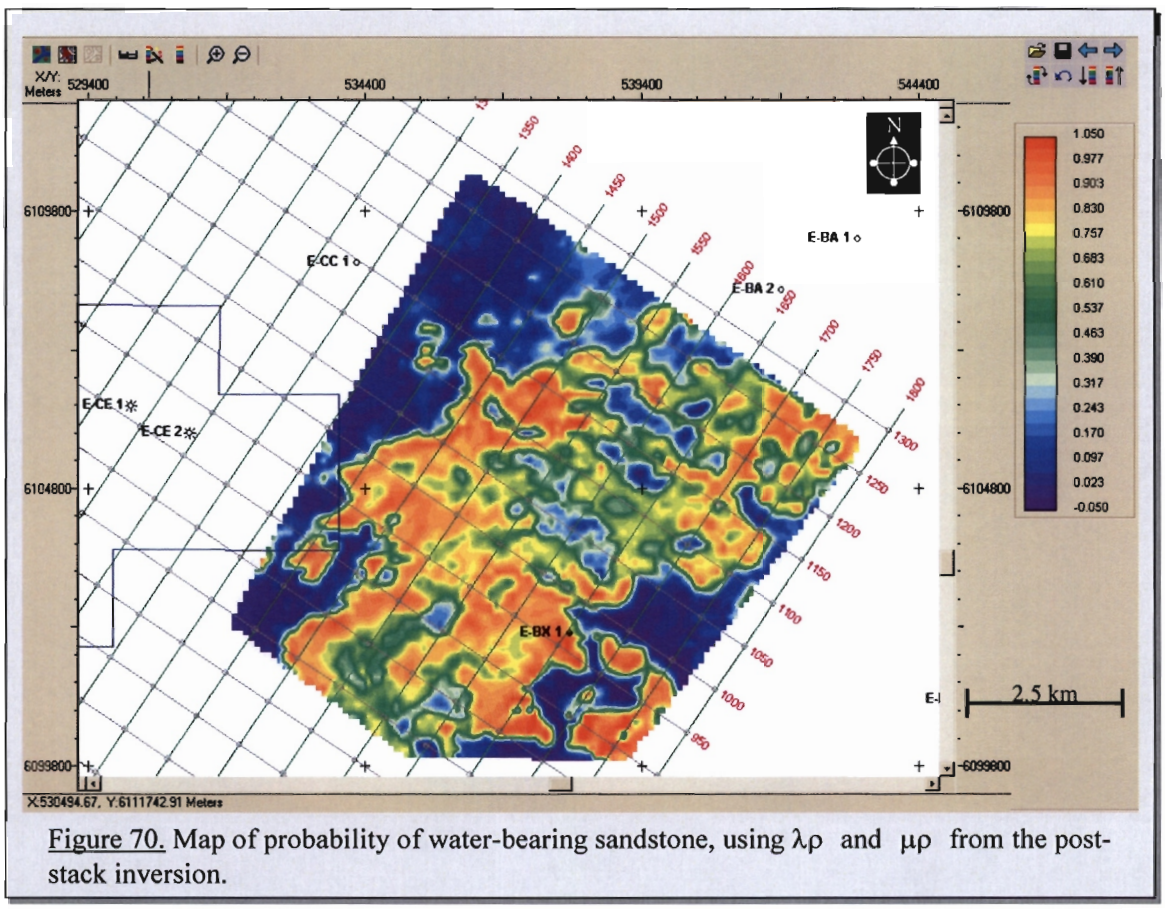

Figure 70. Map of probability of water-bearing sandstone, using $\lambda\rho$ and $\mu\rho$ from the post-stack inversion.

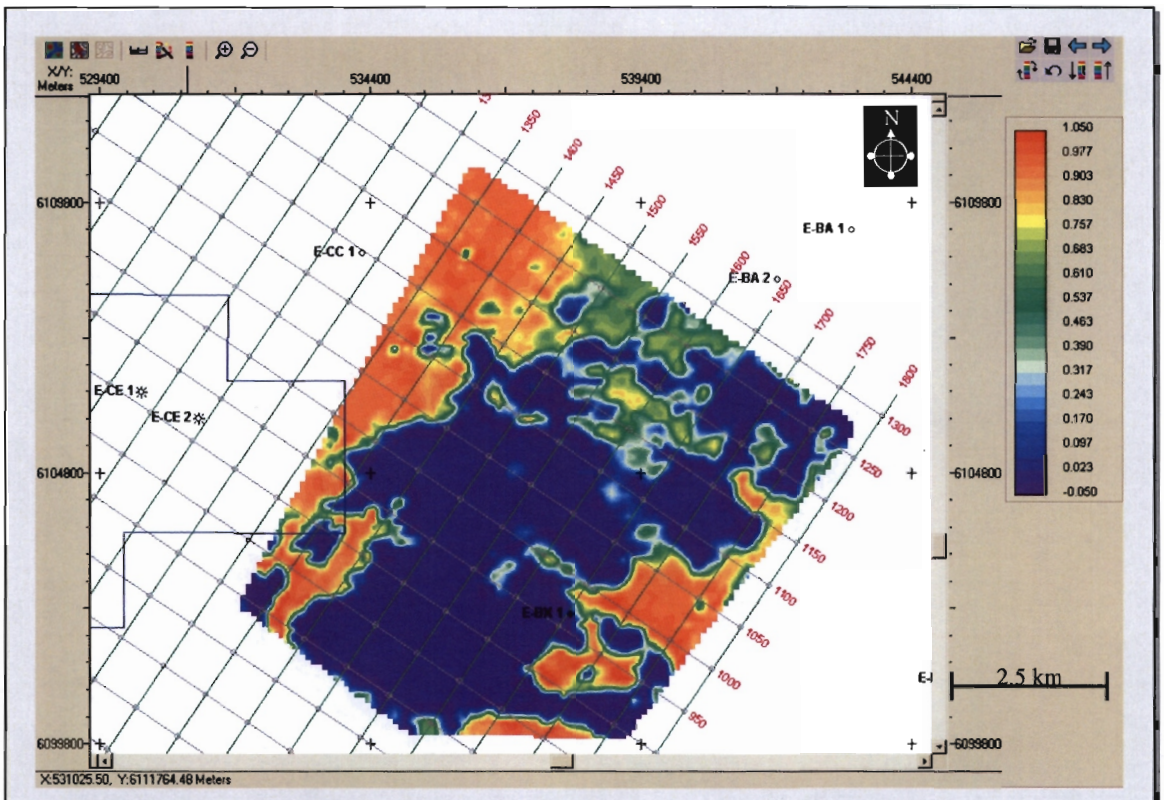

Figure 71. Map of probability of shale, using λρ and μρ from the post-stack inversion.

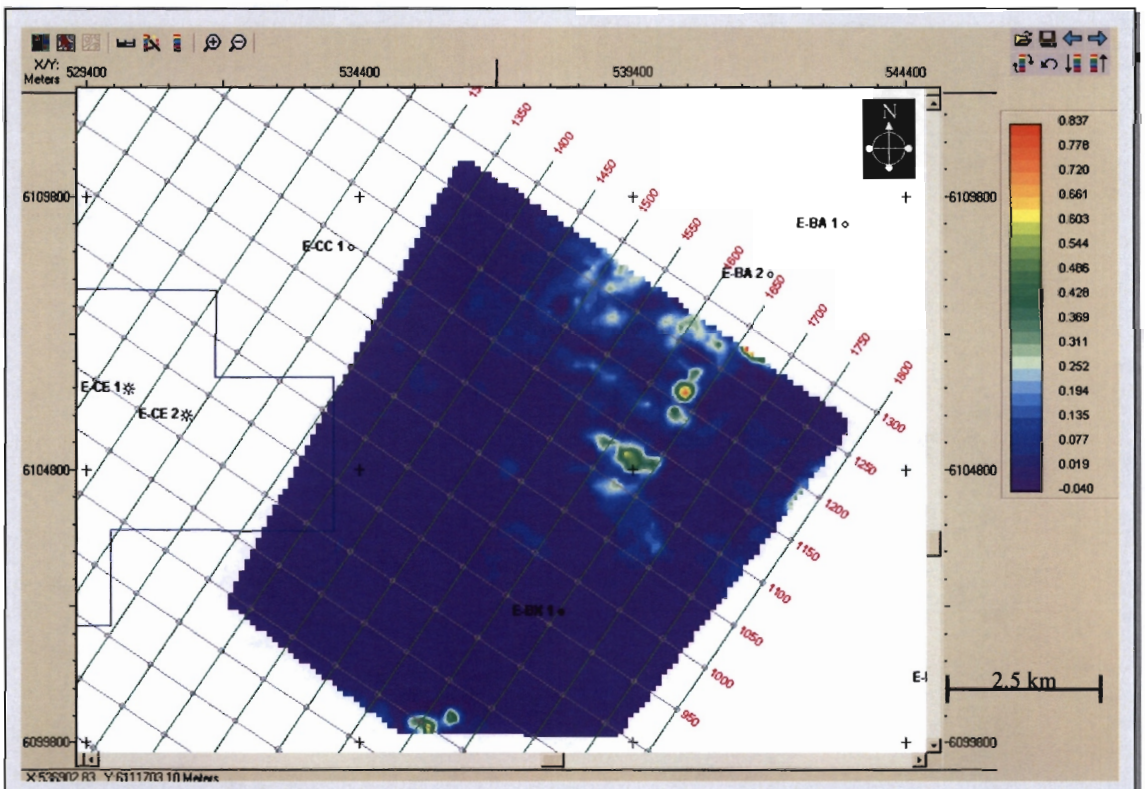

Figure 72. Map of probability of cemented sandstone, using λρ and μρ from the post-stack inversion.

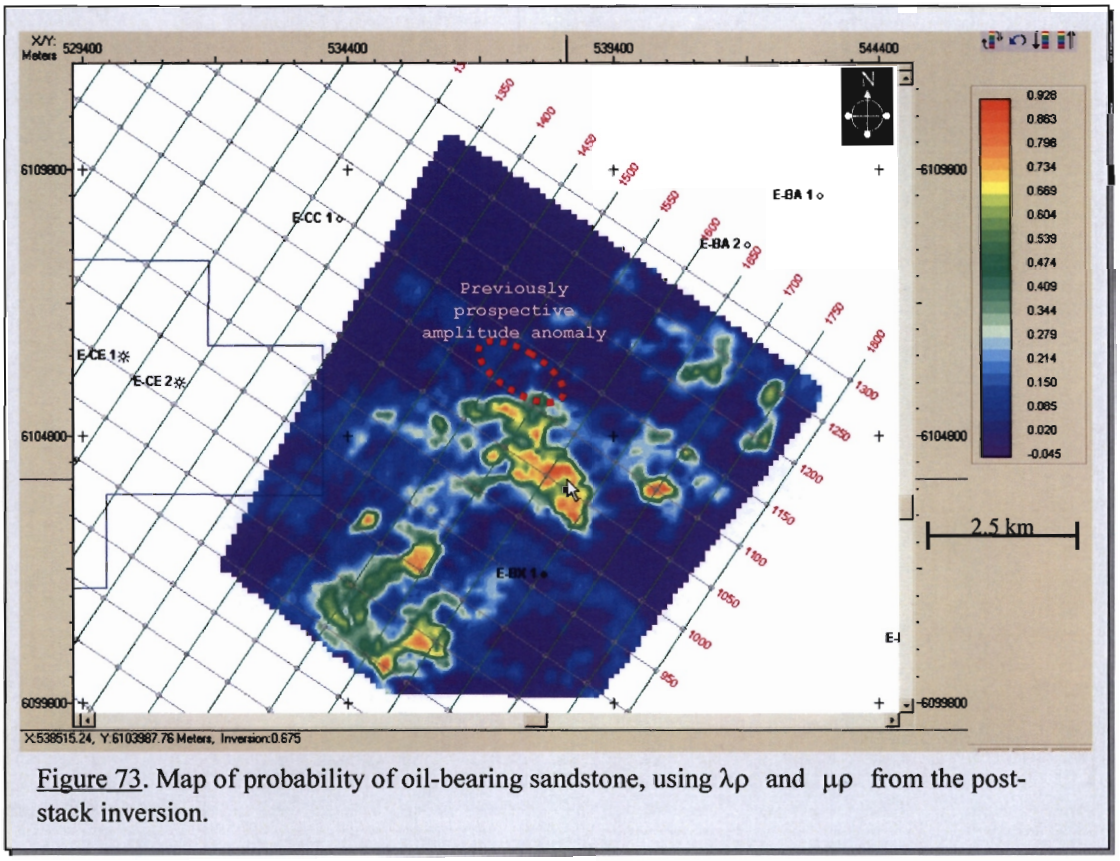

Figure 73. Map of probability of oil-bearing sandstone, using $\lambda\rho$ and $\mu\rho$ from the post-stack inversion.

These four figures contain a large amount of information about the geology and the hydrocarbon system around E-BX1. The water-bearing sandstone and shale probability maps (Figures 70 and 71) indicate a large southwest northeast trending sandstone depositional fairway, which may be bounded to the northwest by the toe of the paleo-slope (Figure 12) and to the southeast by two graben faults (Figures 13 and 17). The amount of shale in this fairway increases towards the northeast, which may indicate more distal depositional environments of the mid- and outer fan (Figure 63).

Figure 72 suggests that the there is very little cemented sandstone at this level around E-BX1. The $\lambda\rho$ and $\mu\rho$ attributes that were used for the classification were extracted over an interval corresponding mainly to the massive upper 13B sandstone. This may be a reason for the lack of cemented sandstone, since it occurs mainly in the facies below and above the massive sandstone. Another reason for the lack of cemented sandstone may be seismic resolution. According to the regional model for sandstone

diagenesis (Fraser and Winters, 1996), pervasive cementation occurred mainly in thin sandstone layers. If these are present in the interval, they will be unnoticed if they are below seismic resolution.

Figure 73 shows the probability of oil-saturated sandstone. Two prospective areas can be identified. The area of high oil-saturated sandstone probability to the west corresponds to the feeder channels of the upper 13B sandstone identified on the coherence map (Figure 17). Since no structural closure of the channel sandstone is anticipated in this area, it is likely that the oil is trapped stratigraphically and that the sandstone terminates against the toe of the paleo-slope. The area of high oil probability to the north of E-BX1 is interesting, since it's existence was not predicted from the seismic interpretation and the geological model. There was no indication of a structural trap in this area from the seismic interpretation. Due to the lack of structural closure in this area of high oil probability, it is most likely that oil is stratigraphically trapped, similar to the trapping style at the nearby Sable Oil Field (Figure 5). It is thus possible that oil is stratigraphically trapped in this, and other areas along the 13B sandstone fairway around E-BX1.

The results of the classification using the pre-stack $\lambda\rho$ and $\mu\rho$ seismic attributes are shown in Figures 74 to 77.

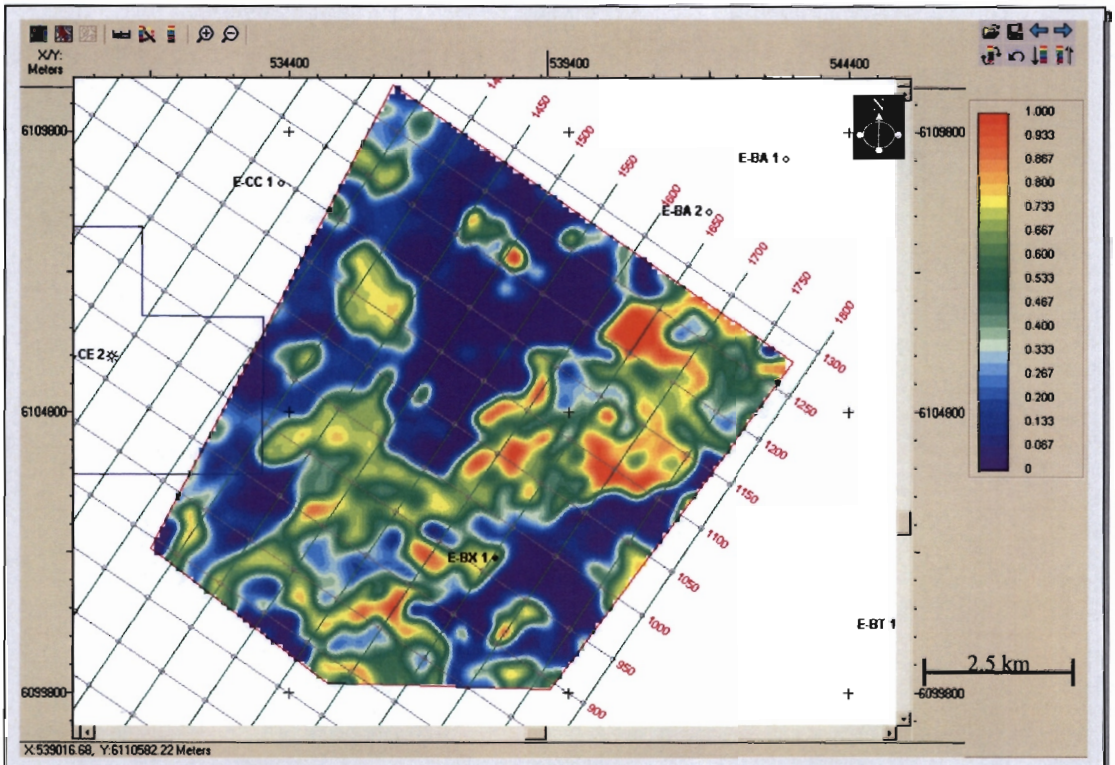

Figure 74. Map of probability of water-bearing sandstone, using $\lambda\rho$ and $\mu\rho$ from the pre-stack inversion.

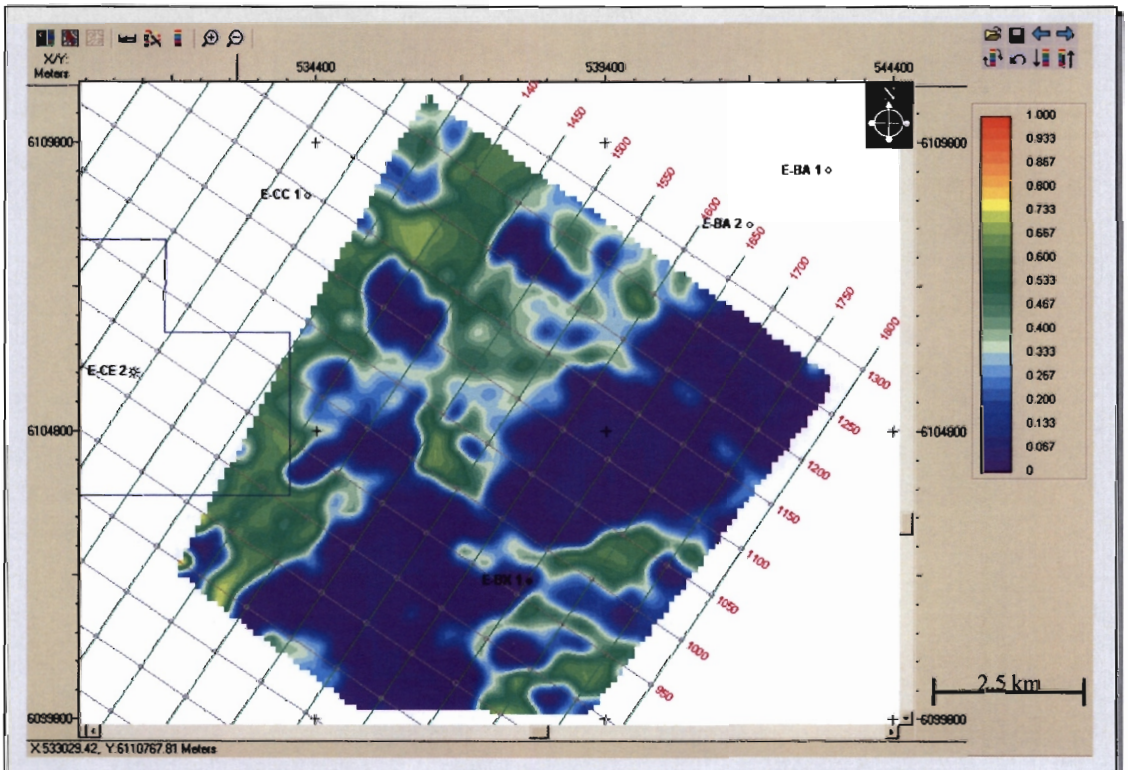

Figure 75. Map of probability of shale, using $\lambda\rho$ and $\mu\rho$ from the pre-stack inversion

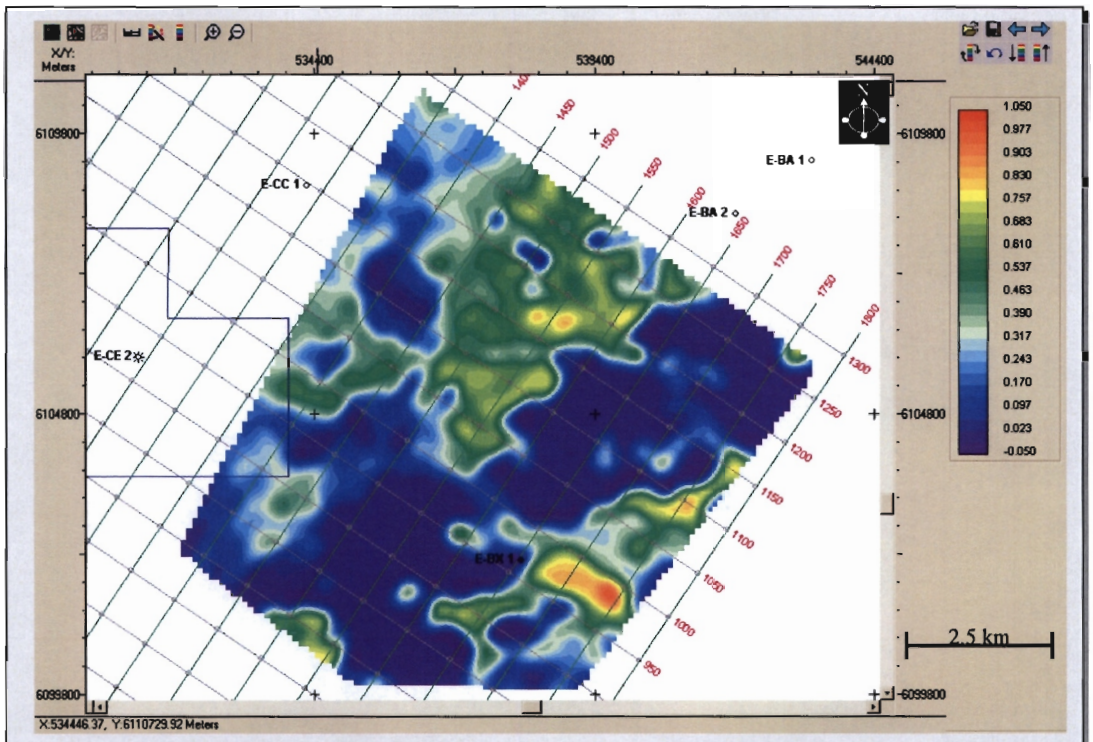

Figure 76. Map of probability of cemented sandstone, using λρ and μρ from the pre-stack inversion

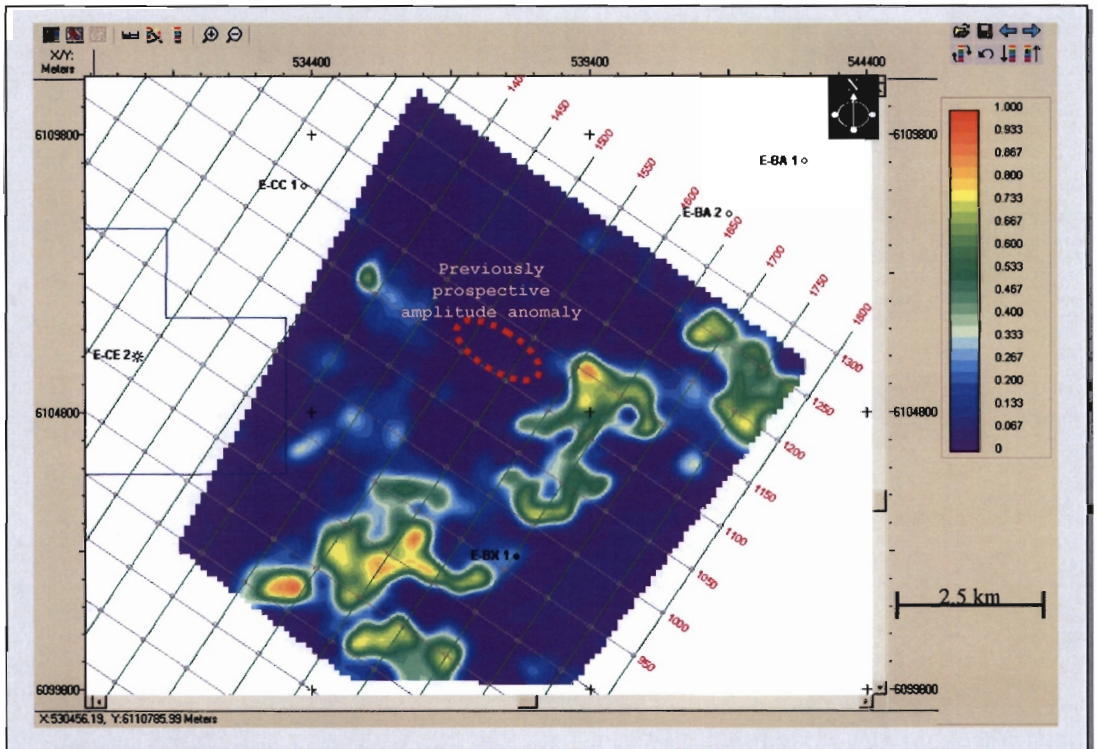

Figure 77. Map of probability of oil-bearing sandstone, using λρ and μρ from the pre-stack inversion.

The results from the pre-stack attribute classification are somewhat similar to those from the post-stack classification, although there are some important differences. The distribution of water-bearing sandstone (Figure 74) also shows a southwest northeast trending fairway, but it is narrower than that identified with the post-stack attribute classification (Figure 70). The probability of shale on the sides of the sandstone fairway is lower than that predicted with the post-stack attribute classification whereas the probability of cemented sandstone is higher (Figures 75 and 76). The shale and cemented-sandstone classes are differentiated by $\mu\rho$ rather than $\lambda\rho$ (Figure 50). The difference between the pre- and post-stack attribute classification for shale and cemented sandstone must thus result from a difference in the extracted $\mu\rho$. A comparison of Figures 36 (post-stack $\mu\rho$) of Figure 45 (pre-stack $\mu\rho$) confirms that the pre-stack inversion predicts a larger distribution of high $\mu\rho$ values, thus increasing the probability of cemented sandstone. Geologically, the increase in cemented sandstone over shale implies that the entire system may be more interbedded and silty than the post-stack results suggest.

Figure 77 shows the probability of oil-bearing sandstone from the pre-stack $\lambda\rho$ and $\mu\rho$ classification. Although the shape of the areas of high oil-probability is somewhat different to those of the post-stack classification, both the western and northern accumulations are present in roughly the same location. Interestingly, the zone of shale that supposedly causes stratigraphic trapping of the oil, to the south of the northern oil anomaly, is more prominent on the pre-stack classification (Figure 75). The structural nose with high seismic amplitude ("northern amplitude anomaly"), which was identified as a potentially prospective area from the seismic interpretation (Figures 18 and 19), is no longer considered prospective, given the low probability of oil-bearing sandstone (Figures 73 and 77).

The work presented in this study shows that combining rock physics, geology and statistics through supervised classification of seismic attributes yields quantitative, problem-tailored solutions for hydrocarbon exploration. The

workflow presented in this study is built on appropriate rock-physics relationships between the seismic attributes available, and the geological parameters being sought. A main feature of the workflow is the extension of the training data. This allows direct incorporation of the prior knowledge of the geological model and the hydrocarbon system. The results of the study are quantitative distribution maps of fluid and lithology categories. They are easy to understand and can be used directly for hydrocarbon exploration, prospect ranking and risking. Furthermore, the method can be used for reservoir management and modeling. The workflow can easily be adjusted to incorporate other data types, for example ocean-bottom seismic data or time-lapse data, by choosing appropriate rock-physics relationships.

The methodology presented in this study can be improved and expanded in a number of ways. For example the effect of seismic noise and seismic processing on $\lambda\rho$ and $\mu\rho$ attributes could be modeled more accurately and included in the classification. This was only done in a very simplistic way for this study, by comparing the $\lambda\rho$ and $\mu\rho$ from the inversions with those from the up-scaled logs at E-BX1 (section 5.1). The difference between the two was attributed to seismic noise, and it may be possible to introduce a similar level of noise in the training data by adding a random component to mimic the inversion results. It should be borne in mind though that the inversions were done from a starting model that honors the well data. Comparing the results at the well may thus not be a fair indication of the seismic noise. A better way to assess the seismic noise is to perform "blind" inversions by systematically leaving out wells from the starting model, and then comparing the inversion results to the "blind" well data. This can only be done if sufficient well data are available.

In this study, $\lambda\rho$ and $\mu\rho$ attributes from pre- and post-stack seismic inversions were used for the calibration. There are many other seismic attributes available, for example $\Delta\lambda\rho$ and $\Delta\mu\rho$ from Smith's equation (Smith, 1999), or even direct extraction of λ and μ using higher-order AVO equations. The use

of these attributes may improve the classification, and thus the workflow presented here. There is also scope for further investigating the difference between the results of the pre- and post-stack inversion attributes.

It has been mentioned before that besides lithology and fluid-fill, other parameters like temperature and pressure affect $\lambda\rho$ and $\mu\rho$. These effects should be included in the training data, since they decrease the ability to discriminate between lithology and fluid-fill groups.

In areas where a large number of closely spaced wells with logging data are available, the seismic inversions should be done by geostatistical inversions for I_p, I_s and I_e. Geostatistical inversions can also provide an estimate of the accuracy away from well control points (Dubrule, 2001). There may be a way to scale the probabilities from the classification to reflect the accuracy from the geostatistical inversion.

Chapter 3 discussed the rock physics relationships that were used in this study. The relationships are for macroscopically isotropic rocks. In areas where strong anisotropy is suspected, the workflow presented in this study has to be adjusted accordingly. The rock physics relationships were mainly used to extend the training data. Only the water-saturated sandstone class was extended in this study, and more accurate results can be obtained if all the classes are lithology-extended.

Most of the shortcomings and improvements suggested in the previous paragraphs will have the effect of lowering the confidence in predicting the spatial variation of lithologies and fluid-fills. The magnitude of the probabilities in Figures 70 to 77 may thus decrease from the values shown.

In conclusion, the results of this study suggest that two 13B stratigraphically trapped oil-accumulations are present around E-BX1. The western accumulation was identified as a prospective area even before the

quantitative classification of the seismic attributes, whereas the northern accumulation was not previously identified as a prospective area. Furthermore, the high seismic amplitude structural nose that lies to the northwest of E-BX1 and was previously identified as a prospective area due to its high seismic amplitude is not considered prospective according to the classification results. The study has therefore changed, or at least challenged the understanding of the geology and hydrocarbon accumulations at the 13B level around E-BX1, by designing a workflow that extracts lithology- and fluid-specific information by combining the log data, regional knowledge and seismic data.

7 References

Aki, K., and Richards, P.G., 1980. Quantitative seismology: Theory and Methods. San Francisco W. H Freeman and Co.

Alberty, M., 1994. The Influence of the Borehole Environment upon Compressional Sonic Logs. *Society of Petrophysicists and Well Log Analysts June 1994 Annual Logging Symposium,* Symposium Transaction 1304.

Avseth, P., Mukerji, and T., Mavko, G., 2005. Quantitative seismic interpretation. Cambridge University Press, United Kingdom.

Backus, G.E., 1962. Long-wave elastic anisotropy produced by horizontal layering. *Journal of Geophys. Res.,* 67, 4427-4440

Batzle, M.L., and Wang, Z., 1992. Seismic properties of pore fluids. *Geophys.*, 57, 1396 – 1408.

Bortfeld, R., 1961. Approximation to the reflection and transmission coefficients of plane longitudinal and transverse waves. *Geophys. Prospecting,* 9, 485-503.

Brown, Jr., L.F., Benson, J.M., Brink, G.J., Doherty, S., Jollands, A., Jungslager, E.H.A., Keenan, J.H.G., Muntingh, A., and van Wyk, N.J.S., 1995. Sequence Stratigraphy in Offshore South African Divergent Basins. *American Association of Petroleum Geologists Studies in Geology,* 41.

Cambois, G., 2001. How to obtain reliable S-impedance from P-wave data. *World Oil*, Vol. 222, No. 9, 37-41.

Castagna, J.P., Batzle, M.L., and Eastwood, R.L., 1985. Relationships between compressional wave and shear-wave velocities in clastic silicate rocks. *Geophys.,* 50, 571-581.

Castagna, J.P., Batzle, M.L., and Kan, T.K., 1993. Rock Physics – The link between rock properties and AVO response, in *Offset-Dependent Reflectivity – Theory and practice of AVO Analysis,* J. P. Castagna and M. Backus, eds. Investigation in Geophysics, No. 8, *Soc. Exploration. Geophys.*, Tulsa, Oklahoma, 135-171.

Connolly, P., 1998. Calibration and inversion of non-zero offset seismic. *Soc. Exploration. Geophys*. 68th Ann. Mtg., Expanded Abstracts.

Dewar, J., 2001. Rock physics for the rest of us, an informal discussion. CSEG Recorder, May Edition, 43-49.

Dubrule, O., 2003. Geostatistics for Seismic Data Integration in Earth Models. Distinguished Instructors Short Course No. 6, Tulsa, Oklahoma.

Fatti J.L., Smith G.C., Vail P.J., Strauss P.J., and Levitt P.R., 1994. Detection of gas in sandstone reservoirs using AVO analysis: a 3D seismic case history using the Geostack technique. *Geophys.,* 59, 1362-1376.

Fraser, N.J., and Winters, S.J., 1996. Regional framework of the 13B Sequence in the west-central Bredasdorp Basin. Soekor E & P internal report number 395.

Gassmann, F., 1951. Über die Elastizität poröser Medien. *Vier. Der Natur. Gesellshaft in Zürich*, 96, 1-23.

Goodway, W., Chen, T., and Downton, J., 1997. Improved AVO fluid detection and lithology discrimination using Lamé petrophysical parameters;

"λρ", "μρ" & "λ/μ fluid stack", from P and S inversions. *Soc. Exploration. Geophys.* 67th Ann. Mtg., Expanded Abstracts, 183-186.

Hashin, Z., and Shtrikman, S., 1963. A variational approach to the elastic behavior of multiphase materials. *J. Mech. Phys. Solids.* 33, 3125-3131.

Hastie, T., Tibshirani, R., and Freidman, J., 2001. The Elements of Statistical Learning: Data Mining, Inference and Prediction. New York: Springer Verlag.

Klimentos, T., 1991. E-BX1 log analysis report. Soekor E&P internal report.

Kuster, G.T., and Toksöz, M.N., 1974. Velocity and attenuation of seismic waves in two phase media. *Geophys.*, 39, 587-618.

Mavko, G., Mukerji, T., and Dvorkin, J., 1998. The Rock Physics Handbook. Cambridge University Press, United Kingdom.

Mukerji, T., Mavko, G., Mujica, D., and Berge, P.A., 1995. Scale dependent seismic velocity in heterogeneous media. *Geophys.*, 60, 1222–1233.

Norris, A.N., 1985. A differential scheme for the effective moduli of composites. *Mechanics of Materials,* 4, 1-16.

O'Connor, J., and Robertson, F., 2004. The MacTutor History of Mathematics archive. University of St Andrews, Scotland.

Reading, H.G., Richards, M., 1994. Turbidite systems in deep water basin margins classified by grain size and feeder system. *Bulletin of the American Association of Petroleum Geologists*, 78, 792–822.

Reinhardt, F., and Soeder, H., 1991. Atlas zur Mathematik. Deutscher Taschenbuch Verlag GmbH & Co. KG, München.

Reuss, A., 1929. Berechnungen der Fliessgrenzen von Mischkristallen. Z. Angew. Math. Mech.,9, 49-587.

Scott Pickford Core Laboratories Company, 2000. Rock Properties and Seismic. Scott Pickford Poster Publications.

Smith, G.C., 1999. The Relationship between Lamé's Constants, λ and μ, and the Fluid Factor in AVO Analysis of Seismic Data. *6th Biennial SAGA Conference and Exhibition*, Extended Abstracts.

Smith, G.C., and Gidlow, P.M., 1987. Weighted stacking for rock property estimation and detection of gas. Geophysical Prospecting, 35, 993-1014.

Snyman, C.P., 1996. Geologie vir Suid-Afrika. Departement Geologie, Universitiet van Pretoria, Pretoria.

Voigt, W., 1910, Lehrbuch der Kristallphysik. Lebzig: Teubner.

Wood, A.W., 1955. A Textbook of Sound. The MacMillan Co., New York.

Wyllie, M.R.J., Gardener, G.H.F., and Gregory, A.R., 1963. Studies of elastic wave attenuation in porous media. *Geophys.*, 27, 569 – 589.

Xu, S., and White, R., 1995, A new velocity model for clay-sand mixtures. Geophysical Prospecting, 43, 91-118.

Zimmerman, R.W., 1991. Compressibility of Sandstones, Elsevier, New York.

Zoeppritz, K., 1919. Erdbebenwellen VIIIB, On the reflection and propagation of seismic waves. Göttinger Nachrichten, I, 66-84.

Appendix A

Reflectivity and AVO

In section 4.6 Vp-Vs relationships and full-offset synthetics were discussed. These topics are related to acoustic wave propagation at the interface between two acoustic layers. Of special interest to AVO is the acoustic behavior when the angle of incidence upon such an interface is non-normal. The following sketch illustrates how a incident P-wave is transformed into transmitted P- and S-waves, as well as reflected P- and S-waves.

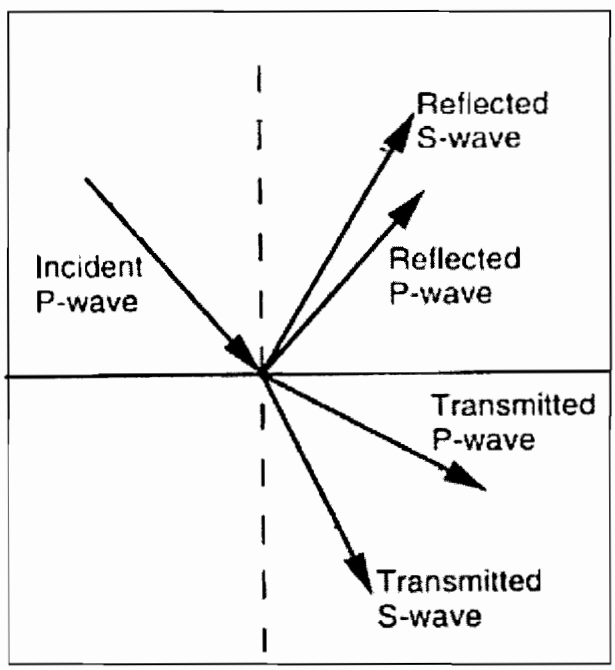

Figure A1. Illustration of how a P-wave is transformed into P-and S-waves at an acoustic interface during non-normal incidence

The reflection and transmission coefficients depend on the change in acoustic properties across the interface as well as the angle at which the incident P-wave strikes the interface. The complete solution for both reflected and transmitted P- and S-waves is given by the Zoeppritz equations (Zoeppritz, 1919), although various approximations have been derived since then. Bortfeld (1961) and later Aki and Richards (1980) derived linearized equations for the reflection coefficients by assuming small contrasts in

acoustic properties at the interface. Aki and Richard's 1980 equation for the P-wave reflection coefficient is given below (Aki and Richards, 1980).

$$R_{PP}(\theta) \approx \frac{1}{2}\left(\frac{\Delta Vp}{Vp} + \frac{\Delta \rho}{\rho}\right) + \left[\frac{1}{2}\frac{\Delta Vp}{Vp} - 2\frac{Vs^2}{Vp^2}\left(\frac{\Delta \rho}{\rho} + 2\frac{\Delta Vs}{Vs}\right)\right]\sin^2\theta + \frac{1}{2}\frac{\Delta Vp}{Vp}\left[\tan^2\theta - \sin^2\theta\right] \quad \text{(A1)}$$

Vp	P-wave velocity
Vs	S-wave velocity
ρ	density
θ	angle of incidence

Fatti et al. (1994) suggested a formulation of the above equation using impedance contrasts. This formulation is generally more accurate when the third term is ignored. This equation is given below

$$R_{PP}(\theta) \approx \frac{\Delta I}{2I}(1 + \tan^2\theta) - 4(Vs_{av}/Vp_{av})^2(\Delta J/J)\sin^2\theta \quad \text{(A2)}$$

I	P-wave impedance
J	S-wave impedance
Vp_{av}	Average P-wave velocity across impedance boundary
Vs_{av}	Average S-wave velocity across impedance boundary